Energy Transport during Growth and Collapse of a Cavitation Bubble

by

Minki Kim

A dissertation submitted in partial fulfillment
of the requirements for the degree of
Doctor of Philosophy
(Mechanical Engineering and Scientific Computing)
in The University of Michigan
2022

Doctoral Committee:

Associate Professor Eric Johnsen, Chair
Professor Steven L. Ceccio
Associate Professor Karthik Duraisamy
Assistant Professor Jonathan B. Estrada
Professor J. Brian Fowlkes

Minki Kim
minkikim@umich.edu
ORCID iD: 0000-0002-8613-0206

DEDICATION

To my beloved family

ACKNOWLEDGMENTS

I have had the great honor of working with my advisor, Professor Eric Johnsen who are not only exceptional researcher, but also kind and supportive mentor. Thank you to my advisor who has patiently worked with me to form abstract scientific questions into analyses, epitomizes research excellence, and always approaches our work with generous enthusiasm, and fostered a welcoming network of collaborators.

I am very grateful to my committee members, Professor Steven Ceccio, Karthik Duraisamy, Jon Estrada, and Brian Fowlkes for their thoughtful insight and positivity as well as my BRC collaborators – Professor Tim Colonius, Christian Franck, David Henann, and Zhen Xu, and Dr. Jon Sukovich, Jin Yang, and Selda Buyukozturk – for their contributions that greatly benefited this research.

I would like to thank my dear friends in Scientific Computing and Flow Physics Laboratory and my Korean friends. They have provided an abundance of support and adventures that made these years so meaningful and memorable. I am grateful to our cavitation subgroup members – Prof. Mauro Rodriguez, and Dr. Shahab Beig, Kazuya Murakami, Lauren Mancia, Erin Burrell, Baudouin Fonkwa, Yuenong Ling, and William White – for their great suggestions, insights, and thoughtful questions. I also thank other past and current lab members – Dr. Ziyang Huang, Philip Johnson, Loc Khieu, Sam Pellone, Siddhesh Shinde, Suyash Tandon, Eunhye An, Griffin Cearley, Sonya Dick, Codie Fiedler-Kawaguchi, Nick Luccido, Kevin Ma, Mizuho

Takayama, Michael Wadas – for their support in our lab. Special thanks to Kazuya and Eunhye for the fruitful discussions and enjoyable time.

I would like to thank all of my family members, my wife and my baby girl who have been so supportive every step of the way. The love and support is so meaningful in my life and I can never thank you enough.

This work was supported in part by ONR grants N00014-12-1-0751 (under Dr. Ki-Han Kim) and N00014-17-1-2058 (under Dr. Timothy Bentley). This work used the Extreme Science and Engineering Discovery Environment (XSEDE), which is supported by National Science Foundation grant number ACI-1548562. I would like to recognize full financial support from Kwanjeong Educational Foundation throughout my Ph.D.

TABLE OF CONTENTS

LIST OF FIGURES

Figure

LIST OF TABLES

Table

LIST OF APPENDICES

Appendix

ABSTRACT

Cavitation bubbles are widely observed in a variety of applications, from naval engineering to biomedical science. One of the major outcomes of cavitation is structural damage produced by the repeated collapse of bubbles, which is undesirable in naval applications. Due to limited optical access and the destructive nature of bubbles, damage induced by cavitation bubbles is not well understood.

As cavitation bubbles undergo a rapid compression that concentrates energy into a small volume, some of this energy is released through a shock wave that has the potential to induce damage to the nearby rigid surface. To develop strategies to mitigate the damage induced by bubbles, it is essential to understand the relationship between the shock properties and the initial conditions (e.g., bubble size, and the liquid and bubble pressures). For this purpose, we consider the canonical problem of the collapse of a single bubble in a liquid, both in a free field and near a solid surface. In particular, we investigate energy transport in the system comprising the bubble and surrounding liquid, with a focus on the role of compressibility.

We first examine the role of liquid compressibility in energy concentration and release during the inertial collapse of a spherical gas bubble. We develop an improved approach for calculating energy transport during bubble collapse, which enables more accurate predictions of energy transport. We also provide closed-form expressions for the energy and size of the bubble at collapse in terms of the parameters governing the problem, which can account for the effects of liquid compressibility. We further provide an analytical model relating the shock pressure to the parameters governing the problem.

Our framework and scaling relations could be used in conjunction with single-phase simulations as a means to estimate the cavitation activity and to help devise strategies to mitigate cavitation.

We identify the dependence of the bubble response and key shock properties on waveform parameters in ultrasound-driven bubble growth and collapse. We develop a framework to understand how energy is transferred from the wave to the system, and to determine the effect of viscosity and surface tension on energy transport in the system. This framework enables us to identify relationships describing bubble expansion during growth and energy concentration at collapse based on the waveform properties.

When the bubble is adjacent to a neighboring boundary, the boundary breaks the symmetry, such that the bubble collapses in a non-spherical fashion, thereby producing a re-entrant jet that penetrates the bubble, impacts the distal side, and thus generates a water-hammer shock. We investigate the role of compressibility in the dynamics of a gas bubble collapsing near a rigid surface. By comparing direct simulations with potential flow simulations, we assess the effects of compressibility on the dynamics of the bubble and the re-entrant jet. We observe a delay between the two approaches, attributed to differences in the pressure fields at an early stage due to compressibility effects. Nevertheless, the bubble morphologies are similar for most of the collapse, with discrepancies visible only in the final stages of collapse. We discuss the effects of compressibility on the dynamics of the bubble and the jet at jet impact. This knowledge will improve the understanding of the importance of waves generated during collapse and will inform efforts to develop a better model to predict shock properties.

CHAPTER 1

Introduction

This chapter provides an introduction to (i) cavitation, (ii) the damage induced by cavitation bubbles, (iii) knowledge gaps in damaging mechanisms, and (iv) an overview of the thesis. First, this chapter begins with a general description of cavitation and how it damages solids. Then, the chapter provides a general overview of cavitation bubble dynamics, before engaging in a more detailed discussion of dynamics of a single bubble, with a focus on the energy transfer between liquid and bubble. Finally, the chapter concludes with an overview of the thesis, research objectives, and highlights key contributions to the field of cavitation erosion and ultrasound-induced cavitation.

1.1 Cavitation in science and engineering

Cavitation is the process whereby vapor bubbles are formed due to the reduction of local pressure in a liquid. Conventionally, in contrast to boiling, cavitation occurs when the local pressure drops below the saturation vapor pressure, such that the liquid undergoes a phase transition to vapor at a given temperature (Brennen, 1995).

Once cavitation bubbles are generated, they interact dynamically with the surrounding flow fields, such that the behavior of these bubbles depends on the local pressure variations. For a small increase in pressure, a bubble collapses and rebounds at a small amplitude. Conversely, for a large increase in pressure, a bubble undergoes a violent collapse, called inertial collapse. During inertial collapse, the liquid inertia dominates the motion of the bubble wall and accelerates the collapsing motion, such that the bubble volume is reduced by several orders of magnitude relative to the maximum bubble volume. Through this process, the energy of a system is concentrated into the bubbles during the collapse. As a result, pressure and temperature build up inside the bubble at collapse. As the bubbles rebound, they emit high-amplitude pressure waves (or shock waves) propagating outward. These strong waves are one of the major consequences of cavitation, which damages the neighboring rigid surfaces (Tomita & Shima, 1986; Philipp & Lauterborn, 1998; Lindau & Lauterborn, 2003; Johnsen & Colonius, 2009).

The destructive nature of cavitation bubbles plays a critical role in determining the sustainability of a system in a large variety of applications, including naval hydrodynamics (Knapp *et al.*, 1970; Plesset & Prosperetti, 1977), turbomachinery (Arndt, 1981), and the Spallation Neutron Source (SNS) (Riemer *et al.*, 2014; Winder *et al.*, 2020), as illustrated in figure 1.1. In naval hydrodynamics, cavitation bubbles can cause severe structural damage to the facilities, leading to financial losses. Low-pressure regions are created due to rapid changes in the velocity field near the solid surfaces and lead to the generation of cavitation bubbles. The repeated collapse of cavitation bubbles can erode the surface of naval structures (e.g., rudders, hydropropellers, etc.), as illustrated in figure 1.1(a), and can significantly reduce the performance of these structures. In another example, cavitation erosion also reduces the sustainability of the SNS at Oak Ridge National Laboratory (Riemer *et al.*, 2014; Winder *et al.*, 2020). The left sides of figure 1.1(b) shows the schematic of the SNS target. In the SNS, an accelerator-based system directs short proton pulses to a steel target filled with liquid mercury. However, these proton pulses create large, transient increases in the local pressure in the mercury, leading to the generation of cavitation bubbles. As the bubbles collapse inertially, the surface of the target container is damaged, as shown in the right side of figure 1.1(b), and must be replaced.

While cavitation erosion is undesirable in hydraulic applications, cavitation bubbles are utilized to provide better strategies for therapeutic and diagnostic ultrasound. Figure 1.1(c) schematically depicts the histotripsy procedure, which employs focused ultrasound and cavitation bubbles to homogenize soft tissue into acellular debris for treatment of prostate diseases, blood clots (thrombolysis), kidney stones, and solid tumors (Maxwell *et al.*, 2009; Khokhlova *et al.*, 2015). When the

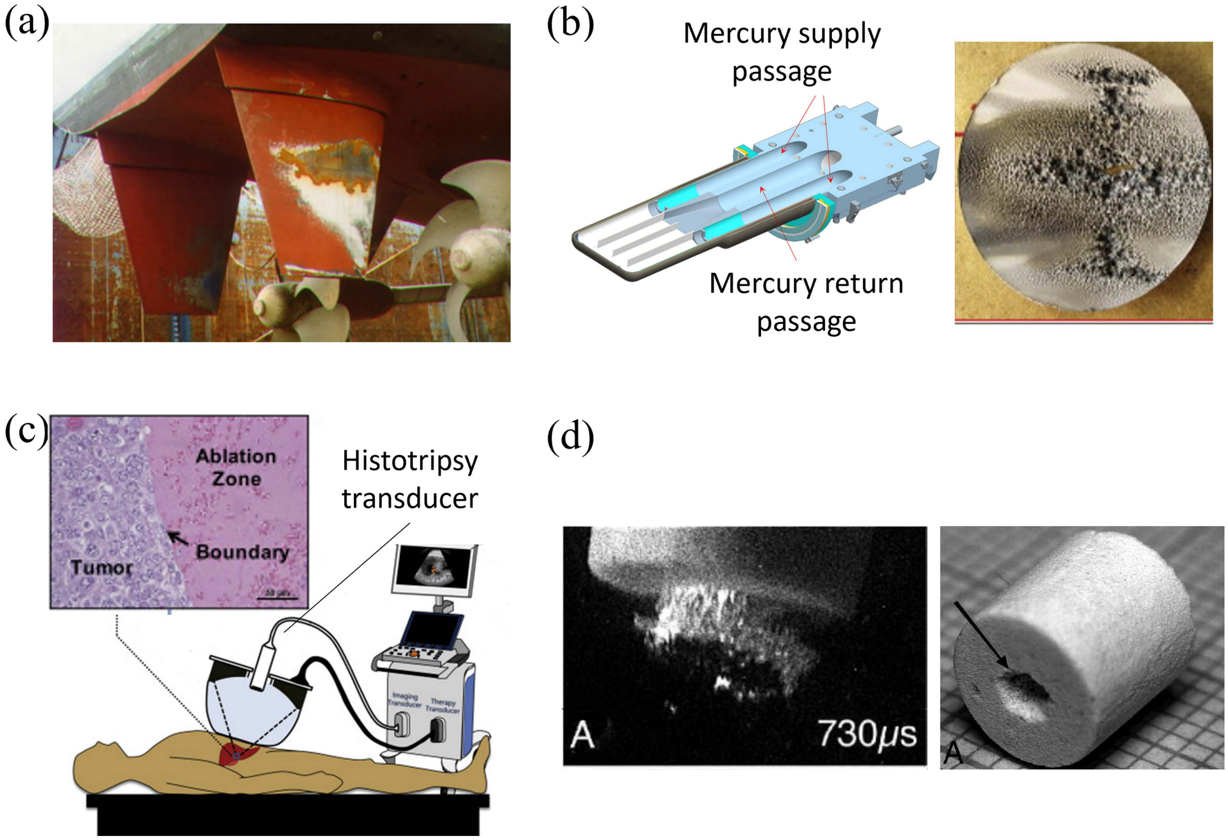

Figure 1.1: Cavitation phenomena in various applications; (a) erosion along rudders (Chahine *et al.*, 2014); (b) schematic of the SNS target with mercury supply and return passages (Winder *et al.*, 2020) and eroded target container (Riemer *et al.*, 2014); (c) histotripsy procedure and disintegration of tissue after treatment (Bader *et al.*, 2019); (d) bubble cluster collapse near an artificial kidney stone and damage on stone (Pishchalnikov *et al.*, 2003).

focused ultrasound pulses interact with a gas nucleus, the negative pressure regions in the pulses break the mechanical equilibrium sustained at the nucleus–liquid interface, which leads to the growth and collapse of bubbles. For the purpose of the histotripsy, pulses with a sufficiently large amplitude are used to cause the bubble to undergo inertial cavitation (i.e., explosive growth and inertial collapse) (Khokhlova *et al.*, 2015; Bader *et al.*, 2019). During this process, the surrounding medium is significantly deformed, and shock waves are produced at collapse, thus damaging the nearby tissue. In extracorporeal shock wave lithotripsy, cavitation also plays a role in fractionating kidney stones (Pishchalnikov *et al.*, 2003). Focused shock waves fractionate kidney stones by inducing large tensile stresses within the stones as the shock waves are reflected (Zhong, 2013). In addition, cavitation bubbles are generated near the kidney stones due to rarefactional pressures, and as the bubbles collapse inertially, the nearby kidney stones can also be damaged (Zhong *et al.*, 1993; Brujan, 2004; Weinberg & Ortiz, 2009), as shown in figure 1.1(d).

With the numerous aforementioned applications, it is essential to have a better understanding of the damaging mechanisms of cavitation bubbles to both mitigate or utilize cavitation bubbles. The following subsection identifies the knowledge gaps in cavitation erosion.

1.1.1 Cavitation erosion

Cavitation erosion is a challenging problem in the field of multiphase flows and fluid–structure interactions. The wide range of length scales, as well as multiple physical phenomena, involved in cavitation erosion poses a challenge to investigating this phenomenon. For instance, cavitating flows include micro-size vapor cavities and millimeter-scale macroscopic flows that interact with each other (Ghahramani *et al.*, 2021), such that the ability to experimentally measure all flow structures simultaneously is limited. In addition, for the numerical analysis of cavitation erosion, a framework for simultaneously considering changes in solids (e.g., structural deformation) and fluid flows (e.g., transient pressure fields) is needed, which requires excessive computing capabilities. This section offers a detailed overview of the erosion process.

The process of cavitation erosion to hard and metallic surfaces can be explained by a sequence of four steps (Kim *et al.*, 2014). The first step is the production of vapor bubbles; local pressure reduction in the flows near the surfaces leads to generation of large-scale vapor structures, which break up into small vapor bubbles. Second, when the bubbles are subjected to high pressure regions, large liquid pressure drives the collapse of the bubble, which is often inertial. The outcomes of such collapse (e.g., shocks) give rise to a localized, high intensity on material surface over a short duration, on the order of a microsecond. Thus, the mechanical energy concentrated on a small area of surface produces high stresses that can exceed the resistance of the material (e.g., yield stress or ultimate strength), such that local damage is induced (Franc & Michel, 2006; Kim *et al.*, 2014). In the third step, the repeated collapse of bubbles causes pit formation on the surface (Philipp & Lauterborn, 1998; Dular *et al.*, 2013). Finally, a large number of superimposed pits

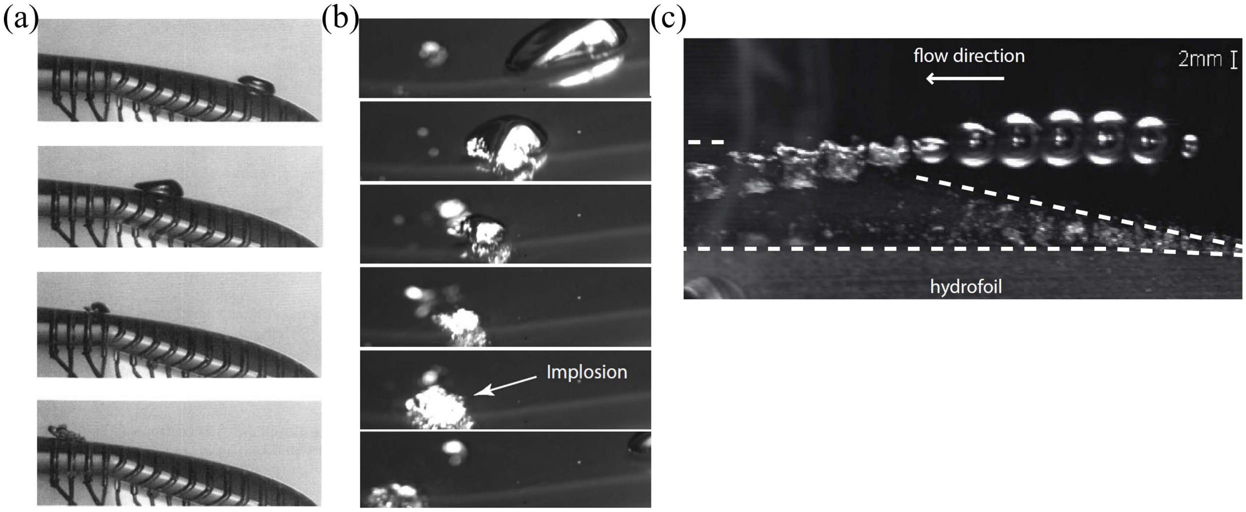

Figure 1.2: Cavitation bubble traveling on the curved surface; series of photograph of (a) a hydrodynamically generated bubble traveling on the Schiebe headform (Ceccio & Brennen, 1991) and (b) a bubble traveling on the wall of an elliptical profile mounted in the tunnel cavitation (Guennoun, 2006), and (c) superposition of the images of a laser-induced bubble generated above hydrofoil (Tinguely, 2013).

leads to the mass loss of the material (Chahine *et al.*, 2014).

While most of these steps in the erosion process have been well characterized, the impact loads due to cavitation bubble collapse in the second step still remains unclear. Several studies have revealed how the problem parameters (i.e., bubble size, driving pressure, and distance between the bubble centroid and a surface) are dependent on the impact pressure on a nearby rigid surface (Naudé & Ellis, 1961; Tomita & Shima, 1986; Vogel *et al.*, 1989; Supponen *et al.*, 2016, 2017). However, these relations are only applicable to limited cases, and a more comprehensive description of the relationship is needed to predict damage potential in bubble collapse.

1.2 Cavitation bubble dynamics

In industrial applications, microscopic bubbles interact with the underlying macroscopic flows, which significantly affect the surrounding pressure fields near the bubbles (Bark & Bensow, 2014). Figure 1.2 shows the growth and collapse of a bubble traveling on the surface of structures (i.e., a Schiebe headform, elliptic profile in a tunnel, and hydrofoil) (Ceccio & Brennen, 1991; Guennoun, 2006; Tinguely, 2013). Although the bubble is generated by different mechanisms (i.e., hydrodynamics and lasers), it shows similar shapes and behaviors due to the strong effects of the macroscopic flows on bubble dynamics (Tinguely, 2013). Specifically, the bubble shows a particular shape in the final stage of collapse (Ceccio & Brennen, 1991; Guennoun, 2006; Tinguely, 2013); thus, bubble dynamics during collapse depend on the macroscopic properties of the flows.

The interactions between microbubbles and macroscopic phenomena also play a key role in therapeutic and diagnostic ultrasound. Figure 1.3(a) shows the growth of nanobubbles induced by ultrasound in histotripsy treatment, which has a wavelength much greater than the size of the bubbles. The ultrasound significantly changes the surrounding pressure fields near the bubbles, such that it leads to the growth and collapse of the bubble. The bubble oscillations contribute to the fragmentation of kidney stones in lithotripsy therapy, as illustrated in figure 1.3(b). Thus, the consequences of bubble oscillations depend on the macroscopic properties of the waveform.

For bubbles that are smaller than spatial variations in the surrounding instantaneous pressure fields, the individual bubble dynamics are linked to the macroscopic flows or external waves by pressure difference $p_\infty(t) - p_b(t)$, where $p_\infty(t)$ is the pressure fields in large-scale flows and p_b is the pressure inside the microbubble, through the well-known Rayleigh–Plesset equation (Rayleigh, 1917; Plesset, 1949). This equation assumes a perfectly spherical bubble in inviscid, incompressible flows, which is given by

$$R\ddot{R} + \frac{3}{2}\dot{R}^2 = \frac{p_b(t) - p_\infty(t)}{\rho_l} - \frac{4\mu_l}{\rho_l}\frac{\dot{R}}{R} - \frac{2S}{\rho_l R}, \tag{1.1}$$

where R is the bubble radius, ρ_l is the liquid density, μ_l is the dynamic viscosity of the liquid and S is the surface tension. Other advanced models of bubble dynamics are typically based on this equation (Keller & Kolodner, 1956; Flynn, 1975b; Nigmatulin *et al.*, 1981; Prosperetti, 1991); for these models, the pressure difference is still a bridge relating the microscopic bubble dynamics to macroscopic flows or external waves. In naval hydrodynamics, these bubbles are often observed in vortical flows, including in the flows near a rotating machine (e.g., a hydropropeller) (Kim *et al.*,

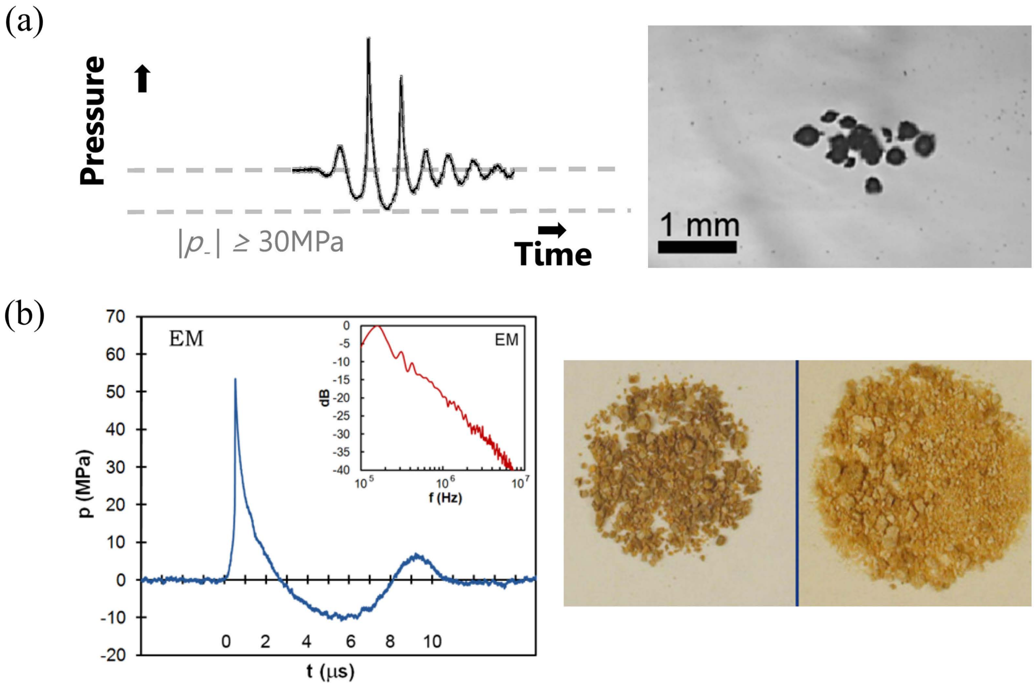

Figure 1.3: Ultrasound-induced cavitation; (a) (Left) focal pressure waveforms with a 10-cycle pulse used in histotripsy and (right) growth of cavitation bubbles (Bader *et al.*, 2019). (b) (Left) Pressure wavesforms produced by shock wave lithotripers and (right) fragmented kidney stones in water (Zhong, 2013).

2014). Thus, it is critical to understand the dynamics of individual bubbles and their relation to the macroscopic flows or waves to reduce or control cavitation-induced damage. This area is still not well understood. Specifically, understanding of the dependence of impact loads and bioeffects on the problem parameters is key to develop a predictive model for cavitation-induced damage in naval hydrodynamics and therapeutic ultrasound. The following subsections describe a current understanding of single bubble dynamics and discuss the energy transport in a system needed for describing the relationship between the individual bubbles and macroscopic phenomena.

1.2.1 Spherical bubble dynamics

Rayleigh collapse occurs when a spherical bubble in an infinite sea of liquid collapses due to an instantaneous increase in the surrounding pressure fields (Brennen, 1995). The Rayleigh collapse problem also corresponds to the limiting case of bubble collapse induced by a shock wave propagating at an infinite speed. This problem has been investigated, in the context of cavitation erosion (Brennen, 1995). The dynamics of a spherical bubble are described by the Rayleigh–Plesset equation (equation 1.1). Other complex physics (e.g., liquid compressibility, thermal conduction, viscosity, surface tension) have been introduced to this equation to better describe bubble collapse in practical applications (Gilmore, 1952; Keller & Kolodner, 1956; Keller & Miksis, 1980; Prosperetti, 1991).

In the Rayleigh collapse problem, when the far-field liquid pressure is sufficiently large, the bubble collapses inertially. During inertial collapse, the initial energy in a system is concentrated in the bubble. However, as the bubble perturbs the liquid during collapse, acoustic waves propagate radially outward from the bubble wall, such that the bubble loses its energy through acoustic radiation. As a result, the concentration of energy in the bubble is limited, such that the strength of a shock produced at collapse is reduced (Obreschkow *et al.*, 2011; Tinguely, 2013). To predict the damage induced by inertial collapse, a model for shock strength based on initial conditions (e.g., bubble sizes, driving pressures), is needed. However, a more precise understanding of the effects of liquid compressibility is required to achieve this goal.

When subjected to high-amplitude ultrasound waves, bubble dynamics are significantly affected by temporal variations in the surrounding pressure fields. As waves interact with a pre-existing bubble, they introduce energy to the liquid–bubble system, which drives the explosive growth and inertial collapse of the bubble, followed by energy release via shocks produced at collapse. The input energy is concentrated into the bubble during collapse, while some of the energy is transferred to the surrounding medium via shock waves. The outcomes of such collapse (e.g., inertial collapse, shock emission) may lead to damage to the surrounding medium, which can produce undesirable bioeffects (Patterson *et al.*, 2012; Versluis *et al.*, 2020) and mechanically ablate tissue in biomedical applications (Xu *et al.*, 2004; Parsons *et al.*, 2006; Khokhlova *et al.*, 2015). Further investigation of the dependence of the bubble response on external waves is needed to better utilize cavitation bubbles and control bioeffects.

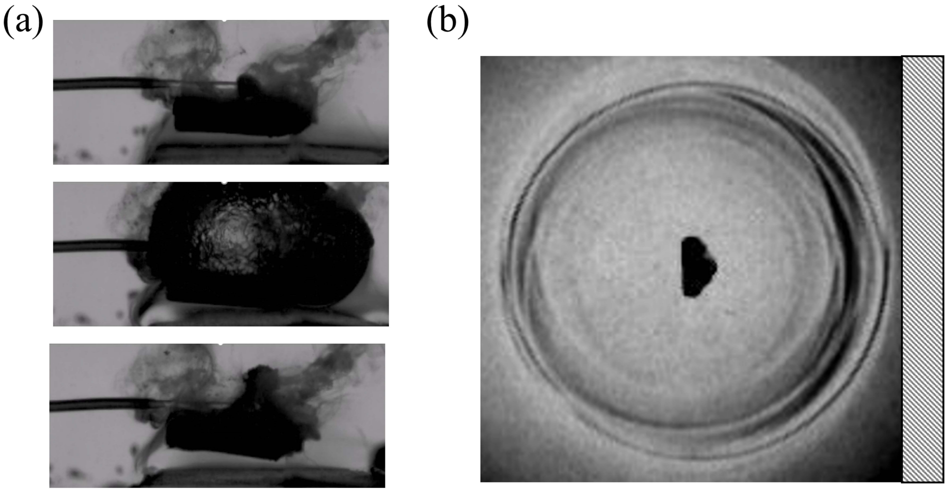

Figure 1.4: Dynamics of a non-spherical bubble near a rigid boundary; (a) Growth and collapse of a laser-induced cavitation bubble near a boundary and (b) non-spherical collapse of a bubble, leading to the formation of the re-entrant jet and emission of the shock (Supponen *et al.*, 2017).

1.2.2 Non-spherical bubble dynamics

When the bubble is adjacent to a neighboring boundary, the presence of the boundary breaks the symmetry, such that the bubble collapses in a non-spherical fashion (Naudé & Ellis, 1961; Plesset & Chapman, 1971; Blake *et al.*, 1986; Vogel *et al.*, 1989; Philipp & Lauterborn, 1998; Brujan *et al.*, 2002; Supponen *et al.*, 2016). Figure 1.4 shows the dynamics of a non-spherical bubble collapsing near a rigid boundary. At the very beginning of the collapse, the initial pressure difference leads to the generation of rarefaction waves, propagating radially outward, hitting a nearby object, and reflecting off objects with negligible attenuation due to a large impedance mismatch between the boundary and liquid. The reflected waves interact with the collapsing bubble, leading to significant changes in nearby pressure fields. However, with the assumption of an incompressible liquid flow, the bubble instantaneously communicates with the nearby boundary; there are significant differences in the surrounding pressure fields between the compressible and incompressible cases. Thus, the overall bubble and jet dynamics are expected to depend significantly on liquid compressibility.

In addition, the hydrodynamic interactions between the bubble and the boundary drive the formation of a high-speed liquid re-entrant jet toward the boundary, penetrating the bubble. When the re-entrant jet impacts the opposite side of the bubble wall, a water-hammer shock wave is produced (see figure 1.4(b)), propagating radially outward and subsequently impinging upon the neighboring wall, thus creating an impact load. In non-spherical collapse, as with spherical collapse, the initial energy is concentrated into the bubble at collapse. However, the re-entrant jet hinders the converging bubble–wall motion such that non-spherical collapse is less effective in energy concentration than spherical collapse (Pearson *et al.*, 2004; Wang, 2016). In addition, when the bubble collapses farther from the boundary, it remains spherical for a longer time during its collapse until the waves reflect back onto the bubble. Furthermore, during non-spherical collapse, energy concentration also becomes less efficient due to liquid compressibility, similar to spherical collapse. In particular, due to energy losses through acoustic radiation, the formation of the re-entrant jet and the subsequent emission of shocks are significantly affected by liquid compressibility, especially at high driving pressures. Thus, a better understanding of the effect of compressibility on non-spherical bubble dynamics is needed to build a predictive model for damage potential in bubble collapse near a rigid boundary.

1.3 Thesis overview

This thesis aims to use theoretical modeling and high-fidelity simulations to (i) better understand the growth and collapse of gas bubbles in an infinite medium and near a rigid surface, and (ii) predict the properties of shocks produced at collapse. This knowledge is instrumental in estimating the damage potential of bubble collapse as well as in predicting the dynamics of a bubble in an acoustic field. The key contributions to the field of cavitation bubble dynamics are summarized below:

- We present the role of liquid compressibility in energy concentration and release during inertial collapse of a spherical gas bubble. We develop an improved approach for calculating energy transport during bubble collapse, which enables more accurate predictions of energy transport. We also provide closed-form expressions for the energy and size of the bubble at collapse in terms of the parameters governing the problem, which can account for the effects of liquid compressibility. We further provide an analytical model relating the shock pressure to the parameters governing the problem (Chapter 2).

- We identify the dependence of the bubble response and key shock properties on waveform parameters in ultrasound-driven bubble growth and collapse. We develop a framework to understand how energy is transferred from the wave to the system, and to distinguish the effect of viscosity and surface tension on energy transport in the system. This framework enables us to obtain the relationships describing bubble expansion during the growth and energy concentration at collapse based on the waveform properties. We further employ these relationships to predict damage potential in bubble growth in histotripsy (Chapter 3).
- We investigate the role of compressibility in the dynamics of a gas bubble collapsing near a rigid surface. By comparing direct simulations with potential flow calculations, we assess the effects of compressibility on the dynamics of the bubble and the re-entrant jet. We show that for a given jet thickness, there exists a time difference between the compressible and incompressible results. For the most part of the collapse, similar overall bubble kinematics were observed for both results after implementing a time shift. In the final stages of the collapse, observable discrepancies between the compressible and incompressible results are visible. Finally, we demonstrate how liquid compressibility plays a role in the dynamics of the bubble and re-entrant jet (chapter 4).

CHAPTER 2

Energy Concentration and Release during the Inertial Collapse of a Spherical Gas bubble in a Liquid

The inertial collapse of a cavitation bubble concentrates energy into a small volume and subsequently releases it into the surroundings in the form of a shock wave. While the incompressible solution to this problem is known and effectively governed by a single parameter (the normalized initial pressure ratio), the compressible version additionally depends on a measure of compressibility. The present chapter examines the role of compressibility on energy concentration and release during inertial collapse of a spherical gas cavity. This work improves both the methods for and understanding of this problem in several ways. First, a correction is made to the calculation of energy losses due to compressibility effects, thus enabling more accurate predictions of energy transport. We also provide closed-form expressions for the energy and size of the bubble at collapse (i.e., at minimum volume) in terms of the parameters governing the problem, which account for the effects of compressibility. Finally, we develop an analytical model relating the shock pressure to the parameters governing the problem.

2.1 Introduction

When a cavitation bubble reaches a size much greater than its equilibrium radius (Noltingk & Neppiras, 1950; Flynn, 1975a,b; Leighton, 2012; Gaudron *et al.*, 2015; Barajas & Johnsen, 2017), its collapse is inertially dominated: driven by the pressure difference between the far field and its contents, the bubble collapses as inward-rushing liquid confines the non-condensible gas inside the bubble and vapor condenses. Under such conditions, cavitation bubbles undergo a rapid compression such that the bubble volume decreases by several orders of magnitude between its maximum and minimum sizes. This collapse concentrates energy into a small volume, thereby producing high localized pressures/temperatures and emitting a pressure wave (or shock wave) propagating radially outward, with the potential to damage neighboring objects (Plesset & Prosperetti, 1977; Arndt, 1981; Johnsen & Colonius, 2009; Kim & Kim, 2014; Beig *et al.*, 2018). Cavitation-bubble collapse gives rise to a variety of outcomes, including erosion of metallic structures (e.g., naval propellers (Knapp *et al.*, 1970; Plesset & Prosperetti, 1977), turbomachinery (Arndt, 1981), the Spallation Neutron Source target (Riemer *et al.*, 2014; Winder *et al.*, 2020)), damage to soft materials (e.g., ultrasound-generated tissue homogenization (Xu *et al.*, 2004; Maxwell *et al.*, 2009)), ice formation (Hunt & Jackson, 1966; Hickling, 1994), and medical treatments (removal of calcified coronary stenoses (Brinton *et al.*, 2019; Karimi Galougahi *et al.*, 2020) and drug delivery to the brain (Pouliopoulos *et al.*, 2020; Todd *et al.*, 2020)). Predicting such outcomes requires an accurate description of the collapse process and associated transient pressure fields. In particular, shock waves are known to play an important role in cavitation-induced damage (Rayleigh, 1917; Hickling & S., 1964; Vogel *et al.*, 1989; Johnsen & Colonius, 2009; Kim *et al.*, 2014; Supponen *et al.*, 2017).

Although in practice bubbles are commonly observed to collapse in a non-spherical fashion due to symmetry-breaking actions such as the presence of a solid object or an accelerating field (Tomita & Shima, 1986; Vogel *et al.*, 1989, 1996; Johnsen & Colonius, 2009; Supponen *et al.*, 2016, 2017; Beig *et al.*, 2018), a large body of theoretical investigations have considered spherical bubble dynamics (Besant, 1948; Rayleigh, 1917; Plesset, 1949; Gilmore, 1952; Keller & Kolodner, 1956; Flynn, 1975a; Plesset & Prosperetti, 1977; Keller & Miksis, 1980; Vogel *et al.*, 1989; Prosperetti, 1991; Brennen, 1995; Leighton, 2012; Tinguely *et al.*, 2012; Obreschkow *et al.*, 2013). In fact, careful experiments (Supponen *et al.*, 2016, 2017) demonstrate that in the absence of perturbations bubbles can remain highly spherical until the very last instants of collapse. The present work examines spherical bubble dynamics as a limiting case that most effectively concentrates energy. Assuming incompressible flow of the surrounding liquid, spherical bubble dynamics are determined by the Rayleigh–Plesset (RP) nonlinear ordinary differential equation (Rayleigh, 1917; Plesset, 1949). From its maximum size, an inertially collapsing bubble converts potential energy into kinetic energy of the surroundings. The kinetic energy is itself converted to internal energy of the bubble at collapse. The resulting pressure build-up inside the bubble causes the bubble to eventually rebound. In the surrounding medium, the transient pressure fields thereby produced can readily be determined (Brennen, 1995):

$$p_l(r,t) = p_\infty + \rho_l \left(\frac{R^2 \ddot{R} + 2R\dot{R}^2}{r} \right) - \frac{\rho_l}{2} \left(\frac{R^4 \dot{R}^2}{r^4} \right), \tag{2.1}$$

where p_l is the liquid pressure, p_∞ is the liquid pressure in the far field, ρ_l is the liquid density, R is the bubble radius, r is the radial position, and the dot denotes a time derivative. However, under inertially dominated conditions, velocities achieved in the liquid can be large enough that liquid compressibility effects cannot be neglected. Compressibility manifests in two primary ways: the accelerating bubble interface continuously radiates waves into the surroundings and energy is released at collapse in the form of a shock. Predicting the transient pressure fields produced by collapsing bubbles thus requires an accurate representation of both energy losses during collapse and shock generation/propagation. In particular, the dependence of the pressure on the parameters governing the problem has yet to be fully determined.

A variety of models have been developed to extend the RP equation to account for energy losses via acoustic radiation in a weakly compressible medium during collapse, such as the Herring (Herring, 1941), Keller–Kolodner (Keller & Kolodner, 1956), Keller–Miksis (Keller & Miksis, 1980), and Trilling (Trilling, 1952) equations. Herring (1941) and Keller & Kolodner (1956) introduced a first-order correction to consider the acoustic propagation of small perturbations in liquid, and Keller & Miksis (1980) further determined the effect of viscosity and surface tension on the acoustic radiation. Trilling (1952) used the hypothesis introduced by Kirkwood & Bethe (1942) to consider characteristics propagating with constant sound speed during bubble oscillations. The energy balance in the liquid-bubble system for these models has recently been investigated to obtain energy losses due to acoustic radiation. Holzfuss (2010), and Fortes-Patella *et al.* (2013) evaluated the energy losses due to acoustic radiation, approximating the pressure field in the acoustic limit; Yasui *et al.* (2011) estimated the energy release through shock wave using acoustic theory. Wang (2016) developed an approach to calculate the energy losses by partitioning the liquid into near- and far-field regions, and Tinguely *et al.* (2012) quantified the energy release via shock wave, subtracting the change in the bubble internal energy during collapse and rebound and in potential energy of the liquid at the maximum radius after first rebound from the initial potential energy. However, as shown in the present study, the total energy evolution predicted by these models is not fully conserved.

Energy release into the surroundings as a shock has been investigated using theory (Kirkwood & Bethe, 1942; Arons & Yennie, 1948; Cole, 1948; Gilmore, 1952; Brennen, 1995; Geers & Hunter, 2002; Hunter & Geers, 2004), direct simulations (Johnsen & Colonius, 2009; Shaw & Spelt, 2010; Beig *et al.*, 2018), and experiments (Vogel *et al.*, 1996, 1989; Pecha & Gompf, 2000; Lauterborn & Kurz, 2010) with application to underwater explosions and bio-medical applications. The wave emitted upon collapse exhibits a blast profile expected in this diverging flow. The shock amplitude is a key quantity to estimate the damage induced by shock on the neighboring objects (Kirkwood & Bethe, 1942; Gilmore, 1952; Johnsen & Colonius, 2009; Shaw & Spelt, 2010), decaying inversely proportional to the shock radius or faster near the source of the shock (Cole, 1948; Arons, 1954; Shaw & Spelt, 2010; Holzfuss, 2010; Aganin & Mustafin, 2021). Determining the dependence of the shock peak pressure produced by bubble collapse on the initial conditions could thus improve predictions of cavitation-induced damage and enable the development of mitigation strategies.

The objective of this study is to determine the dependence of the maximum pressure produced some distance away by an inertially collapsing bubble on the parameters governing the problem. For this purpose, we developed an improved approach for calculating energy transport during bubble collapse, which enables us to understand the mechanisms by which energy is transferred and released into the shock. This understanding is critical to determine the relationship between the shock pressure and the parameters governing the problem, namely the driving pressure ratio and an effective Mach number. The chapter is organized as follows. First, an improved framework to calculate energy transfer for a bubble obeying the general Keller–Herring (KH) equation is introduced in section 2.2. This framework is used to examine energy transfer during bubble collapse in section 2.3, in which scaling relations are developed and comparisons to other approaches are made. Section 2.4 discusses specific regimes and different collapse types, including comparisons to experiments. Concluding remarks close the chapter in section 2.5.

2.2 Energy transport in bubble oscillations in a weakly compressible medium

2.2.1 Problem description and bubble dynamics equations

We seek to determine the dependence of the pressure produced by a collapsing bubble some distance away on the parameters governing the problem. Simply put, assuming we know the energy of our system at a given time (e.g., at maximum bubble radius), we expect the collapse to concentrate a fraction of this energy into the bubble at minimum volume and determine the dependence of the bubble properties at collapse on the parameters governing the problem. This bubble energy is then released as a shock, whose pressure we seek to relate to the bubble conditions at collapse. For simplicity, we start by considering the classical Rayleigh collapse problem (Rayleigh, 1917), illustrated in figure 2.1. A perfectly spherical bubble (Ω_B) in an infinite liquid (Ω_∞) is initially in thermal and mechanical equilibrium with its surroundings at pressure p_{eq} and temperature T_{eq}. For simplicity, the bubble is filled with non-condensible gas; mass transport could be included in the analysis but is beyond the present scope. An instantaneous increase in surrounding liquid pressure Δp from p_{eq} at $t = 0$ then initiates the collapse. This problem corresponds to the limiting case of

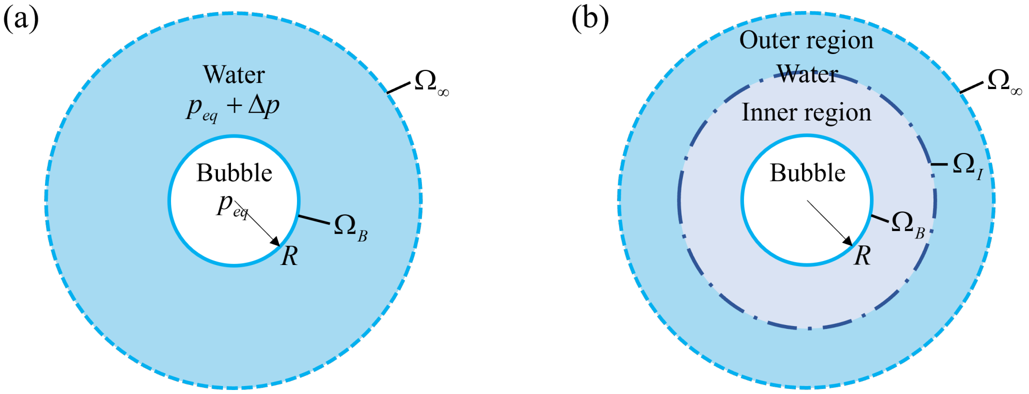

Figure 2.1: Schematics of Rayleigh collapse in (a) incompressible and (b) compressible media.

shock-induced collapse for an infinitely fast shock.

The classical incompressible analysis (Rayleigh, 1917; Plesset, 1949) considers the bubble to be in an infinite sea of liquid, as it would feel the presence of any foreign object in the liquid given the infinite sound speed, though the interaction may be weak. In a compressible medium, the bubble is informed of the presence of a boundary by the wave emitted at the beginning of collapse propagating to that boundary and reflecting back to the bubble. Taking the time from maximum to minimum volume, the Rayleigh collapse time (Rayleigh, 1917; Plesset, 1949; Brennen, 1995), it follows that a bubble beyond a critical distance δ_{cr} from the boundary,

$$\frac{\delta_{cr}}{R_o} \approx \frac{1}{2}\left[1 + 0.915\left(\frac{\rho_l a_l^2}{p_{eq}}\right)^{1/2}\left(\frac{p_{eq}}{\Delta p}\right)^{1/2}\right], \tag{2.2}$$

is not affected by the boundary during its collapse, where R_o is the initial maximum radius, and a_l is the speed of sound. It further follows that a spherical bubble starting its collapse at a distance greater than δ_{cr} from a boundary would remain spherical throughout its collapse. The dependence of the critical distance beyond which bubble collapse is expected to be spherical on the driving pressure ratio $\Delta p/p_{eq}$ is shown in figure 2.2. The right-hand side of Eq. (2.2) should be multiplied by 2 when considering the growth phase.

The oscillations of a spherical bubble in a weakly compressible liquid can be described, to first-order in effective Mach number $M = U/a_l$ based on the characteristic velocity $U = \sqrt{\Delta p/\rho_l}$,

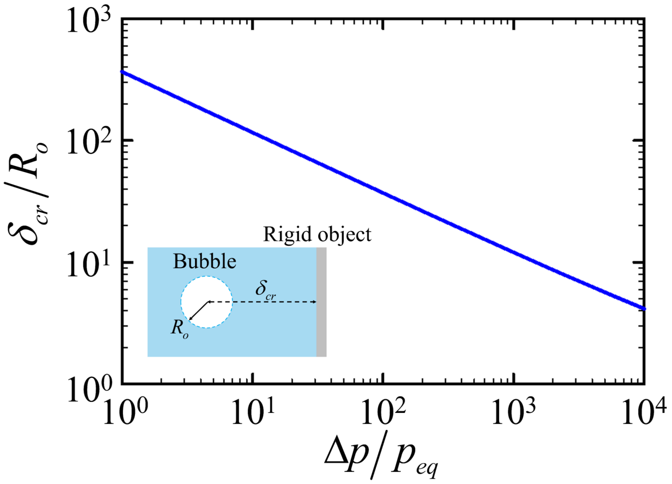

Figure 2.2: Critical stand-off distance δ_{cr} for a bubble not affected by the rigid object during collapse for Rayleigh collapse.

by a single-parameter family of equations for the bubble radius (Herring, 1941; Keller & Kolodner, 1956; Prosperetti & Lezzi, 1986):

$$R\ddot{R}\left[1-(\lambda+1)\frac{\dot{R}}{a_l}\right]+\frac{3}{2}\dot{R}^2\left[1-\left(\frac{3\lambda+1}{3}\right)\frac{\dot{R}}{a_l}\right]=\left(\frac{p_l-p_\infty}{\rho_l}\right)\left[1+(1-\lambda)\frac{\dot{R}}{a_l}\right]+R\frac{\dot{p}_l}{\rho_l a_l} \tag{2.3}$$

where p_l is the pressure at the bubble wall ($r = R$), λ is the model parameter ($0 \leq \lambda \leq 1$). Different values of λ correspond to different models for compressibility. For instance, the Keller–Kolodner (KK) (Keller & Kolodner, 1956) and Keller–Miksis (Keller & Miksis, 1980) equations require $\lambda = 0$ and the Herring equation (Herring, 1941) is obtained with $\lambda = 1$. Prosperetti & Lezzi (1986) recommend using the KK equation for the bubble collapse problem based on comparisons with numerical simulations. In the limit of $\dot{R}/a_l \to 0$, which is reasonable for relatively small-amplitude bubble oscillations, the incompressible limit (RP equation (Rayleigh, 1917; Plesset, 1949)) is recovered.

Balance of stresses at the bubble wall implies

$$p_b = p_l + 4\mu_l\frac{\dot{R}}{R} + \frac{2S}{R}, \tag{2.4}$$

where p_b is the gas pressure inside the bubble, μ_l is the dynamic viscosity of the liquid and S is the surface tension. The KK equation is Eq. (2.3), which, when combined with Eq. (2.4) yields the KM equation (Keller & Miksis, 1980). The bubble is assumed to contain a gas whose pressure follows the polytropic relation $p_b = p_{eq}(R_o/R)^{3k}$, where k is the specific heat ratio. The bubble can be assumed homobaric because the bubble–wall velocity is much smaller than the speed of sound in gas for most of the collapse (Prosperetti, 1991). The water properties are $\rho_l = 998$ kg/m^3 and $a_l = 1,510$ m/s. To solve the equation of motion, the Cash-Karp Runge-Kutta method (Barajas & Johnsen, 2017) is used for the time integration of the equation.

Using R_o and U to non-dimensionalize, Eq. (2.3) can be rewritten in dimensionless form:

$$\begin{aligned} R^*\ddot{R}^*\left[1-(\lambda+1)\,\dot{R}^*M\right]+\frac{3}{2}\dot{R}^{*2}\left[1-\left(\frac{3\lambda+1}{3}\right)\dot{R}^*M\right] &= \\ (p_l^*-p_\infty^*)\left[1+(1-\lambda)\,\dot{R}^*M\right]+R^*\dot{p}_l{}^*M&, \end{aligned} \tag{2.5}$$

and Eq. (2.4) is: $p_b^* = p_l^* + 4\dot{R}^*/R^*\mathrm{Re} + 2/R^*\mathrm{We}$, where the Reynolds number is $\mathrm{Re} = \rho_l U R_o/\mu_l$ and the Weber number is $\mathrm{We} = \rho_l U^2 R_o/S$. Here, $p_b^* = p_{eq}^*(1/R^*)^{3k}$. For given initial conditions R_o^* and $\dot{R}_o^*$, $R^*(t^*)$ is uniquely determined by two parameters, the driving pressure ratio $\Delta p/p_{eq}$, which is a measure of (static) compression of the bubble, and the effective Mach number $M = \sqrt{\Delta p/\rho_l a_l^2}$, which is a measure of compressiveness of the medium for a given driving pressure. In an incompressible limit, $R^*(t^*)$ is determined only by the driving pressure ratio provided $R_o^* = 1$ and $\dot{R}_o^* = 0$. In the following sections, we investigate the dependence of the bubble dynamics, energy transfer, and shock emission on $\Delta p/p_{eq}$ and M by varying these parameters in the ranges $0.8 \leqslant \Delta p/p_{eq} \leqslant 2.8 \times 10^3$ and $1.1 \times 10^{-3} \leqslant M \leqslant 6.6 \times 10^{-2}$. This driving pressure range is relevant to both shock-induced collapse and free collapse in shock-wave lithotripsy (Ohl & Ikink, 2003; Zhong, 2013) and inertial collapse of acoustically generated bubbles as well as underwater explosions (Cole, 1948; Hunter & Geers, 2004). The effective Mach numbers are selected such that compressibility effects are within a range accurately represented by the model.

In the present study, the KK equation forms the starting point of our analysis (Knapp *et al.*, 1970; Plesset & Prosperetti, 1977; Prosperetti & Lezzi, 1986; Holzfuss, 2010; Kim *et al.*, 2014;

Wang, 2016), and a bubble in incompressible limit using the RP equation is used as references cases. The initial bubble wall velocity is set to $\dot{R}_o = \Delta p/\rho_l a_l$ to account for the release corresponding to the initial Riemann problem when accounting for compressibility (Gilmore, 1952; Plesset & Prosperetti, 1977; Barajas & Johnsen, 2017); in the incompressible limit, $\dot{R}_o = 0$. For a bubble in the 10^2–10^3 μm range, the thermal boundary layer thickness $\sim \sqrt{\alpha \Delta t}$ (Prosperetti, 2017), where α is the thermal diffusivity, reaching $O(1)$ μm in the liquid and $O(10)$ μm in the gas. Although those length scales are comparable to the bubble radius in the very last stages of collapse [$\sim O(1)$ μm], they are only observed over nanoseconds, such that thermal conduction and phase change are considered negligible for inertial collapse (Johnsen & Colonius, 2009; Beig *et al.*, 2018; Prosperetti, 1991) and thus a polytropic representation of the bubble with $k = 1.4$ is satisfactory; these effects will be investigated in detail in subsequent work on thermal transport. The Reynolds number $O(10^3 - 10^5)$ and Weber number $O(10^1 - 10^5)$ are sufficiently large for a micro-to-millimeter size bubble such that the viscosity and surface tension are negligible as they would affect the bubble volume during collapse by less than a percent for the relevant range of parameters. The present discussion ignores gravity, whose role is argued to be negligible for micron- to millimeter-sized bubbles (Tinguely *et al.*, 2012; Obreschkow *et al.*, 2011).

As a baseline for this study, we consider driving pressure ratios of 27 and 280, which are relevant to therapeutic ultrasound. Figure 2.3 shows the time evolution of the bubble radius, with time non-dimensionalized by the Rayleigh collapse time $t_c = 0.915 R_o \sqrt{\rho_l / p_\infty}$ of an empty cavity. If the liquid and gas pressure are equal (equilibrium case), the bubble motion is stationary with no collapsing motion. While small-amplitude, linear oscillations result from infinitesimally small increases in liquid pressure, oscillations become nonlinear at high driving pressures, achieving high velocities and accelerations in the final stage of collapse. Discrepancies between the compressible and incompressible cases are negligible at low pressure ratios ($\Delta p/p_{eq} = 27$) since the effective Mach numbers are small (Prosperetti & Lezzi, 1986; Brennen, 1995). At high pressure ratios (e.g., $\Delta p/p_{eq} = 280$), differences are visible between the compressible and incompressible case, in particular in the minimum radius, maximum radius after rebound, and time for them. The bubble

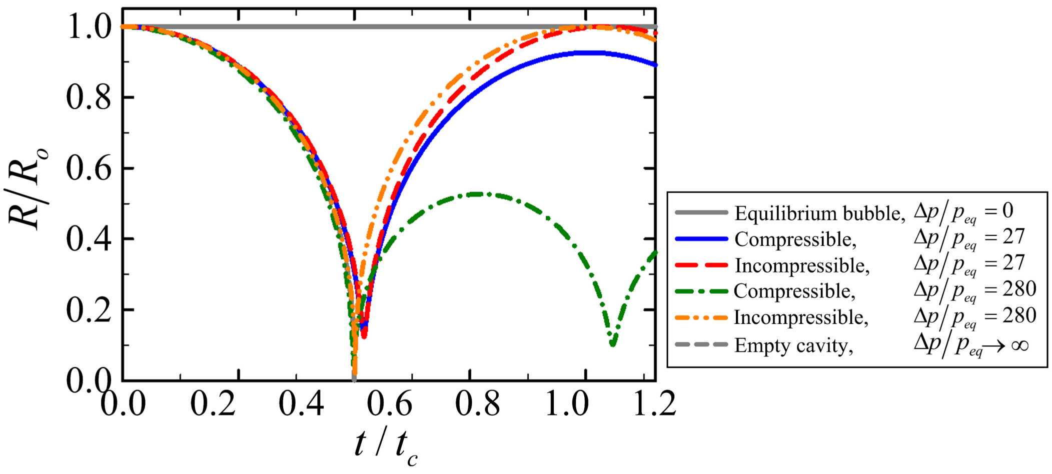

Figure 2.3: Time evolution of the bubble radius vs. bubble radius in one cycle for different pressure ratios for the compressible and incompressible cases, including the empty cavity case and an equilibrium bubble for reference.

radius during rebound is significantly damped in the compressible case, while in the incompressible limit, the initial bubble radius is recovered with no damping at maximum radius during rebound. In the incompressible limit, as the pressure ratio becomes large ($\Delta p/p_{eq} \to \infty$), the bubble radius tends to that of an empty cavity until the very last stages of collapse because the effect of gas inside the bubble is negligible for most of the collapse.

2.2.2 Energy transfer during bubble oscillations

Discrepancies between compressible and incompressible cases, as well as differences between the dynamics at different driving pressures, can be explained by examining energy transfer during the process. In our analysis, we take our system to consist of a bubble in a sea of liquid sufficiently large such that the velocity in the far-field is effectively zero. For an ideal, non-condensible gas, the bubble internal energy is

$$E_{BIE} = \int \rho_g e dV = \frac{p_b V}{k-1}, \tag{2.6}$$

where ρ_g is the gas density, e is the specific internal energy, and V is the bubble volume. The liquid near the bubble (inner region) has finite kinetic energy (Lamb, 1932; Cole, 1948; Pearson *et al.*, 2004; Wang, 2016)

$$E_{LKE} = \frac{\rho_l}{2}\left(\int_{\Omega_B} \varphi \frac{\partial \varphi}{\partial n} \mathrm{d}S + \int_{\Omega_I} \varphi \frac{\partial \varphi}{\partial n} \mathrm{d}S\right) = 2\pi \rho_l R^3 \dot{R}^2, \tag{2.7}$$

where Ω_B is the bubble wall, Ω_I is the outer boundary of the inner region, and S is the surface integral. We assume that temperature changes are small enough that changes in internal energy can be neglected. Given the conservative hydrostatic force acting on the liquid in the far-field, the potential energy stored in the liquid is (Arons & Yennie, 1948; Obreschkow *et al.*, 2006; Tinguely *et al.*, 2012; Vogel *et al.*, 1996)

$$E_{LPE} = p_\infty V. \tag{2.8}$$

Other energy modes related to the thermal conduction, viscosity, and surface tension are neglected in this study.

Given that the liquid is compressible, acoustic waves may leave the outer boundary, thus giving rise to energy losses due to acoustic radiation. This mode of energy transfer requires discussion. We start our analysis by following that of Prosperetti & Lezzi (1986) and extend it to more accurately represent acoustic radiation losses by summing up the energy transferred by waves propagating away from the bubble. As illustrated in figure 2.1(b) for weakly compressible analysis, we divide the liquid into two sub-regions of sizes determined by characteristic lengths relevant to bubble oscillations Prosperetti & Lezzi (1986); Prosperetti (1987). Near the bubble (inner region), the bubble oscillations induce liquid motion with characteristic length scale R_o; the near-field flow can be assumed solenoidal since the characteristic time corresponding to pressure wave propagation is much shorter than the collapse time. On the other hand, far from the bubble (outer region), velocity changes are primarily due to wave propagation. Linear acoustics reasonably approximate the dynamics, with characteristic length scale $a_l(R_o/U)$. Taking appropriate limits based on the ratio $\epsilon = U/a_l$, which corresponds to an effective Mach number, singular perturbation analysis can be used to match the velocity potential and enthalpy at the outer boundary of the inner region to those at the inner boundary of the outer region. The equation of motion for bubble radius and velocity potential can be expressed, to order ϵ^2

$$\frac{\dot{F}}{R} - \frac{F^2}{R^4} - \frac{\ddot{F}}{a_l} = \frac{p_l - p_\infty}{\rho_l}, \qquad \varphi = -\frac{F}{r} + \frac{\dot{F}}{a_l}, \tag{2.9}$$

where φ is the velocity potential, and the function $F = R^2\dot{R} = \dot{V}/4\pi$. This equation can be rewritten as (Prosperetti & Lezzi, 1986; Prosperetti, 1987, 1991)

$$R\ddot{R} + \frac{3}{2}\dot{R}^2 - \frac{\ddot{F}}{a_l} = \frac{p_l - p_\infty}{\rho_l}, \qquad \text{where} \qquad \ddot{F} = 2\dot{R}^3 + 6R\dot{R}\ddot{R} + R^2\dddot{R}. \tag{2.10}$$

However, it is a well-known problem in acoustics that a solution growing exponentially in time is obtained when a perturbation theory is applied inappropriately (Burke, 1970; Templin, 1999; Keller & Miksis, 1980; Prosperetti & Lezzi, 1986). To avoid this divergent solution, the third-order derivative of R is replaced by low-order derivatives while confining the error to order of ϵ^2 (Keller & Miksis, 1980; Prosperetti & Lezzi, 1986). Taking the derivative of Eq. (2.9) yields

$$\ddot{F} = \frac{\dot{R}^3}{2} + R\dot{R}\ddot{R} + \dot{R}\left(\frac{p_l - p_\infty}{\rho_l}\right) + R\frac{\dot{p}_l}{\rho_l}, \tag{2.11}$$

where the $O(\epsilon)$ term is ignored. The KK equation (2.3) (Keller & Kolodner, 1956) is obtained by substituting Eq. (2.11) into Eq. (2.10). Expressing $\ddot{F}$ as $\lambda\ddot{F} + (1-\lambda)\ddot{F}$ and using the RP equation and Eq. (2.11), we obtain:

$$\ddot{F} = (1+3\lambda)\frac{\dot{R}^3}{2} + (1+\lambda)R\dot{R}\ddot{R} + (1-\lambda)\dot{R}\left(\frac{p_l - p_\infty}{\rho_l}\right) + R\frac{\dot{p}_l}{\rho_l}. \tag{2.12}$$

By substituting Eq. (2.12) into Eq. (2.10), the general KH equation (2.3) is obtained (Prosperetti & Lezzi, 1986).

The first law of thermodynamics requires the change in energy at any given time relative to the initial energy to be balanced as follows:

$$p_\infty V_o + \frac{p_{b,o} V_o}{k-1} + 2\pi\rho_l R_o^3 \dot{R}_o^2 = p_\infty V + \frac{p_b V}{k-1} + 2\pi\rho_l R^3 \dot{R}^2 + E_{AE}, \tag{2.13}$$

where E_{AE} is the acoustic radiation energy (i.e., energy losses due to acoustic radiation). All energy terms except for the last term are introduced in Eqs. (2.6)–(2.8). The last term E_{AE} should be evaluated accurately for not violating energy balance.

Thus, following the framework introduced above by (Prosperetti & Lezzi, 1986), we propose an approach to more accurately calculate E_{AE}. The energy of pressure waves perturbing the liquid near the bubble can be computed at the outer boundary of the inner region:

$$E_{AE} = \int_0^t \left[\lim_{\Omega_l \to \infty} \int_{\Omega_l} (p_l - p_\infty)\, u_r \mathrm{d}S \right] \mathrm{d}t, \tag{2.14}$$

where E_{AE} is the acoustic radiation energy, and $u_r = \mathrm{d}\varphi/\mathrm{d}r$ is the liquid velocity. Here, E_{AE} is evaluated by integrating the energy flux along the outer boundary. In a weakly compressible liquid (acoustic limit), pressure waves propagate with no dissipation such that these pressure waves transport energy away from the bubble. Hence, E_{AE} is evaluated at the outer boundary of the inner region infinitely far from the bubble center, at which the initial far–field pressure is only modified by pressure waves emitted from the bubble wall. Using Eq. (2.9), the acoustic radiation energy is

$$E_{AE} = -\frac{4\pi\rho_l}{a_l} \int_0^t F \ddot{F} \mathrm{d}t. \tag{2.15}$$

Plugging Eq.(2.12) into Eq. (2.15) yields the explicit form of E_{AE}, which satisfies energy balance in Eq. (2.13). Again, λ is a model parameter in the general KH equation; in this study, since the KK equation is used, $\lambda = 0$ is used for obtaining E_{AE}. For other choices of λ, the general KH equation produces equations to first-order in ϵ with considering weak compressibility of liquid, and same choices of λ should be used for Eq. (2.15) to accurately calculate E_{AE}. In past studies (Wang, 2016; Yasui *et al.*, 2011; Holzfuss, 2010; Herring, 1941), theories underlying the KH equation introduced in this section are not considered and E_{AE} is explicitly calculated using acoustic theory, such that E_{AE} are not obtained accurately and energy balance [Eq. (2.13)] cannot be satisfied. In the incompressible limit, the last term of Eq. (2.13) is zero. In Table 2.1, our approach and several past approaches (Wang, 2016; Yasui *et al.*, 2011; Holzfuss, 2010; Herring, 1941) for calculating E_{AE} are introduced, and they are compared in the next section.

2.3 Results

2.3.1 Analysis of energy transport during bubble collapse

We first examine energy transport during the collapse and the early rebound stage of a gas bubble corresponding to the nominal cases in figure 2.3, investigate the effects of compressibility on the energy transport, and assess performance of the different approaches.

Figures 2.4(a) and 2.4(b) shows the time evolution of the total energy (E), the liquid potential energy (PE) and kinetic energy (KE), the bubble internal energy (IE), and the acoustic radiation

Table 2.1: Previous approaches for energy losses due to acoustic radiation.

Present approach	$E_{AE} = -\dfrac{4\pi\rho_l}{a_l}\displaystyle\int_0^t F\ddot{F}\mathrm{d}t$	
Wang (2016)	$E_{AE} = -\dfrac{\rho_l}{4\pi a_l}\left[\dot{V}(t)\ddot{V}(t) - \dot{V}(0)\ddot{V}(0) - \displaystyle\int_0^t \ddot{V}^2\mathrm{d}t\right]$	(2.16)
Yasui *et al.* (2011)	$E_{AE} = \dfrac{\rho_l}{4\pi a_l}\displaystyle\int_0^t \ddot{V}^2\mathrm{d}t$	(2.17)
Holzfuss (2010)	$E_{AE} = \dfrac{4\pi}{\rho_l a_l}\displaystyle\int_0^t R^2\left(p_l - p_\infty + \dfrac{\rho_l\dot{R}^2}{2}\right)^2\mathrm{d}t$	(2.18)
Herring (1941)	$E_{AE} = -\dfrac{4\pi}{a_l}\displaystyle\int_0^t \dot{p}_l R^3\dot{R}\mathrm{d}t$	(2.19)

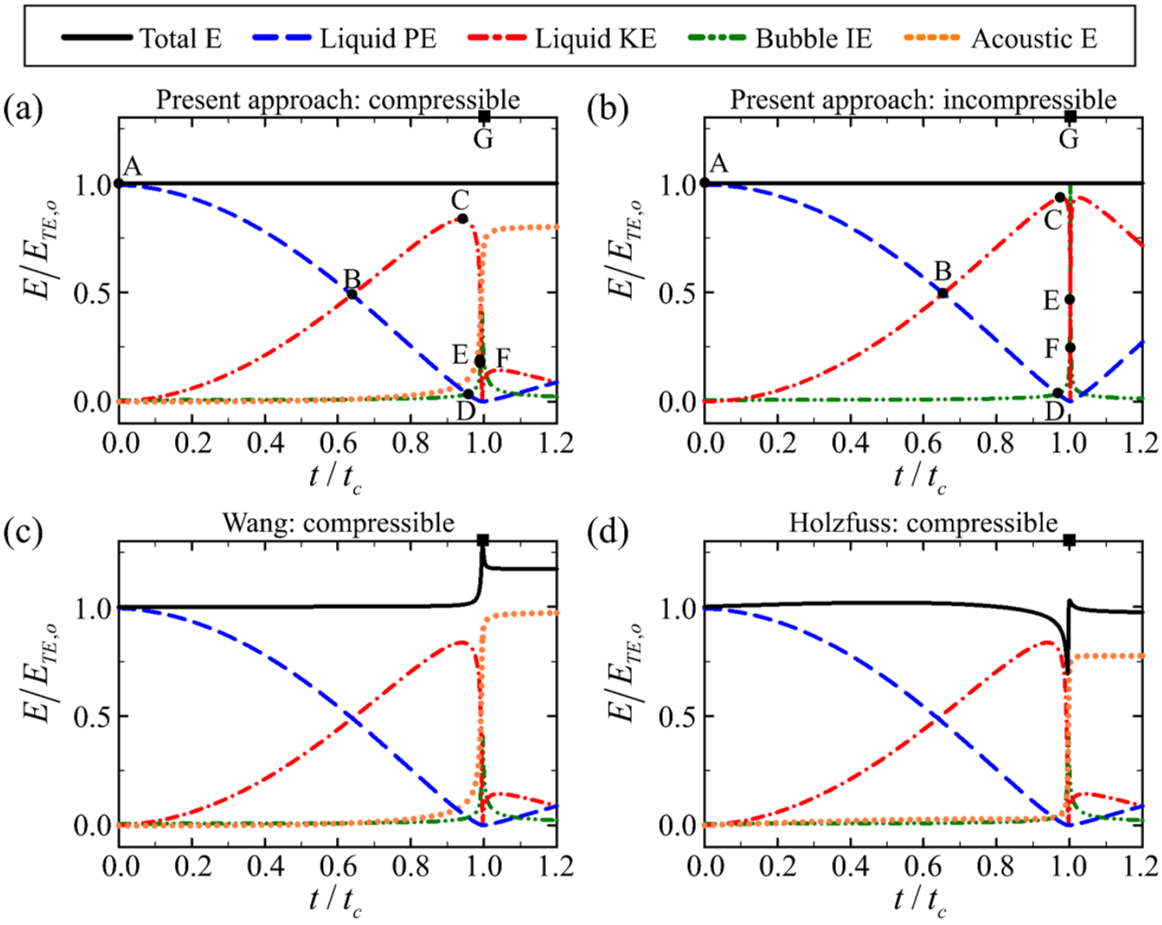

Figure 2.4: Time evolution of each mode of energy normalized by the initial total energy $E_{TE,o}$ during collapse and early rebound of a gas bubble for the (a,c,d) compressible and (b) incompressible cases at $\Delta p/p_{eq}$ =280. A to G marked in (a) an (b) imply the events for characterization of the energy transport, which are introduced in Table 2.2.

energy for an driving pressure ratio of $\Delta p/p_{eq} = 280$. For a better description of the local energy transport in the system, we choose the specific events, A to G, at which important phenomena occur, introduced in Table. 2.2. In both the compressible and incompressible cases, the liquid only contains the potential energy at the initial instant (event A). During collapse, a converging motion of the bubble wall leads to the increase in the kinetic energy of the liquid. Simultaneously,

Table 2.2: Important events during bubble collapse.

Label	A	B	C	D	E	F	G
Event	$t=0$	$E_{LPE}=E_{LKE}$	max E_{LKE}	$E_{LPE}=E_{BIE}$	$E_{LKE}=E_{BIE}$	max $\dot{R}$	$t=t_{col}$

the pressure at the interface works on the bubble, such that the more energy is concentrated to the bubble. Hence, as the bubble collapses, the potential energy initially stored in the liquid is transferred to the kinetic energy of the liquid and the internal energy of the bubble. In the early stage of the collapse, a greater portion of the total energy is transferred to the liquid kinetic energy than the bubble internal energy, leading to event B when $E_{LPE} = E_{LKE}$. In the compressible case, as the bubble collapses more, E_{LKE} reaches the maximum (event C), and thereafter, E_{LPE} reduces to become equal to E_{BIE} (event D). However, in the incompressible limit, the order of these two events are reversed. Then, after some time, E_{LKE} decreases and becomes equal to the rising E_{BIE} (event E). Prior to collapse when the bubble reaches to minimum volume, $\dot{R}$ has the maximum value (event F), and finally at collapse (event G), $\dot{R} = 0$, such that $E_{LKE} = 0$. In particular, in the compressible cases, a less amount of the initial E_{LPE} is concentrated to the bubble in the final stage of collapse due to E_{AE}, compared with the incompressible limit.

We turn our attention to the assessment of different approaches for E_{AE} calculation in figures 2.4(a), 2.4(c), and 2.4(d). Our approach is compared to that of Wang (2016) and that of Holzfuss (2010); results with the approach of Yasui *et al.* (2011) and Herring (1941) are not considered since the former is very similar to that of Wang (2016) and the latter is only related to the Herring equation. During the oscillation, the total energy should be always equal to the initial total energy because of the balance of the mechanical energy in the liquid–bubble system. In the case where the present approach [equation (2.15)] is employed, E_{TE} has no deviation from one [figure 2.4(a)]. However, E_{TE} is deviated from one when Wang's approach [equation (2.16)] is used, as shown in figure 2.4(c). In addition, there exist larger deviations in the total energy when Holzfuss's approach [equation (2.18)] is employed, as shown in figure 2.4(d). Thus, these results verify that our approach has a high fidelity on E_{AE} calculation. It should be noted that, the KK equation, which is equivalent to equation (2.3) with $\lambda = 0$, is used, and the same analysis can be conducted for the Herring equation, which is equivalent to equation (2.3) with $\lambda = 1$.

To better understand the effects of compressibility on the local details of energy transport, a portion of each energy mode at event A to G in the compressible and incompressible cases is

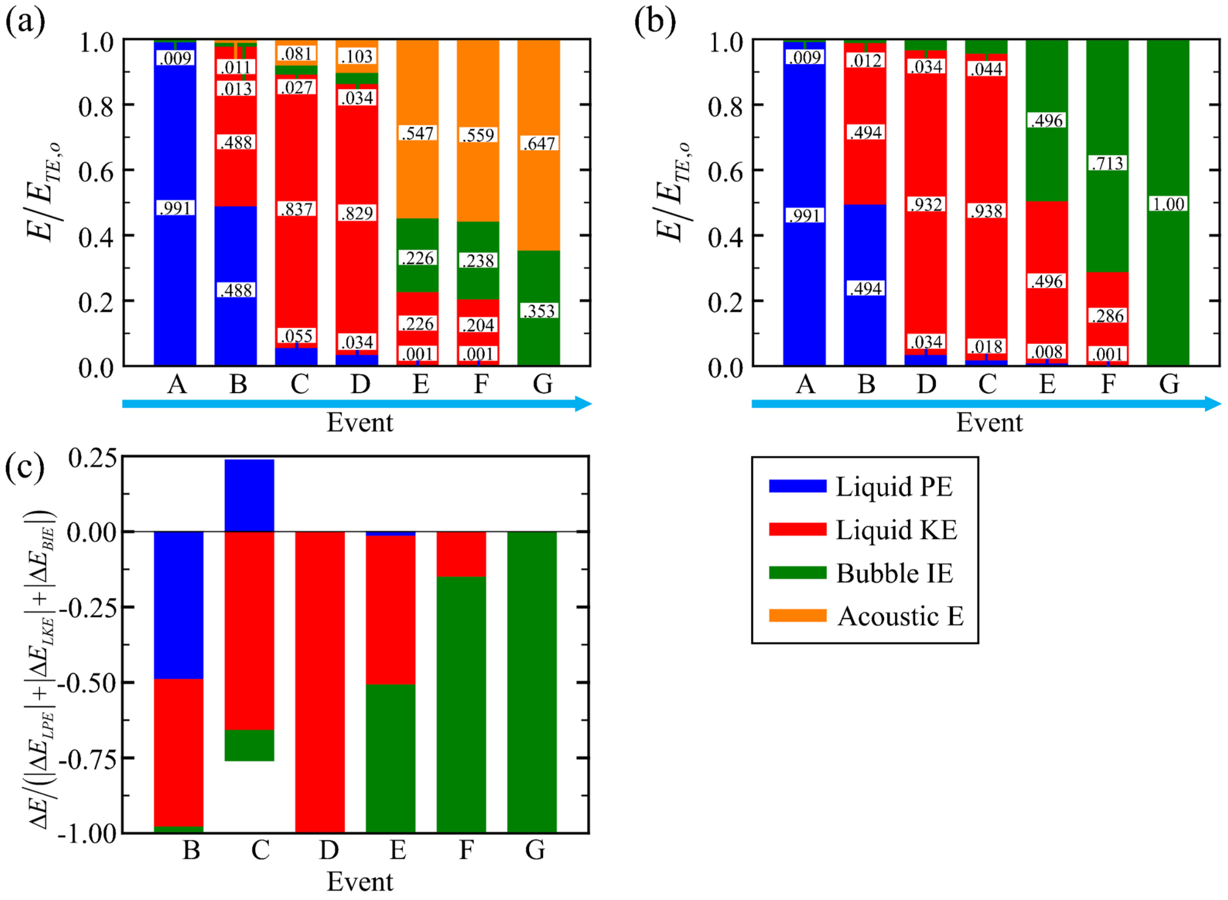

Figure 2.5: Energy partitions at event A to G characterizing the energy transport during collapse at $\Delta p/p_{eq} = 280$ for the (a) compressible and (b) incompressible cases. (c) The portions of energy differences at event B to G evaluated by subtracting the energy in the incompressible limit from that in the compressible liquid; the differences in E_{LPE}, E_{LKE} and E_{BIE}.

compared in figures 2.5(a) and 2.5(b). Although the trend in the direction of energy transport between each energy mode is similar in both cases, the magnitude of each energy mode at time A to G in the compressible case is somewhat affected by the energy losses due to acoustic radiation occupying some portion of the total energy in later times. Figure 2.5(c) depicts differences in each energy mode (i.e., E_{LPE}, E_{LKE}, and E_{BIE}) ΔE by subtracting the energy mode in the incompressible limit from that in the compressible case at a given event (i.e., event B to G), normalized by the sum of these three energy modes. For most of the events, ΔE_{LKE}, $\Delta E_{BIE} < 0$ because the bubble and near-field liquid lose their energy acoustically during collapse, such that E_{LKE} and E_{BIE} in the compressible case are smaller those in the incompressible limit. At event B ($E_{LPE} = E_{LKE}$),

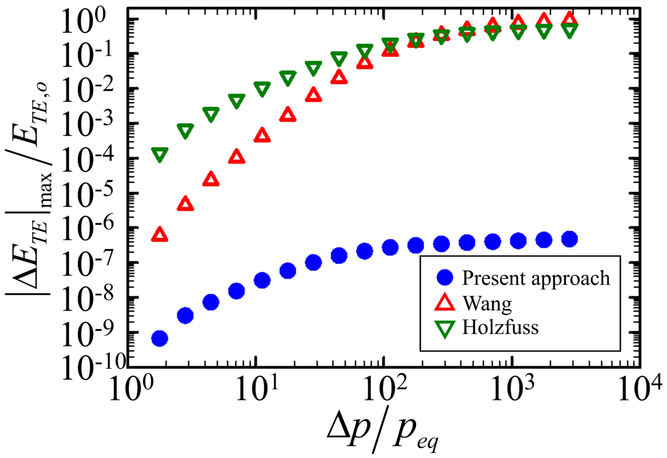

Figure 2.6: Absolute value of maximum deviations of the total energy $|\Delta E_{TE}|_{\max}$ during collapse and rebound for different approaches used to calculate energy losses due to acoustic radiation; solid circles: present approach, open upward triangles: Wang (2016), open downward triangles: Holzfuss (2010).

$\Delta E_{LPE} = \Delta E_{LKE}$. At event C (maximum E_{LKE}) and D ($E_{LPE} = E_{BIE}$), the liquid primarily loses its kinetic energy due to acoustic radiation, so most of the energy losses are observed in E_{LKE} at this time. From time D to G occurring in the moderate and final stage of the collapse, the losses in E_{LKE} decrease while the losses in E_{BIE} increase. In particular, $\Delta E_{LKE} = \Delta E_{BIE}$ at event E ($E_{LKE} = E_{BIE}$). As time evolves, ΔE_{LPE} becomes negligible. Overall, the lower values of E_{LKE} in the compressible case due to acoustic radiation also give rise to the lower values of E_{BIE} at collapse.

2.3.2 Dependence of energy transport during collapse on driving pressure ratio

The deviations of the total energy during collapse and rebound from its initial value for different approaches to evaluate E_{AE} [equations (2.15), (2.16), and (2.18)], shown in figure 2.4, depend on the driving pressure ratios primarily determining the energy losses due to acoustic radiation. Figure 2.6 shows the absolute value of maximum deviations of the total energy from its initial value for different approaches. For larger pressure ratios, the deviations for all approaches rise because large energy is lost through acoustic radiation. The deviations in our approach are ranging from $O(10^{-10})$ to $O(10^{-7})$ occurring in the integration of equation (2.15). However, as depicted in figure

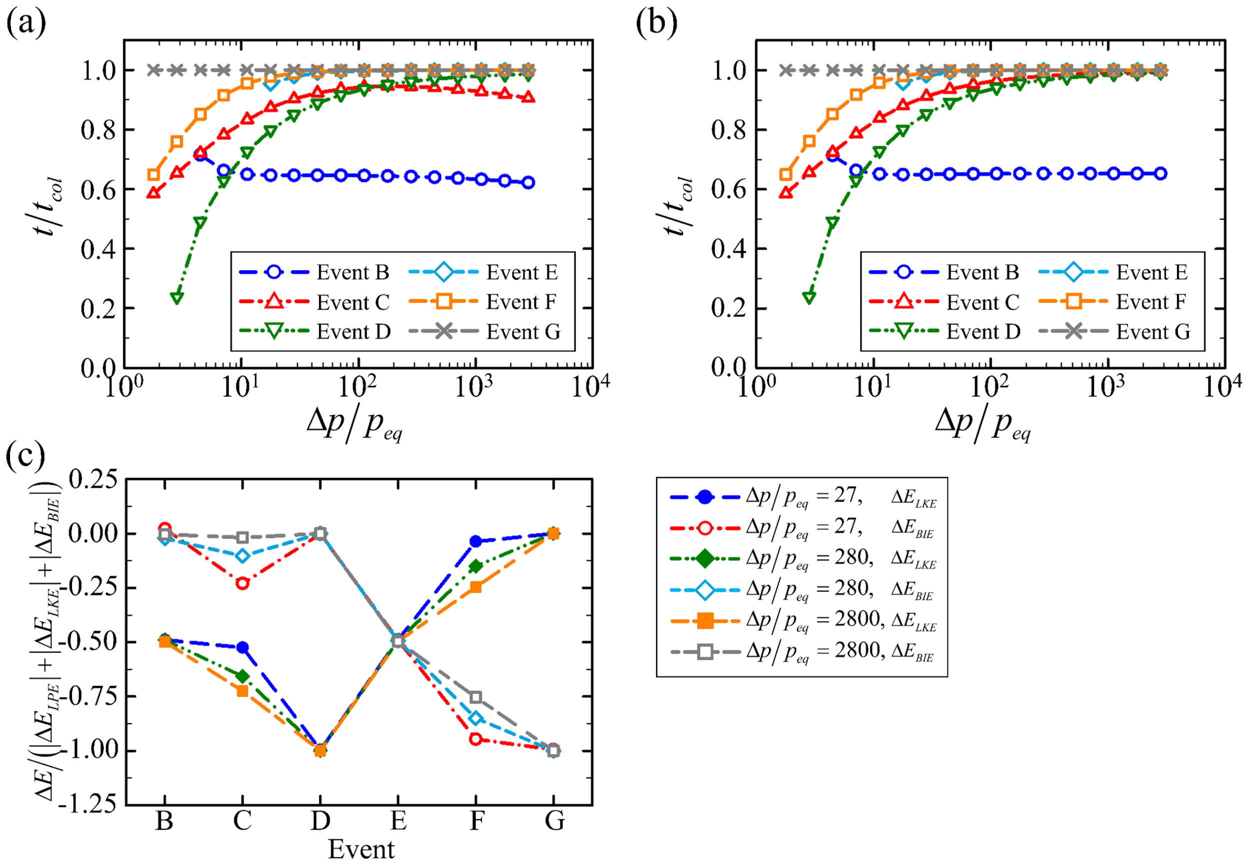

Figure 2.7: Event B to G normalized by the actual collapse time t_{col} as a function of driving pressure ratios for the (a) compressible and (b) incompressible cases. The portions of differences in E_{LKE} and E_{BIE} at event B to G evaluated by subtracting the energy in the incompressible limit from that in the compressible case for $\Delta p/p_{eq}$ = 27, 280, and 2800.

2.4, other approaches [equations (2.16) and (2.18)] produce larger deviations comparable to the initial energy at larger pressure ratios. Our approach thus shows a better performance, specifically at larger pressure ratios where the compressibility effects are crucial.

The order and time of events introduced in Table 2.2 reveal the direction and speed of the energy transport during collapse. Figures 2.7(a) and 2.7(b) show event B to G normalized by the actual collapse time t_{col}. Overall, the event B is observed earlier than other events, and event E to G occur in sequence. However, there exists the reverse of the order of event C and D in the compressible case because the acoustic radiation in a compressible liquid pushes event C forward while postponing event D. Thus, at low pressure ratios ($\Delta p/p_{eq} < 180$), event D is observed earlier than event C while it is reversed at high pressure ratios ($\Delta p/p_{eq} > 180$). In addition, at very low pressure ratios ($\Delta p/p_{eq} < 9$), event D occurs earlier than event B because the initial potential energy of the liquid is comparable to the initial internal energy of the bubble in this regime, such that they become equal at earlier times. For both cases, as the driving pressure ratios are increased, the collapsing motion of the bubble and corresponding energy transport become violent, such that a gap between events decreases. We note that event B and E are not observed at low pressure ratios where the energy transport is less violent, leading no crossover between E_{LPE}, E_{LKE}, and E_{BIE}.

Figure 2.7(c) demonstrates the portions of ΔE_{LKE} and ΔE_{BIE} at $\Delta p/p_{eq} = 27$, 280, and 2800. As also illustrated in the figure 2.5(c), greater losses are observed for E_{LKE} than in E_{BIE} in the earlier stage of the collapse (event B to E) while the opposite occurs in the later stage of the collapse (event E to G). At higher pressure ratios, the instant for event B to G occurs at later times, such that a more portion of the energy losses arises in the kinetic energy.

2.3.3 Bubble volume and energy at collapse

During the collapse, the potential energy in liquid is concentrated to the bubble, and some of the energy in the bubble is released through a high-amplitude (or shock) wave produced at collapse. A larger fraction of total energy confined in a smaller volume as internal energy at collapse leads to a stronger explosion, i.e., stronger emitted pressure/shock wave. In the following, we examine the dependence of various dynamically and energetically relevant quantities at collapse on the two parameters characterizing the problem, namely the driving pressure ratio and effective Mach number, which are linearly proportional to each other in the Rayleigh collapse. Figure 2.8 shows the dependence of the liquid potential energy, bubble internal energy, and acoustic radiation energy normalized by the initial total energy on the driving pressure ratio. As demonstrated in figures 2.4 and 2.6, our approach naturally conserves total energy. At low pressure ratios ($\Delta p/p_{eq} \sim 0.7$), nearly 80% of the initial total energy is concentrated into bubble internal energy, with the remaining being liquid potential energy. As the pressure ratio is increased, the fraction of bubble internal energy increases until $\Delta p/p_{eq} \approx 10$ at which point acoustic energy losses are no longer negligible. As the pressure ratio is further increased, energy losses due to acoustic radiation increase to 95%

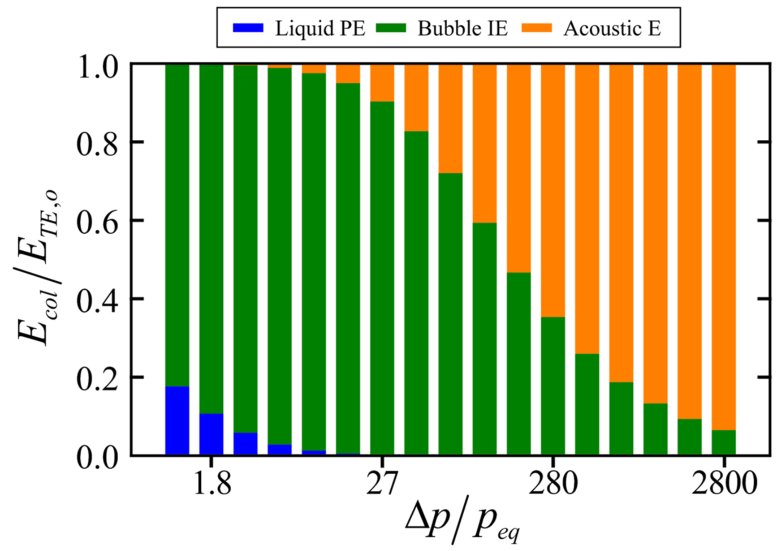

Figure 2.8: Energy partitions at collapse for a wide range of driving pressure ratios. x axis is uniformly spaced in log scale, and $\Delta p/p_{eq} = 2.7$, 28, 280, and 2800 are marked on the x axis.

of the initial energy for $\Delta p/p_{eq} \approx 2800$.

As the bubble energy and size at collapse provide the "initial conditions" for the energy release, we examine the role of compressibility on the energy and minimum volume at collapse. Figures 2.9(a)–2.9(c) show the dependence of the bubble volume, the bubble internal energy, and the energy losses due to acoustic radiation through the collapse, normalized by initial total energy, on the intial pressure ratio for the compressible and incompressible cases. The compressibility of the liquid, via acoustic radiation, is the reason that the bubble is less compressed and the efficiency of energy concentration into the bubble is reduced at collapse, compared to the incompressible limit. Higher pressure ratios lead to smaller volume at collapse for both cases while causing larger discrepancies between them. For the compressible case shown in figure 2.9(b), the normalized bubble internal energy has a local maximum at $\Delta p/p_{eq} \approx 17$, and when $\Delta p/p_{eq} > 17$ the bubble loses a significantly greater fraction of internal energy through acoustic radiation due to the higher bubble wall velocities and M. Figure 2.9 shows the bubble internal energy at collapse normalized by the initial internal energy. In both cases, as the driving pressure ratio is increased, a greater amount of energy is concentrated to a smaller bubble volume because the larger potential energy is initially stored in liquid at higher pressure ratios, such that a stronger shock is produced at collapse. The

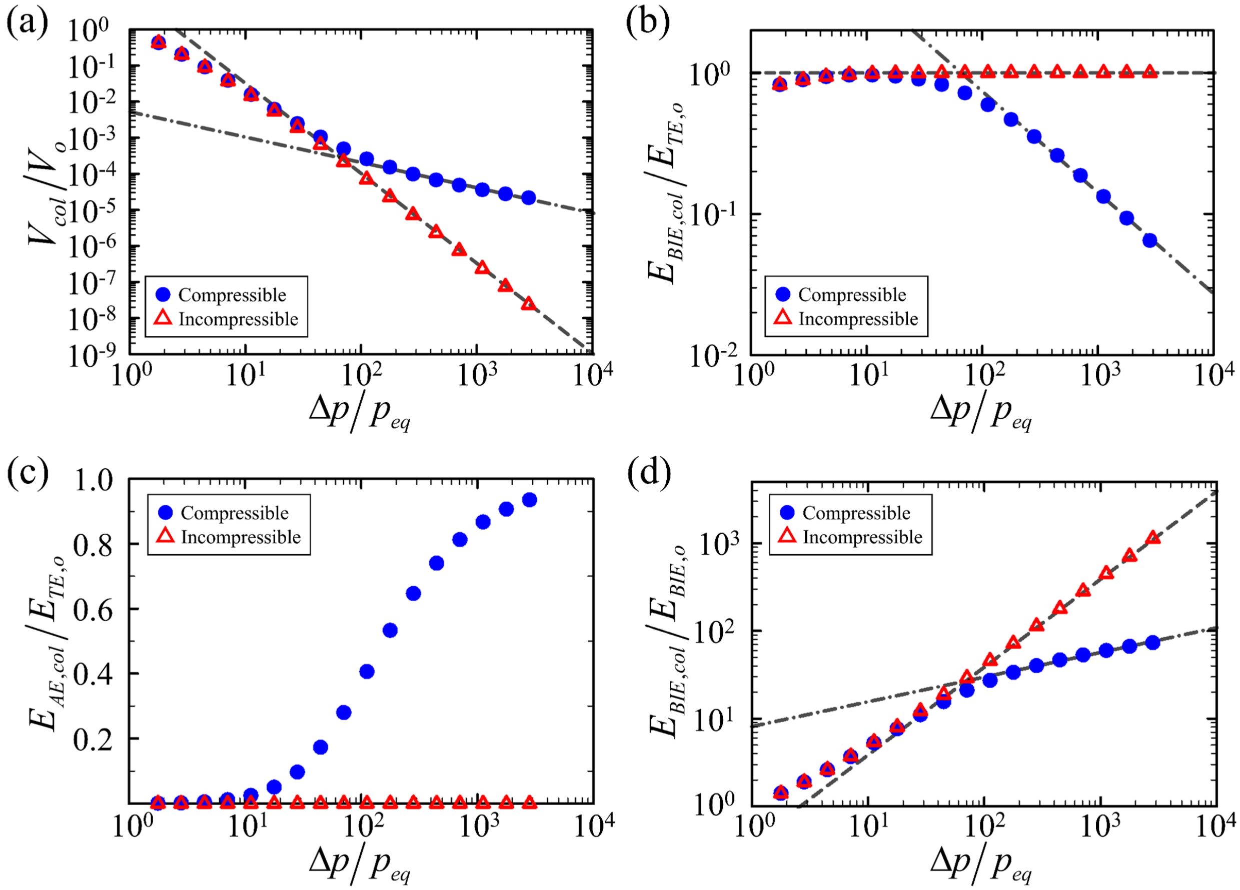

Figure 2.9: (a) Bubble volume, (b) bubble internal energy at collapse and (c) energy losses due to acoustic radiation through the collapse normalized by initial total energy, and (d) bubble internal energy at collapse normalized by initial internal energy for the compressible (solid circles) and incompressible (open triangles) cases as a function of driving pressure ratios; dashed line: (a) equation (2.24), (b) equation (2.26), and (d) equation (2.28); dash-dotted line: (a) equation (2.23), (b) equation (2.25), and (d) equation (2.27).

liquid compressibility significantly reduces the bubble internal energy at collapse, compared to the incompressible limit.

To explain the behaviors observed in figures 2.9, we analyze the energy balance equation to obtain scalings for limiting cases. At high pressure ratios (i.e., for highly compressible cases), a large fraction of energy is lost through acoustic radiation, such that

$$p_\infty V_o \approx -\frac{4\pi\rho_l}{a_l}\int_0^{t_{col}} F\ddot{F}\mathrm{d}t = F(t_{col})\dot{F}(t_{col}) - F(0)\dot{F}(0) - \int_0^{t_{col}} \dot{F}^2\mathrm{d}t. \tag{2.20}$$

where on the right-hand side, the first term is zero because $\dot{R}(t = t_{col}) = 0$, and the second term is negligible because $\dot{R}(t = 0)$ is small. Using equation (2.9), the time derivative of the function F can then be expressed as

$$\dot{F} \approx R\left(\dot{R}^2 + \frac{p_b - p_\infty}{\rho_l}\right) + O(\epsilon), \tag{2.21}$$

where $\epsilon = U/a_l$. As observed in figure 2.4(a), at high pressure ratios, most of the energy losses are accumulated in the final stage of the collapse where the gas pressure inside the bubble dominates the motion of the bubble–wall. Therefore, $\dot{F} \approx p_{b,col}R_{col}/\rho_l$ in the third term of equation (2.20) where $p_{b,col}$ is the gas pressure inside the bubble at collapse. Substituting this relation into equation (2.20) gives

$$p_\infty V_o \sim \frac{4\pi\rho_l}{a_l} R_{col}^2 \left(\frac{p_{b,col}}{\rho_l}\right)^2 t_c, \tag{2.22}$$

where the time scale in the integration is approximately t_c. Combining equation (2.22) with the polytropic relation for $p_{b,col}$ yields

$$\frac{V_{col}}{V_o} \sim \left(\frac{\Delta p}{p_{eq}}\right)^{-3/(3k-1)} M^{3/2(3k-1)}, \tag{2.23}$$

which implies that the bubble volume would solely depend on the driving pressure ratio and effective Mach number because they uniquely determine the solution of the general KH equation (2.3) (see section 2.2.1). In the incompressible limit, the bubble volume at collapse achieves a power-law scaling with respect to driving pressure ratio, as shown in figure 2.9(a). At high pressure ratios in the incompressible case, most of the initial potential energy is concentrated to the bubble as an internal energy with no energy losses, so equation (2.13) can be expressed as $p_\infty V_o \approx p_{b,col}V_{col}/(k-1)$, which can be simplified with the polytropic relation of $p_{b,col}$:

$$\frac{V_{col}}{V_o} \approx (k-1)^{-1/(k-1)} \left(\frac{\Delta p}{p_{eq}}\right)^{-1/(k-1)}. \tag{2.24}$$

For a given k, the bubble volume scales with driving pressure ratio, which uniquely determines the solution of the RP equation (see section 2.2.1).

Using the scaling relations (2.23) and (2.24) for the bubble volume at collapse, the internal energy of the bubble at collapse can be determined as follows. The internal energy of the bubble at collapse $E_{BIE,col}$ normalized by the initial total energy can be approximated by

$$\frac{E_{BIE,col}}{E_{TE,o}} \approx \frac{1}{p_\infty V_o}\frac{p_{b,col}V_{col}}{k-1} \sim \left(\frac{\Delta p}{p_{eq}}\right)^{-\frac{2}{3k-1}} M^{-\frac{3(k-1)}{2(3k-1)}}, \tag{2.25}$$

for the compressible case, and

$$\frac{E_{BIE,col}}{E_{TE,o}} \approx \frac{1}{p_\infty V_o}\frac{p_{b,col}V_{col}}{k-1} \approx 1, \tag{2.26}$$

for the incompressible limit. At small pressure ratios, only some fraction of the potential energy of liquid is transferred to the bubble. As the driving pressure ratio is increased, the bubble internal energy at collapse tends to unity in the incompressible case, while in the compressible case energy losses due to acoustic radiation tend to unity.

The internal energy of the bubble at collapse normalized by initial internal energy is $E_{BIE,col}/E_{BIE,o} = (V_{col}/V_o)^{1-k}$. Using equations (2.23) and (2.24), we obtain the relation:

$$\frac{E_{BIE,col}}{E_{BIE,o}} \sim \left(\frac{\Delta p}{p_{eq}}\right)^{-3(1-k)/(3k-1)} M^{3(1-k)/2(3k-1)}, \tag{2.27}$$

for the compressible case, and

$$\frac{E_{BIE,col}}{E_{BIE,o}} \approx (k-1)\left(\frac{\Delta p}{p_{eq}}\right), \tag{2.28}$$

for the incompressible case. As illustrated in figure 2.9, the scaling relations (2.23)–(2.28) correctly describe the behavior of the energy and the bubble volume, thus confirming that the bubble volume and internal energy at collapse are determined by the initial conditions, i.e., driving pressure ratio and effective Mach number.

2.3.4 Shock pressure after collapse

At the instant of collapse, the internal energy is confined to the bubble volume, whose volume is finite, albeit small. In the incompressible limit, most of the potential energy is converted to internal energy of the bubble at collapse, while in the compressible case a significant fraction is lost due to acoustic radiation in the compressible case. For an inertially dominated collapse, the rapid compression of the gas gives rise to a large build-up in bubble pressure until the instant of collapse. At collapse, the pressure decreases rapidly and monotonically to ambient pressure in radial direction from the center of the bubble, such that the bubble rebound after collapse corresponds to a spherical Riemann problem (Zel'dovich, 2002). The bubble internal energy is then released as an explosion, including the emission of a shock. This explosion process cannot be accurately represented by potential flow, and by contrast to the Taylor–Sedov problem (Zel'dovich, 2002), the explosion energy is initially distributed over a finite volume and the surrounding medium has non-negligible inertia, such that classical analysis no longer holds.

Assuming conservation of the characteristics propagating outward from a spherical surface, Kirkwood & Bethe (1942) developed a theory to approximate the peak pressure of a spherical shock propagating outward p_m: $p_m \sim (R/r) \,/\, [\log(r/R)]^{1/2}$ for $r \gg R$, where r is the radial location of the shock front, and R is the radius of sphere at the instant of shock emission. For simplicity, p_m can be expressed as a similitude relation: $p_m \approx c_0(R/r)^{1+\alpha}$, where c_0 and α are material-dependent constants, and $\alpha = 0.13$ describes the logarithmic part of formula by Kirkwood and Bethe sufficiently and shows the best-fit to experimental data for TNT (Cole, 1948; Arons, 1954; Geers & Hunter, 2002; Hunter & Geers, 2004). Making the analogy between underwater explosions and bubble rebound, we apply this similitude relation to estimate the pressure of a shock produced in the spherical bubble collapse. Thus, as a model of the peak pressure of the shock (Supponen *et al.*, 2017), an empirical relation can be formulated as

$$p_m \sim p_{b,col}\left(\frac{R_{col}}{r}\right)^{1+\alpha} = p_{b,col}\left(\frac{R_{col}}{R_o}\right)^{1+\alpha}\left(\frac{R_o}{r}\right)^{1+\alpha}, \tag{2.29}$$

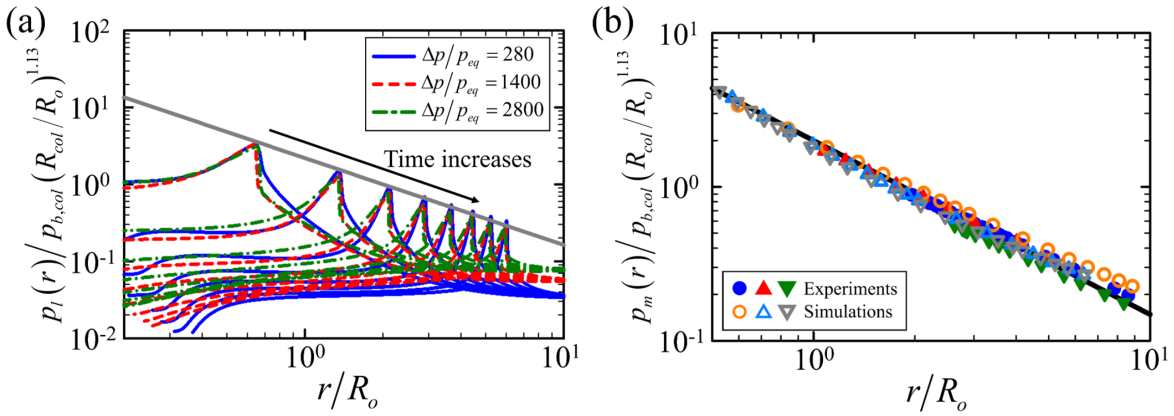

Figure 2.10: (a) Normalized pressure profile of the radiated shock wave as a function of distance at different times for $\Delta p/p_{eq} = 280, 1400, 2800$. (b) Normalized peak pressure of the shock produced at collapse as a function of radial distance. Pressures are normalized according to the scaling of equation (2.29); solid circles: Vogel *et al.* (1989); solid upward triangles: Lauterborn & Kurz (2010); solid downward triangles: Isselin *et al.* (1998); hollow circles: $\Delta p/p_{eq} = 280$; hollow upward triangles: $\Delta p/p_{eq} = 1400$; hollow downward triangles: $\Delta p/p_{eq} = 2800$; solid line: slope -1.13.

where $r \gg R_{col}$, such that the position $r = R_{col}$ at which the shock is released has no effect on p_m.

The liquid pressure profile and the peak pressure of shock shown in figure 2.10 confirms the relation (2.29). The time history of normalized pressure profiles of the emitted shock from direct simulations (Johnsen & Colonius, 2009; Beig *et al.*, 2018) at different pressure ratios manifests the peak pressure obeying the relation (2.29). However, there are some discrepancies in the tail of the shock pressure profile where the liquid flow velocity is significant compared to the local speed of sound and interferes with the shock propagation. In addition, rarefaction waves produced at collapse propagate toward the bubble center, reflect at the center, reach to the shock front, and may affect the tail of the shocks and their strength. As introduced in figure 2.10(b), the peak pressure of the shock observed in spherical bubble experiments (Vogel *et al.*, 1989; Lauterborn & Kurz, 2010; Isselin *et al.*, 1998) and direct simulations (Johnsen & Colonius, 2009; Beig *et al.*, 2018) collapse onto the expression given by equation (2.29), particularly at small distances. For $r/R_o \sim O(10)$, simulation results show discrepancies from the scaling relation because the shock has become so weak that it propagates as an acoustic wave with peak pressure decaying as $1/r$. Nevertheless, the relation (2.29) is a simple model for the shock that can be applied to estimate the shock pressure

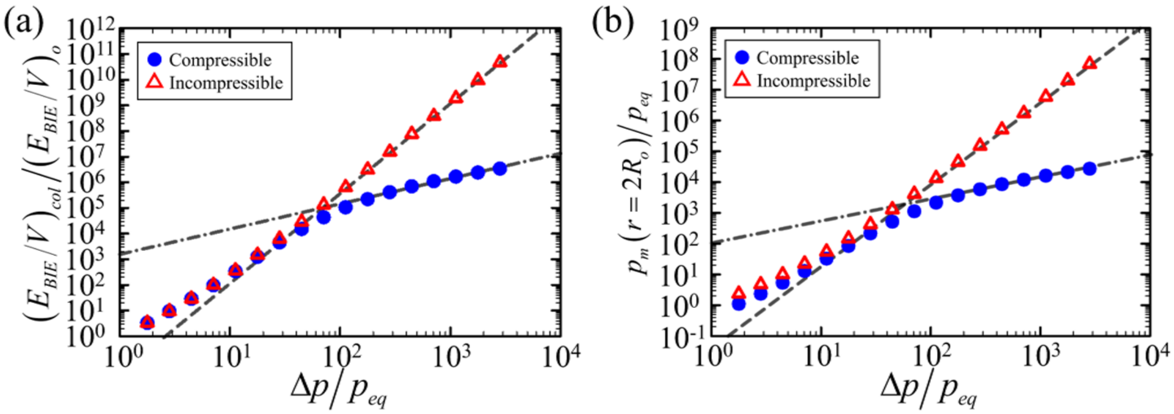

Figure 2.11: (a) Bubble energy density and (b) peak liquid pressure in the compressible (solid circles) and incompressible (open triangles) cases at $r/R_o = 2$ as a function of driving pressure ratio; dashed line: (a) equation (2.31), (b) equation (2.34); dash-dotted line: (a) equation (2.30), (b) equation (2.32).

at some distance from the bubble.

A quantitative measure of energy entrapped in the bubble is the energy density E_{BIE}/V, i.e., the bubble internal energy divided by bubble volume, normalized by the initial energy density (Ramsey & P., 2013). As shown in figure 2.11(a), the energy density of bubble increases as the driving pressure ratios is raised. The liquid compressibility significantly reduces the energy density at collapse, compared to the incompressible limit. As integrating the relations (2.23)–(2.25), we approximate the bubble energy density:

$$\frac{(E_{BIE}/V)_{col}}{(E_{BIE}/V)_o} \sim \left(\frac{\Delta p}{p_{eq}}\right)^{-3k/(3k-1)} M^{3k/2(3k-1)}, \tag{2.30}$$

for the compressible case, and

$$\frac{(E_{BIE}/V)_{col}}{(E_{BIE}/V)_o} \approx (k-1)^{-k/(k-1)} \left(\frac{\Delta p}{p_{eq}}\right)^{-k/(k-1)}. \tag{2.31}$$

for the incompressible limit. Those relations show good agreement with the simulations in figure 2.11(a).

The peak pressure of the shock produced at collapse is directly explained by the input parameters (i.e., driving pressure ratio and effective Mach number) because they are linked by the scaling relations for the bubble volume and energy [equations (2.23)–(2.26)]. Combining equations (2.23) and (2.29), the peak pressure of the shock can be related to the driving pressure ratio and effective Mach number:

$$\frac{p_m}{p_{eq}} \sim \left(\frac{\Delta p}{p_{eq}}\right)^{\frac{3k-(1+\alpha)}{3k-1}} M^{-\frac{3k-(1+\alpha)}{2(3k-1)}} \left(\frac{R_o}{r}\right)^{1+\alpha}. \tag{2.32}$$

In the incompressible limit, the maximum liquid pressure at collapse is approximated as

$$p_l(r) = p_\infty + (p_{b,col} - p_\infty)\frac{R_{col}}{r} - \frac{\rho_l}{2}\left(\frac{R^4\dot{R}^2}{r^4}\right) \approx p_{b,col}\left(\frac{R_{col}}{R_o}\right)\left(\frac{R_o}{r}\right), \tag{2.33}$$

which is equivalent to equation (2.29) with $\alpha = 0$ and can be expressed:

$$\frac{p_l}{p_{eq}} \approx (k-1)^{\frac{3k-1}{3(k-1)}} \left(\frac{\Delta p}{p_{eq}}\right)^{\frac{3k-1}{3(k-1)}} \left(\frac{R_o}{r}\right). \tag{2.34}$$

Figure 2.11(b) shows the peak pressure at $r = 2R_o$ for the compressible and incompressible cases. This distance is chosen such that the shock front is neither too close to the bubble, so that the incoming liquid flow does not interfere with the shock propagation, or too far, in which case the shock propagates as an acoustic wave. In the compressible case, the peak pressure corresponds to that of the shock. However, in the incompressible case, the pressure is determined from equation (2.34) (Brennen, 1995) and does not actually correspond to that of a shock. An increase in the driving pressure ratio leads to a larger energy density (or gas pressure) inside the bubble, and thus a stronger shock. The good agreement between the simulations and the relations (2.32) and (2.34) for the compressible and incompressible case confirms that by ignoring acoustic energy losses the incompressible model vastly overpredicts the shock pressure. The current model is thus capable of determining the amplitude of shocks produced by inertially collapsing bubbles given the initial conditions (driving pressure ratios and effective Mach number).

2.4 Discussion

2.4.1 Application of energy budget framework to experimental data

Our framework can readily be applied to experimental data for analysis. Here, we consider the single-bubble laser-generated experiments of Tinguely *et al.* (2012), which produced a highly spherical bubble under microgravity conditions. In their experiments, the bubble with a maximum size of 2 to 5.6mm were generated at three distinct liquid pressures ($p_\infty = 10, 30, 80$ kPa). Their analysis was focused on the bubble collapse, which is driven by the difference between liquid pressures and the reduced gas pressures, and the subsequent rebound. We examine the time evolution of different energy partitions to understand overall energy transport in these experiments, quantify the losses, and evaluate the shock produced upon collapse. Figure 2.12 shows the time history of the bubble radius and energy budget corresponding to the experiments in Tinguely *et al.* (2012). One of the bubble radius–time curves for each initial gas pressure ($p_o = 6, 8, 10$ Pa) is chosen from data sets, and the KK equation [equation (2.3) with $\lambda = 0$] is used for the simulation because thermal and viscous effects are negligible for milimeter-size bubbles and gas diffusion is much slower than the first collapse and rebound. The simulation results show excellent agreement with the experimental data throughout the collapse and rebound. Overall, the potential energy at maximum radius is transferred to kinetic energy of the bubble. Compressible losses and bubble internal energy undergo significant changes starting just before collapse. Again, it is confirmed that our framework [equation (2.15)] assures the constant total energy with an integration error in $O(10^{-7})$, while the deviations in the total energy are ranging from 0.3 to 0.8 for Wang's approach [equation (2.16)] and from 0.3 to 0.5 for Holzfuss's approach [equation (2.18)].

Figure 2.13 quantifies the bubble volume and bubble internal energy at collapse, and energy losses due to acoustic radiation through the collapse, and relates these quantities to the predicted shock strength. For the lowest gas pressure, the bubble has the smallest volume, and the greatest fraction of the total energy is lost through acoustic radiation, as expected since the resulting pres-

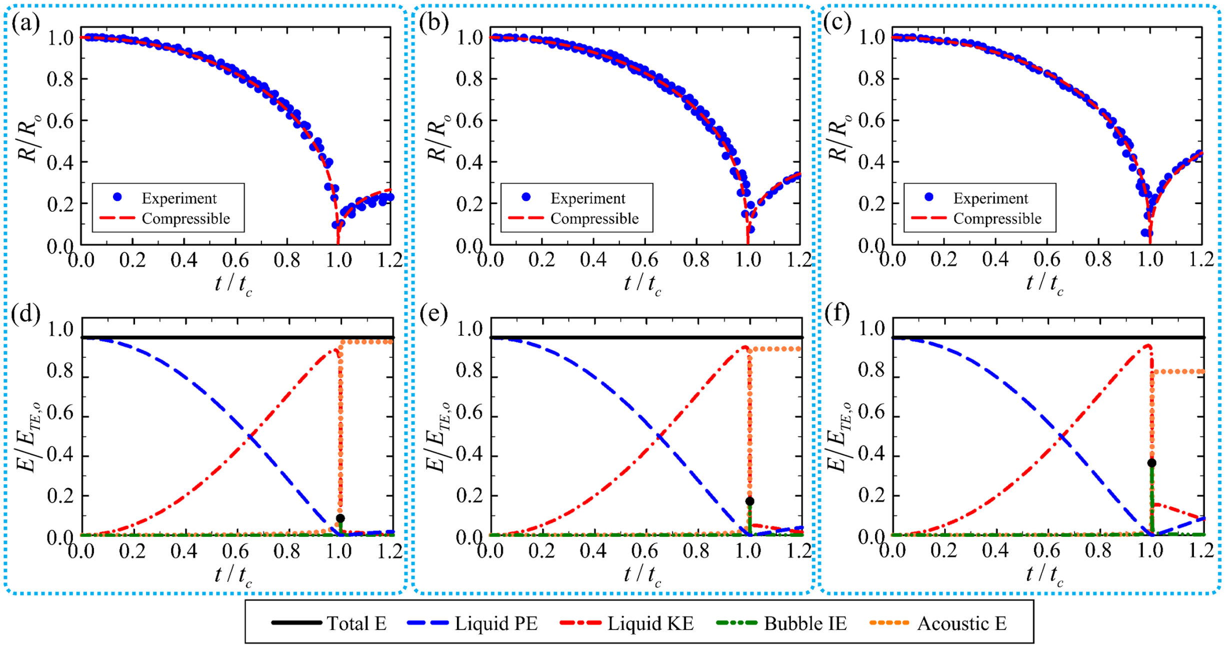

Figure 2.12: Time evolution of the bubble radius and energy budgets evaluated using experimental data in Tinguely *et al.* (2012). The initial gas pressure p_o =6 Pa, and p_∞ =(a,d) 80, (b,e) 30, and (c,f) 10 kPa. Dots in (d,e,f): bubble internal energy at collapse.

sure ratio is the highest of the three cases such that higher velocities are achieved at collapse. It follows that the smallest portion of the total energy is concentrated to the bubble for the experiments with the lowest gas pressure. As the gas pressure is increased, the driving pressure ratio is smaller, leading to larger bubble volume, lower bubble wall velocities, smaller losses of the total energy due to acoustic radiation, and therefore larger energy concentration of the total energy to the bubble. A resulting lower gas pressure at collapse leads to smaller peak pressure of the shock produced at collapse. It further follows that the rebounds are larger as the gas pressure is increased, since less energy is lost by and more energy is available to the bubble, compared to those cases with lower initial gas pressure. The observed behavior is consistent with that discussed in section 2.3.3 and section 2.3.4, including the scalings with driving pressure ratio.

In application of our framework to experimental data, several uncertainties should be considered. First, the initial gas pressure inside a bubble must be estimated for the experimental data. In Tinguely *et al.* (2012), the liquid pressure and temperature are readily controlled in the experiment, and the maximum bubble radius can be measured from optical images. However, the driving pres-

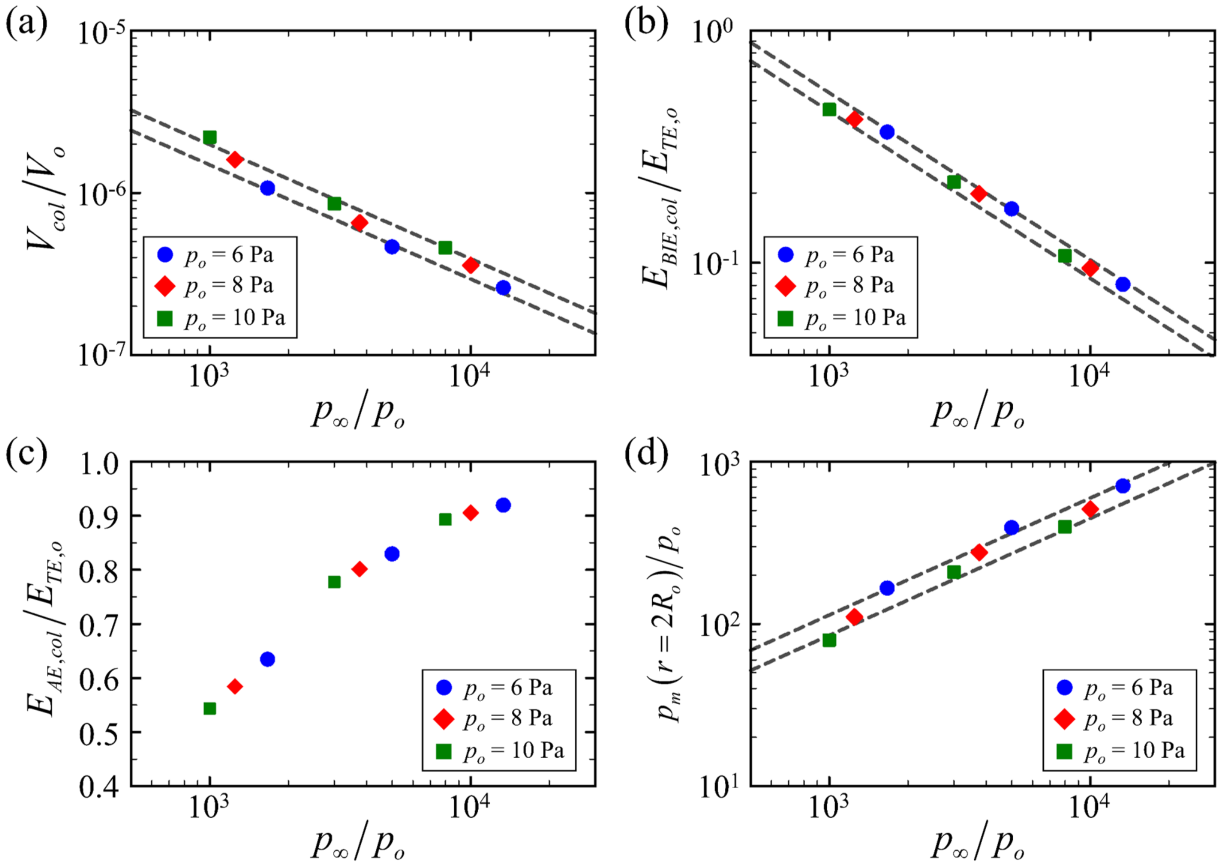

Figure 2.13: (a) Bubble volume and (b) bubble internal energy at collapse, (c) energy losses due to acoustic radiation through the collapse, and (d) shock peak pressure at $r = 2R_o$ for $p_o = 6$, 8, and 10 Pa, and $p_\infty = 10$, 30, and 80 kPa. Dashed line: (a) equation (2.23), (b) equation (2.25), and (d) equation (2.32).

sure of the gas inside a bubble is not directly measurable, leading to uncertainties in the driving pressures, which, as we showed here, determines the bubble dynamics and energy transport in the system. In Tinguely *et al.* (2012), the initial gas pressure was estimated by fitting simple models (RP, KK equation) to the experimental data. In another related study, Estrada *et al.* (2018) deduced the initial gas pressure by invoking mechanical equilibrium as $t \to \infty$. Assuming that the gas mass remains constant in time and that the gas temperature is the same at $t = 0$ and $t \to \infty$, Boyle's law can be used to obtain the initial gas pressure. Another uncertainty is that thermal and viscous effects on the gas and liquid may be important for micron-size bubbles, for which the gas Fourier number $\alpha_{th} t_c / R_o^2$ and Reynolds number $\rho_l U R_o / \mu_l$ are large. Here, α_{th} is the thermal diffusivity of the gas. In Tinguely *et al.* (2012), the laser pulse energy varying from 55 to 230 mJ results in maximum bubble radii from 2 to 5.6 mm, so these effects are negligible. However, for lower laser pulse energy and thus smaller bubble, energy losses due to thermal conduction and viscous dissipation may become important and should be accounted for in the energy budget analysis.

2.4.2 Effects of compressibility on the bubble collapse

As illustrated in figure 2.9, we observe two regimes in the bubble dynamics, energy transport, and subsequent shock emission: up to a certain pressure ratio (~ 100), the bubble dynamics described by the incompressible and compressible models are indistinguishable from each other; beyond that pressure ratio, the compressible solution departs from the incompressible limit. At low driving pressure ratios, the bubble oscillations are linear. As the driving pressure ratio is raised, nonlinear inertially dominated effects become increasingly important, though compressible is not (yet) significant. As the driving pressure ratio is further increased, effective Mach numbers are no longer negligible; compressible effects (acoustic radiation) significantly affect the bubble dynamics, resulting in significant damping of oscillations.

A more quantitative description of these different regimes can be provided. In the linear regime, $R \approx R_{eq}(1 + x)$, where R_{eq} is the equilibrium radius, $R_{eq} = R_o$, and x is the small perturbation, thus yielding the linearized RP equation $\ddot{x} + \omega_{eq}^2 x = (p_{eq} - p_\infty)/\rho_l R_o^2$, where $\omega_{eq}^2 = 3kp_{eq}/\rho_l R_{eq}^2$ (Brennen, 1995; Leighton, 2012). Although $|x| \ll 1$, we also approximates a criterion that roughly classifies transition from linear to inertial regime by $1 + x > 0$, which produces $\Delta p/p_{eq} < 1.5k \approx 2.1$ for air. Thus, the bubble collapse is (i) linear as long as $\Delta p/p_{eq} \ll 2.1$, (ii) inertial at $\Delta p/p_{eq} \gg 2.1$, and are (iii) transitioned from linear to inertial collapse around $\Delta p/p_{eq} \approx 2.1$.

To estimate the driving pressure ratio at which the compressible case becomes distinguished from the incompressible limit as the pressure ratio is increased, we use the modified Herring equation (Vokurka, 1986), in which only the bubble pressure term is retained, as it can be manipulated in forms advantageous for the present analysis. The normalized volume of the bubble at collapse

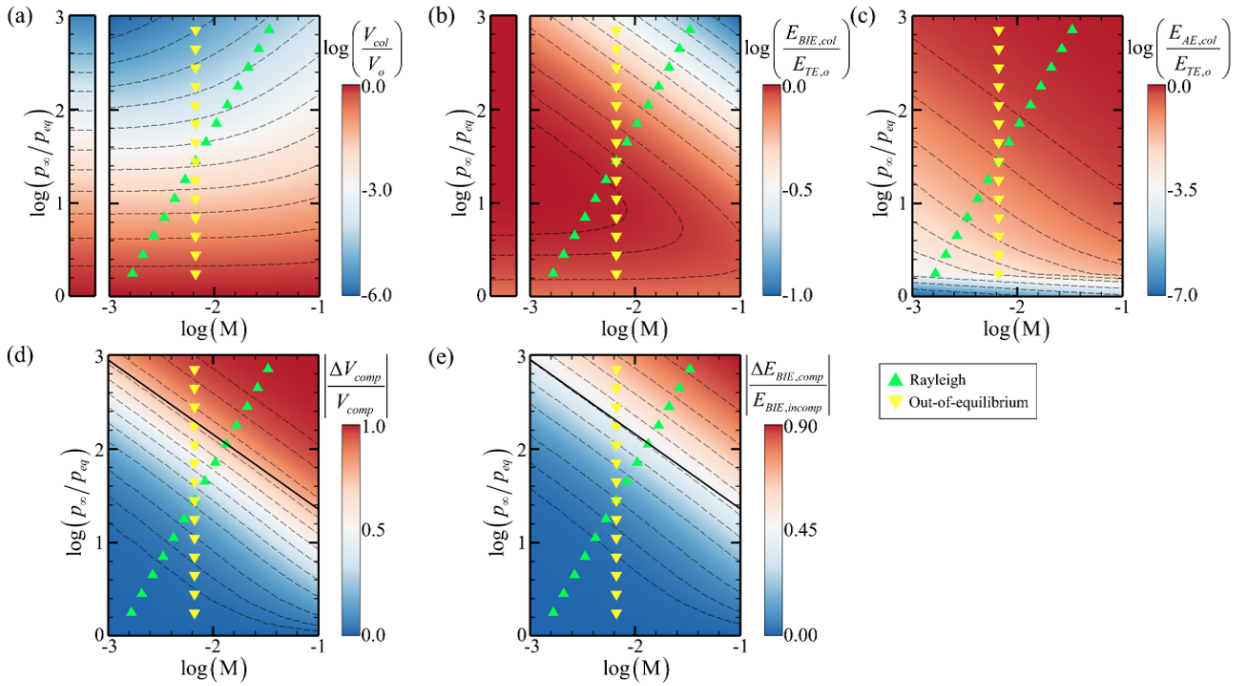

Figure 2.14: Contour map of the logarithmic value of the (a) bubble volume and (b) bubble internal energy at collapse, and (c) energy losses due to acoustic radiation until collapse for the compressible case, and of the absolute value of difference in the (d) bubble volume $|\Delta V_{comp}/V_{comp}|$ and (e) bubble internal energy $|\Delta E_{BIE,comp}/E_{BIE,incomp}|$ between the compressible and incompressible cases as a function of driving pressure ratio and effective Mach number. The left column map in (a) and (b) corresponds to the incompressible limit. The differences in (d) and (e) are non-dimensionalized by the larger of the two values; Solid line: equation (2.37); Dashed line: isoline.

can be expressed purely in terms of non-dimensional quantities describing the problem:

$$\frac{V_{col}}{V_o} \approx \eta_V \left(\frac{\Delta p}{p_{eq}}\right)^{-2/(2k-1)} M^{2/(2k-1)}, \tag{2.35}$$

where $\eta_V = k^{-1/(k-1)}(6k^2)^{1/(2k-1)}$. A full derivation is provided in Appendix A. Equating this relation and the scaling relation for the bubble volume in the incompressible limit [equation (2.24)] yields the condition at which the compressibility effects become distinguishable as the driving pressure ratio is increased:

$$\frac{\Delta p}{p_{eq}} \approx \eta_o M^{-2(k-1)}, \tag{2.36}$$

where $\eta_o = [k/(k-1)]^{2k-1}(6k^2)^{-(k-1)}$. In figures 2.9 and 2.11, this regime transition occurs at $\Delta p/p_{eq} \approx 111$; beyond this ratio, the bubble falls within the regime where the compressibility plays a role. This transition beyond which the compressible solution departs from the incompressible behavior is naturally not abrupt, but rather gradual as the driving pressure ratio is increased. Nevertheless, equation (2.36) provides an estimate.

The dependence of the key collapse quantities on both the driving pressure ratio and the effective Mach number can be determined based on the KK solution. Figure 2.14 shows maps of X vs. M and $\Delta p/p_{eq}$ on logarithmic scales; the incompressible limit is added for the bubble volume and internal energy at collapse. The driving pressure ratios and effective Mach numbers considered for the Rayleigh and out-of-equilibrium collapse are shown in symbols. A discussion for the out-of-equilibrium collapse will be introduced in the next section. For M → 0, the compressible solution tend to the incompressilbe limit, as expected. For a given $\Delta p/p_{eq}$, an increasing M leads to an increase in energy losses due to acoustic radiation and thus a reduction in bubble compression (larger minimum volume) and in energy concentration (smaller bubble internal energy). For a given M, raising $\Delta p/p_{eq}$ leads to increased bubble compression (smaller minimum volume); the bubble internal energy also increased due to large energy transfer from the potential energy, but eventually reaches a local maximum as the energy losses due to acoustic radiation become important.

To better understand the role of the liquid compressibility, we calculate the absolute value of difference in the bubble volume and energy between the compressible cases and incompressible limits, $\Delta V_{comp} = V_{comp} - V_{incomp}$ or $\Delta E_{comp} = E_{comp} - E_{incomp}$, which is non-dimensionalized by the larger of the two values. As $\Delta p/p_{eq}$ or M are increased, this normalized difference becomes larger, thus illustrating the increasingly important effect of liquid compressibility. Furthermore, equations (2.35) and (2.24) can be used to establish the approximate dependence of these changes on the parameters governing the problem:

$$\frac{V_{incomp}}{V_{comp}} = 1 - \frac{\Delta V_{comp}}{V_{comp}} \approx \left(\frac{1}{\eta_o}\frac{\Delta p}{p_{eq}}\right)^{-1/(2k-1)(k-1)} M^{-2/(2k-1)}, \tag{2.37}$$

whose slopes show good agreement with those of isolines depicted in figures 2.14(d) and 2.14(e).

2.4.3 Dependence of energy concentration and release on types of collapse problems

The classical Rayleigh collapse problem where the liquid is overpressurized has been primarily examined to understand the cavitation bubble dynamics (Besant, 1948; Rayleigh, 1917; Noltingk & Neppiras, 1950; Brennen, 1995; Johnsen & Colonius, 2009; Barajas & Johnsen, 2017; Beig *et al.*, 2018). However, initial conditions driving the bubble collapse may change the bubble dynamics, energy concentration, and shock emission at collapse. Under the standard ambient pressure p_∞, a bubble with larger radius than the equilibrium bubble radius has lower gas pressure p_o than the equilibrium gas pressure p_{eq}, such that the initial state is out of equilibrium (Flynn, 1975a,b; Leighton, 2012; Gaudron *et al.*, 2015; Barajas & Johnsen, 2017; Estrada *et al.*, 2018). In this out-of-equilibrium collapse, same as the Rayleigh collapse, pressure difference between the surroundings and the gas drives the bubble collapse from maximum to minimum size. During the collapse, some fraction of the initial potential energy of liquid is concentrated to the bubble during the collapse with energy losses due to acoustic radiation, while the magnitudes of concentrated energy and the peak pressures of released shock show large discrepancies between those two collapse problems. The out-of-equilibrium collapse is a simpler case of an acoustically-oscillated gas bubble primarily used in bio-medical applications (e.g., histotripsy for tissue ablation), where the driving pressure ratio is $\Delta p/p_o$ where $p_\infty = 0.1$ MPa and $p_o < p_{eq}$.

Figure 2.15 shows the bubble dynamics, energy, energy density, shock pressure, and effective Mach number in the Rayleigh and out-of-equilibrium collapse for a bubble in a compressible liquid. In both cases, the energy losses due to acoustic radiation increase with increasing pressure ratio as the bubble wall velocity also increases [equation (2.15)], such that the bubble has a smaller volume at collapse and less fraction of the total energy is concentrated to the bubble. It follows that the peak shock pressure $2R_o$ away from the bubble is larger at high pressure ratios due to larger bubble energy density.

Although both collapse problems show similar behavior for change in the driving pressure

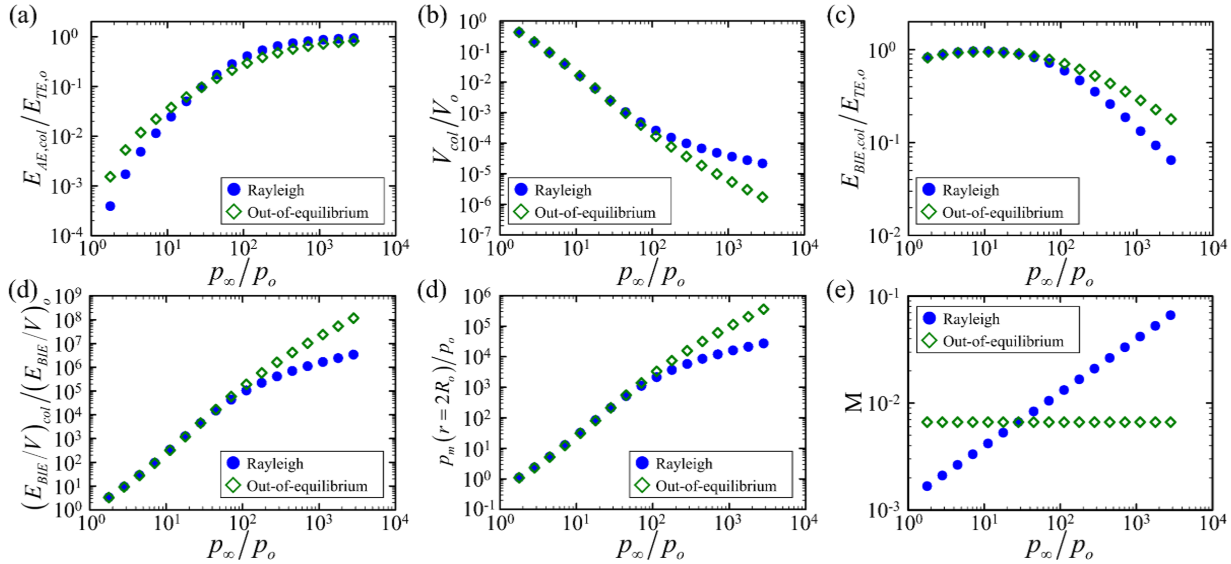

Figure 2.15: (a) Bubble volume and (b) bubble internal energy at collapse, (c) energy losses due to acoustic radiation through the collapse, (d) bubble energy density at collapse, (e) maximum peak pressure of the shock at $r/R_o = 2$, and (f) effective Mach number as a function of driving pressure ratio for the Rayleigh and out-of-equilibrium collapse.

ratios, there are some discrepancies between them even for the same pressure ratio, which are described by the dependence of effective Mach number on the driving pressure ratio. As the driving pressure ratio is increased, once it crosses over at $\Delta p/p_o \sim 27$, the effective Mach number in the out-of-equilibrium collapse becomes smaller than that in the Rayleigh collapse, such that compressibility effects become less important and a smaller fraction of total energy is lost in the out-of-equilibrium collapse. Therefore, at $\Delta p/p_o > 27$, the bubble in the out-of-equilibrium collapse case is more compressed, i.e., has a smaller minimum volume, with larger energy concentration to the bubble, leading to larger bubble energy density and higher peak shock pressure $2R_o$ away from the bubble. Up to driving pressure ratios on the order of 10s where the energy losses is smaller than 10%, the discrepancies between two collapse cases are negligible due to small compressibility effects.

2.5 Conclusion

In summary, we propose a theoretical approach to accurately represent energy transport, including direct calculations of compressible losses during the oscillation of a spherical bubble in a weakly compressible liquid described by the general Keller–Herring equation. This approach is used to build an energy budget framework identifying energy modes in the liquid–bubble system and for elucidation of energy transport between these modes. As the bubble begins to collapse, the potential energy in the liquid is primarily transferred to kinetic energy of the liquid; in the final stage of collapse, energy losses due to acoustic radiation and bubble internal energy become significant. In the early stage of the collapse, the liquid primarily loses its kinetic energy due to acoustic radiation, and these losses lead to less energy concentration to the bubble in the final stage of the collapse.

We quantitatively demonstrate that the energy concentration during the collapse obeys one of two scenarios: up to the driving pressure ratio of 112, most of the initial energy is concentrated into the bubble, whereas beyond that pressure ratio, a significant fraction of the initial energy is lost via acoustic radiation, thus reducing the efficiency of the energy concentration process. Liquid compressibility also reduces the energy density and thus the strength of the shock emitted upon collapse. Overall, as the driving pressure ratio is increased, the liquid has a larger potential energy initially, such that a larger energy is concentrated to a smaller bubble confinement at collapse, thus increasing the bubble energy density and demonstrating a stronger shock is released. Using our energy budget framework, we develop scaling relations for the bubble volume, energy concentration, bubble energy density, and shock emission at collapse depending on the parameters governing the problem, i.e., the driving pressure ratio and effective Mach number. These scaling relations are employed to identify the driving pressure ratios at which the compressibility effects become important. Finally, we apply our framework to experimental data for validation and analysis.

Additional effects (e.g., thermal conduction, viscous dissipation, surface tension) are expected to affect the energy transfer in other regimes. In the future, we plan to incorporate these effects into our model. Furthermore, the present results will form the basis for better understanding energy concentration and shock emission in non-spherical bubble collapse.

CHAPTER 3

Energy Transfer during the Growth and Collapse of a Cavitation Bubble in an Acoustic Field

Acoustic cavitation has been used for a variety of applications including therapeutic ultrasound procedures (e.g., lithotripsy, histotripsy) and ultrasonic cleaning. When a gas nucleus is exposed to strong transient rarefaction waves, it undergoes an explosive growth and violent collapse, leading to the generation of shock waves and large deformation of the surrounding material, which may lead to local damage. However, the relation between input parameters (e.g., external waveform, nucleus size) and outputs (e.g., maximum bubble radius and energy concentration at collapse), which is necessary to predict damage, is not known due to the large parameter space and complex physics. In this study, we develop a framework to understand how energy is transferred from the wave to the medium. Using this framework, we obtain scaling relations describing bubble expansion during the growth and energy concentration at collapse based on the waveform properties. These relations will help to better understand cavitation-induced damage and develop strategies to control cavitation bubble dynamics.

3.1 Introduction

Under the action of ultrasound waves, a pre-existing gas nucleus grows and collapses when it is exposed to negative pressure regions in the ultrasound waves. In the presence of the gas nucleus, the interactions between the ultrasound waves and the nucleus lead to a different type of energy transfer from the waves (energy source) to the medium. When the amplitude of the waves is sufficiently large, the bubble undergoes explosive growth, followed by rapid compression, called inertial collapse. During inertial collapse, the input energy is concentrated into the bubble, such that high pressure and temperature build up inside the bubble at collapse. As the bubble rebounds, some of the bubble energy is released via a shock wave. In addition to the shock emission, large-amplitude bubble oscillations also lead to local changes in the surrounding medium (e.g., large deformations).

The outcomes of such oscillations may lead to damage in the surrounding medium; this damage is observed and even used in a variety of biomedical applications. The damage produced by inertial cavitation is used to homogenize soft tissue into acellular debris during histotripsy treatment (Xu *et al.*, 2004; Parsons *et al.*, 2006; Khokhlova *et al.*, 2015; Bader *et al.*, 2019). Large deformations and shock waves observed in inertial collapse may be responsible for disrupting the blood-brain barrier (BBB), enabling targeted drug delivery to the brain in the BBB opening technique (McDannold *et al.*, 2006; Tung *et al.*, 2010). On the other hand, the damage produced by cavitation bubbles causes undesirable bioeffects (e.g., capillary ruptures in tissue) in contrast-enhanced ultrasound treatment, in which lipid-coated microbubbles are injected intravenously to enhance the contrast in imaging (Patterson *et al.*, 2012; Versluis *et al.*, 2020). However, the relationship between waveform properties and cavitation-induced damage is unclear. Thus, further investigation of dependence of bubble response and key shock properties on initial conditions (i.e., waveform properties and initial bubble size) is needed to better utilize bubbles and control bioeffects for the safety and efficacy of these applications.

For freely-oscillating bubbles whose growth is initially driven by an impulse or pulsed ultrasound waveform, the first of many oscillations is typically responsible for the results desirable or undesirable for the applications. The amplitude of subsequent oscillations rapidly attenuates due to energy transfer by compressibility, thermal conduction, and viscosity. In the present study, we focus on the first oscillation, which can be divided into two sequential components: bubble growth (the initial equilibrium state to the maximum bubble radius) and bubble collapse (the maximum bubble radius to the minimum bubble radius at collapse). In chapter 2, we develop a model for inertial collapse to predict bubble radius and energy at collapse using the parameters at maximum size:

$$\frac{R_{col}}{R_{max}} \sim \left(\frac{\Delta p}{p_{b,max}}\right)^{\frac{-1}{3k-1}} M^{\frac{1}{2(3k-1)}}, \qquad \frac{E_{BIE,col}}{E_{TE,max}} \sim \left(\frac{\Delta p}{p_{b,max}}\right)^{-\frac{2}{3k-1}} M^{-\frac{3(k-1)}{2(3k-1)}}, \tag{3.1}$$

where R_{col} is the bubble radius at collapse, R_{max} is the bubble radius at maximum size, Δp is the driving pressure, $\Delta p = p_\infty - p_{b,max}$, p_∞ is the liquid pressure at far field, $p_{b,max}$ is the bubble pressure at maximum size, M is the effective Mach number, $M = \sqrt{\Delta p/\rho_l a_l^2}$, a_l is the speed of sound, $E_{BIE,col}$ is the energy of the bubble at collapse, $E_{TE,max}$ is the total energy at maximum size. Then, an empirical relation for peak pressure of the shock p_m is

$$\frac{p_m}{p_{b,max}} \sim \left(\frac{\Delta p}{p_{b,max}}\right)^{\frac{3k-1.13}{3k-1}} M^{-\frac{3k-(1+\alpha)}{2(3k-1)}} \left(\frac{R_{max}}{r}\right)^{1.13}. \tag{3.2}$$

Although helpful for assessing energy concentration during collapse, these relations depend on the maximum radius, which is not known a priori. The goal of this work is to determine the dependence of the quantities at collapse on the initial conditions, namely the initial nucleus forcing (waveform properties).

In the context of ultrasound-induced cavitation, several models have been developed to predict the maximum bubble radius using initial conditions. By examining energy transfer during bubble growth in water, Apfel (1981) derived a model for predicting R_{max} based on R_{eq} and the continuous sinusoidal waveform, by assuming that the change in the potential energy between R_{eq} and R_{max} is the same as the maximum kinetic energy of the liquid. However, this model does not apply to freely-oscillating bubbles. Although Bader & Holland (2016) empirically obtained the relation for predicting the maximum bubble diameter after growth of the bubble in water for the purpose of histotripsy, the relation is only valid for the specific pulsed ultrasound waveform considered in their study.

The objective of this work is to determine the dependence of the maximum bubble radius on the input parameters (i.e., equilibrium bubble radius, and wave amplitude and period) for a bubble oscillating in water driven by a pulsed ultrasound waveform. For this purpose, we present a framework to decompose the energy of the liquid–bubble system into different modes and to track their evolution during bubble oscillations. The framework introduced in section 2 is extended to also quantify heat energy into liquid via thermal conduction at the bubble wall, as well as energy transport via viscous and surface tension effects. This chapter is organized as follows. First, the dynamic equations describing the bubble dynamics and energy transport are introduced in section 3.2. This framework is used to track the time evolution of each energy mode and to understand the energy transfer during the bubble growth, thus enabling the development of a model predicting the maximum radius and energy at that time in section 3.3. In section 3.4, we apply this knowledge to histotripsy and different regimes. Concluding remarks close the chapter in section 3.5.

3.2 Energy transport in bubble oscillations driven by an acoustic field

3.2.1 Problem description and modeling of gas bubble dynamics

Initially, a bubble filled with non-condensible gas at pressure p_{eq} is in mechanical and thermal equilibrium with its surroundings, such that

$$p_{eq} = p_\infty + 2S/R_{eq}, \tag{3.3}$$

where p_∞ is the far-field liquid pressure, S is the surface tension, and R_{eq} is the equilibrium radius. As illustrated in Fig. 3.1(a), acoustic waves from the far-field (Ω_∞) disrupt the equilibrium and cause the bubble (Ω_B) to oscillate. The interaction of the ultrasound with the bubble is a means by which energy is transferred from the wave to the medium as the bubble oscillates and eventually loses energy via a variety of mechanisms. We expect that the waveform and initial bubble radius determine bubble growth (i.e., maximum bubble radius R_{max}) and subsequent collapse (i.e., bubble radius at collapse R_{col}). For simplicity, a Gaussian pulse is considered because it is general

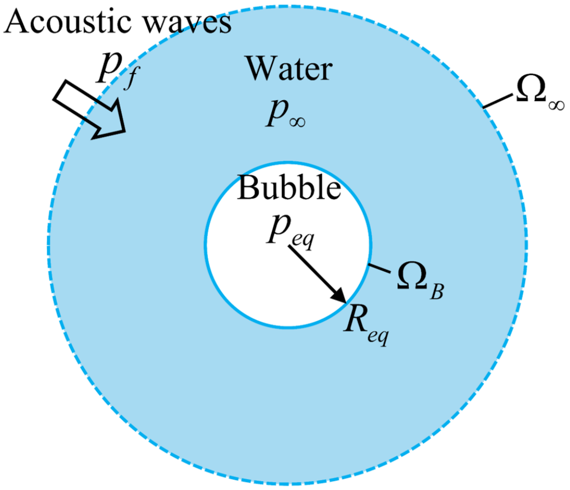

Figure 3.1: (a) Schematic of bubble oscillations in an acoustic wave field.

enough to represent ultrasound waves (Flynn, 1975b). The acoustic period τ corresponding to the Gaussian pulse is assumed as $\tau = 4\sigma$, within which over 95 % of the Gaussian pulse is contained. The frequency is $f = 1/\tau$. The bubble is assumed to maintain its spherical shape during oscillations, which is a reasonable assumption given that ultrasound wavelength is much larger than the equilibrium radius, i.e., $a_l\tau \gg R_{eq}$, where τ is the acoustic period.

The oscillations of a spherical bubble in an acoustic field can be described by the Keller–Miksis (KM) equation (Keller & Miksis, 1980):

$$R\ddot{R}\left(1-\frac{\dot{R}}{a_l}\right)+\frac{3}{2}\dot{R}^2\left(1-\frac{\dot{R}}{3a_l}\right)=\left[\frac{p_l-p_\infty-p_f}{\rho_l}\right]\left(1+\frac{\dot{R}}{a_l}\right)+R\left(\frac{\dot{p}_l-\dot{p}_f}{\rho_l a_l}\right), \tag{3.4}$$

where $p_f = -p_A\exp[-0.5((t-w_f)/\sigma)^2]$, p_A is the peak amplitude, w_f is the mean pressure, and σ is the standard deviation. As introduced in section 2.2.1, weak compressibility of medium is considered to first order in effective Mach number $M = U/a_l$ based on the characteristic velocity $U = \sqrt{\Delta p/\rho_l}$, where $\Delta p = p_{eq} + p_A - p_\infty$. At the bubble wall, normal components of the stresses are balanced, as described in Eq. (2.4).

During such bubble oscillations, heat conduction may lead to inhomogeneous temperature fields inside the bubble (Prosperetti, 1977, 1991). To account for such effects, we solve the energy equation inside the bubble,

$$\left(\frac{k}{k-1}\right)\frac{p_b}{T_b}\frac{\mathrm{d}T_b}{\mathrm{d}t} = \dot{p}_b + \frac{1}{r_{in}^2}\left(2r_{in}K_b\frac{\partial T_b}{\partial r_{in}} + r_{in}^2 K_b\frac{\partial^2 T_b}{\partial r_{in}^2}\right), \tag{3.5}$$

where $T_b(t, r)$ is the gas temperature inside the bubble, and k is the specific heat capacity ratio, t is the time, K_b is the gas thermal conductivity, and r_{in} is the radial coordinate inside the bubble. Mass diffusion is neglected because the corresponding time scales over which those processes affect the dynamics are far longer than those under consideration. To account for the dependence of the thermal conductivity of gas on the temperature $K_b(T_b) = AT_b + B$, where $A = 5.3 \times 10^{-5}\mathrm{W/mK^2}$, and $B = 1.17 \times 10^{-2}\mathrm{W/mK}$ are empirically determined coefficients (Prosperetti *et al.*, 1988), we change variables (Prosperetti *et al.*, 1988; Barajas & Johnsen, 2017):

$$\theta_b = \int_{T_{eq}}^{T} K_b(T')\mathrm{d}T', \tag{3.6}$$

and Eq. (3.5) becomes

$$\left(\frac{k}{k-1}\right)\frac{p_b}{K_b T_b}\frac{\mathrm{d}\theta_b}{\mathrm{d}t} = \dot{p}_b + \frac{1}{r_{in}^2}\left(2r_{in}\frac{\partial \theta_b}{\partial r_{in}} + r_{in}^2\frac{\partial^2 \theta_b}{\partial r_{in}^2}\right). \tag{3.7}$$

Combining this equation with the continuity equation for the gas inside the bubble, the velocity field inside the bubble $u_b(r_{in}, t)$ can be obtained:

$$u_b(r_{in}, t) = \frac{1}{kp_b}\left[-\frac{r_{in}}{3}\dot{p}_b + (k-1)\frac{\partial \theta_b}{\partial r_{in}}\right]. \tag{3.8}$$

Since the bubble wall velocity is much smaller than the gas speed of sound for the most part of the oscillation, the gas pressure can be assumed uniform (Prosperetti, 1977; Nigmatulin *et al.*, 1981; Prosperetti *et al.*, 1988; Prosperetti, 1991, 2017; Zhou & Prosperetti, 2020). At the bubble wall,

$u_b(r_{in} = R) = \dot{R}$, such that the gas pressure inside the bubble can be expressed:

$$\dot{p}_b = \frac{3}{R}\left[-kp_b\dot{R} + (k-1)K_b\frac{\partial T_b}{\partial r_{in}}\bigg|_w\right], \tag{3.9}$$

where the subscript w indicates the bubble wall. In liquid, we use the cold-water assumption $T_l = T_\infty$ because the thermal conductivity of liquid are much larger than those of gas. This assumption is verified in Appendix B.

Making use of R_{eq}, U, T_{eq}, and K_{eq}, Eqs. (3.4), (2.4) (3.7)–(3.9) can be rewritten in dimensionless form:

$$R^*\ddot{R}^*\left(1 - \dot{R}^*M\right) + \frac{3}{2}\dot{R}^{*2}\left(1 - \frac{\dot{R}^*}{3}M\right) = \left(p_l^* - p_\infty^* - p_f^*\right)\left(1 + \dot{R}^*M\right) + (\dot{p_l}^* - \dot{p_f}^*)R^*M, \tag{3.10}$$

$$p_b^* = p_l^* + \frac{4}{\mathrm{Re}_l}\frac{\dot{R}^*}{R^*} + \frac{2}{\mathrm{We}_l R^*} \tag{3.11}$$

$$\frac{\partial\theta_b^*}{\partial t^*} + \left(\frac{u^* - \dot{R}^*y}{R^*}\right)\frac{\partial\theta_b^*}{\partial y} = \dot{p}_b^*\left(\frac{k-1}{k}\right)\frac{K_b^*T_b^*}{p_b^*} + \frac{\mathrm{Fo}_b K_b^*}{R^{*2}}\left(\frac{2}{y}\frac{\partial\theta_b^*}{\partial y} + \frac{\partial^2\theta_b^*}{\partial y^2}\right), \tag{3.12}$$

$$u_b^* = -\frac{y}{3k}\left(\frac{R^*\dot{p}_b^*}{p_b^*}\right) + \frac{\mathrm{Fo}_b}{R^*T^*}\frac{\partial\theta_b^*}{\partial y}, \tag{3.13}$$

$$\dot{p}_b^* = \frac{3k}{R^*}\left[-p_b^*\dot{R}^* + \left(\frac{\mathrm{Fo}_b p_b^*}{R^*T_b^*}\right)\frac{\partial\theta_b^*}{\partial y}\bigg|_w\right], \tag{3.14}$$

where the Reynolds number is $\mathrm{Re}_l = \rho_l U R_{eq}/\mu_l$, the Weber number is $\mathrm{We}_l = \rho_l U^2 R_{eq}/S$, the thermal Fourier number is $\mathrm{Fo}_b = \alpha_b(R_{eq}/U)/R_{eq}^2$, α_b is the thermal diffusivity of gas, $p_f^* = -p_A^*\exp[-0.5((t^* - w_f^*)t_r^*)^2]$, where $t_r^* = R_{eq}/U\sigma$, and for simplicity in the spatial discretization, the radial coordinate is transformed as $y = r_{in}/R$, where $y \in [0, 1]$. A fifth-order Cash–Karp Runge–Kutta method is used to march a set of ordinary and partial differential equations with adaptive stepsize control (Barajas & Johnsen, 2017). The spatial derivatives are discretized in radial direction with a uniform spacing Δy from the bubble center to the bubble wall using second-order central differences. The boundary conditions at the bubble center and wall are $\partial\theta_b^*/\partial y|_{y=0} = 0$ and $\theta_b^* = 0$. The number of grid points inside the bubble is $N_{in} = 1000$. To demonstrate convergence, the simulation results are compared to two limiting cases; isothermal and adiabatic gas

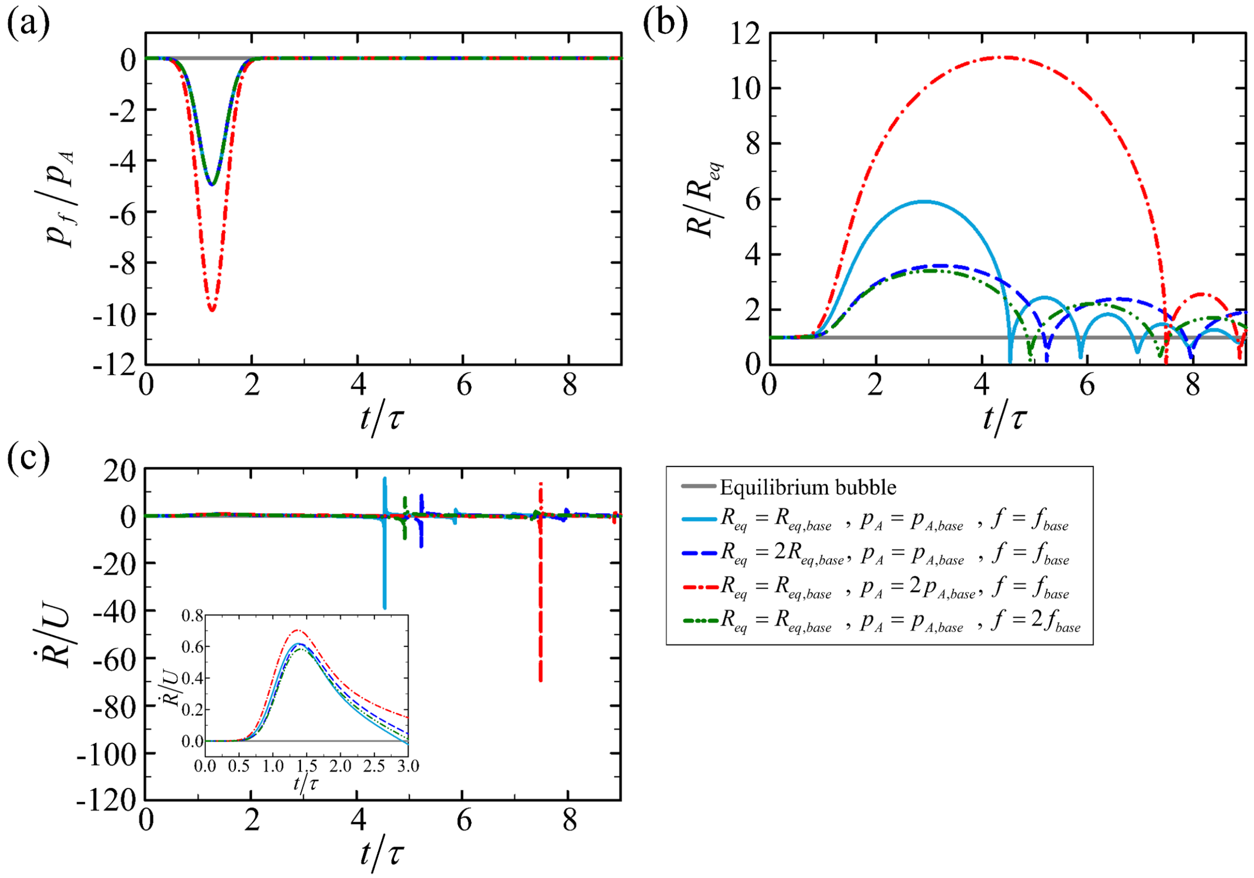

Figure 3.2: (a) Pulsed ultrasound shape for the baseline case and relevant waveforms, and correspnoding bubble oscillations: normalized (b) bubble radius and (c) bubble–wall velocity, including an equilibrium bubble case for reference; inset: bubble–wall velocity in the early stage of growth.

behavior inside the bubble, for which deviations are $< 0.2\%$ with $N_{in} = 1000$ In the following sections, we investigate the dependence of the bubble dynamics and energy transfer on the equilibrium radius and waveform properties (i.e., p_A and f) by varying these parameters in the ranges $0.1\ \mu\text{m} \leq R_{eq} \leq 10\ \mu\text{m}$, $0.1\ \text{MPa} \leq p_A \leq 5\ \text{MPa}$, and $1\ \text{MHz} \leq f \leq 10\ \text{MHz}$. This equilibrium radius range is relevant to the bubble size commonly used in contrast-enhanced ultrasound and drug delivery; the size is approximately equal to or smaller than the size of a red blood cell (Sirsi & Borden, 2009; Tung *et al.*, 2010; Patterson *et al.*, 2012). The waveform properties are selected, accounting for inertial collapse and bioeffects induced by this collapse, observed in the process of contrast-enhanced ultrasound and drug delivery (Ignee *et al.*, 2016; Cammalleri *et al.*, 2020; Versluis *et al.*, 2020).

As a baseline for this study, we consider $R_{eq,base} = 2.5$ µm with $p_{A,base} = 0.5$ MPa and $f_{base} = 1.25$ MHz, which correspond to a waveform practically used in contrast-enhanced ultrasound (Patterson *et al.*, 2012). Figure 3.2 shows different waveforms of interest along with the corresponding bubble response and bubble–wall velocity. The baseline case and other relevant waveforms are provided; in other waveforms, one of the problem parameters (i.e., R_{eq}, p_A, and f) is doubled, relative to the baseline waveform. As the bubble is exposed to tension, the bubble begins to expand, continuing its growth even after the passage of the wave. As the negative pressure decreases and approaches zero, the bubble expands more slowly, eventually reaching its largest size. The bubble then collapses due to the large pressure difference between the far field and gas inside the bubble. During the collapse, the bubble reaches a size smaller than its equilibrium radius (minimum radius). At this point, the pressure build-up within the bubble is achieved such that the bubble rebounds. For waves with larger negative peak pressure, higher bubble–wall velocities are achieved during both the growth and collapse, such that the growth is more explosive and the collapse is more violent. Hence, larger maximum radius and smaller minimum radius are achieved. For larger equilibrium radius, the growth is less explosive and the collapse is less violent because the pressure difference that drives the growth, Δp, is smaller. For higher frequency, the bubble is exposed to the negative pressure for shorter time, such that the growth is less explosive and the collapse is less violent. Clearly, the bubble oscillations are significantly affected by the problem parameters.

3.2.2 Energy budgets for bubble oscillations driven by an acoustic field

The dependence of the bubble response on the waveform properties can be explained by examining energy transfer in the liquid–bubble system, illustrated in figure 3.3. In the present study, following the theoretical framework proposed by Prosperetti & Lezzi (1986) and Yang & Church (2005), we develop a framework to distinguish the individual contributions of compressibility, viscous stresses, surface tension, and input energy from ultrasound to energy transfer. We first describe our framework and examine the energy transfer during bubble oscillations in later sectoins. The first

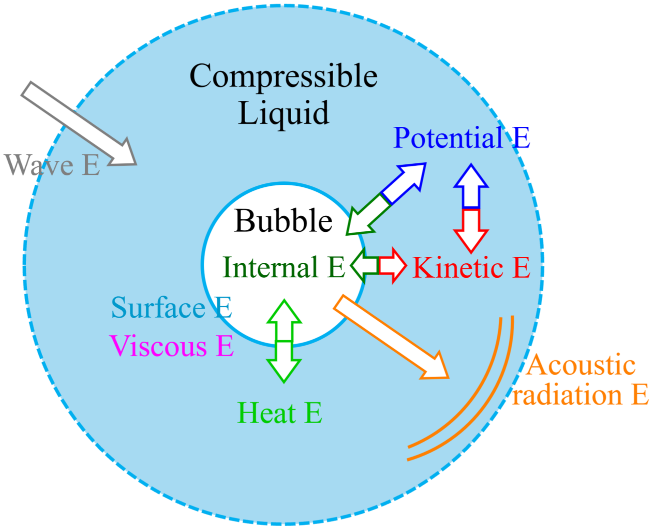

Figure 3.3: Schematic of energy transfer during bubble oscillations in a weakly compressible liquid.

law of thermodynamics states that the energy in the system must be balanced at anytime:

$$E_{TE,eq} + E_{WIE} = E_{TE}, \tag{3.15}$$

where E_{TE} is the total energy, E_{WIE} is the wave input energy, and the subscript eq indicates the quantity at equilibrium. The total energy is comprised of seven energy modes:

$$E_{TE} = E_{LPE} + E_{LKE} + E_{BIE} + E_{ARE} + E_{HEL} + E_{VIE} + E_{SFE}, \tag{3.16}$$

where E_{LPE} is the liquid potential energy, E_{LKE} is the liquid kinetic energy, E_{BIE} is the bubble internal energy, E_{ARE} is the acoustic radiation energy, E_{HEL} is the heat energy transferred to the liquid, E_{VIE} is the energy losses due to viscosity, and E_{SFE} is the surface tension energy. At equilibrium, the kinetic energy and energy losses are zero, so the total energy is

$$E_{TE,eq} = E_{LPE,eq} + E_{BIE,eq} + E_{SFE,eq}. \tag{3.17}$$

Compared to the Rayleigh collapse problem (Rayleigh, 1917) typically studied for cavitation erosion, additional mechanisms have visible effects on the energy transfer when accounting for bubble growth; waves introduce energy into the system and the effects of heat conduction and viscosity cannot be negligible in the early stage of growth.

In our analysis, we take our system to consist of a bubble in a sea of liquid. Given the conservative hydrostatic force acting on the liquid in the far-field, the potential energy stored in the liquid is (Arons & Yennie, 1948; Obreschkow *et al.*, 2006; Tinguely *et al.*, 2012; Vogel *et al.*, 1996)

$$E_{LPE} = p_\infty V. \tag{3.18}$$

The liquid kinetic energy is (Lamb, 1932; Cole, 1948; Pearson *et al.*, 2004; Wang, 2016)

$$E_{LKE} = 2\pi\rho_l R^3 \dot{R}^2. \tag{3.19}$$

For an ideal, non-condensible gas, the bubble internal energy is

$$E_{BIE} = \int \rho_g e dV = \frac{p_b V}{k-1}, \tag{3.20}$$

where ρ_g is the gas density and e is the specific internal energy. The heat conduction across the bubble wall due to temperature difference between the liquid and gas leads to changes in internal energy of the gas and liquid. Assuming a cold liquid, heat conduction across the liquid is infinitely fast. The heat energy transferred from bubble to liquid is calculated at the bubble wall:

$$\Delta E_{HEL} = 4\pi \int_0^t R^2 K_b \left(\frac{\partial T_b}{\partial r_{in}}\right)\bigg|_w \mathrm{d}t. \tag{3.21}$$

We start our analysis with Yang & Church (2005)'s framework, which provided theories to understand the terms implying external waves, viscosity, and surface tension in the KM equation. The motion of the bubble–wall is dominant near the bubble while fluctuations due to that motion are attenuated and the stresses become negligible. By matching the solutions to approximated continuity and momentum conservation equations in each sub-region, the equation of motion for bubble radius to the first order of ratio of characteristic length scales $\epsilon = U/a_l$ can be obtained:

$$R\ddot{R} + \frac{3}{2}\dot{R}^2 - \frac{\ddot{F}}{a_l} = \frac{p_l - p_\infty - p_f}{\rho_l} - \frac{\tau_{rr}(R)}{\rho_l} + \frac{3}{\rho_l}\int_R^\infty \frac{\tau_{rr}}{r}\mathrm{d}r, \tag{3.22}$$

where τ_{rr} is the normal viscous stress in the radial direction and the function accounting for liquid compressibility $\ddot{F}$ is

$$\ddot{F} = 2\dot{R}^3 + 6R\dot{R}\ddot{R} + R^2\dddot{R}. \tag{3.23}$$

The effect of bulk viscosity can be negligible for the liquid with small shear viscosity (Shen *et al.*, 2017; Nazari-Mahroo *et al.*, 2018). Equation 3.22 can be rewritten as

$$R\ddot{R} + \frac{3}{2}\dot{R}^2 - \frac{\ddot{F}}{a_l} = \frac{p_b - p_\infty - p_f}{\rho_l} - \frac{4\mu_l}{\rho_l}\frac{\dot{R}}{R} - \frac{2S}{\rho_l R}. \tag{3.24}$$

The work done by external waves (i.e., input energy introduced via waves) is

$$E_{WIE} = 4\pi\int_0^t p_f R^2\dot{R}\mathrm{d}t. \tag{3.25}$$

Work done by pressure difference across the interface is dissipated by normal viscous stresses and stored as surface tension energy (Prosperetti, 1979) as well. Thus, the energy of viscous dissipation to first-order in ϵ is

$$E_{VIE} = 16\pi\mu_l\int_0^t R\dot{R}^2\mathrm{d}t. \tag{3.26}$$

Since the surface tension only acts on the interface, the energy of surface tension is

$$E_{SFE} = 4\pi S R^2. \tag{3.27}$$

Finally, the energy losses due to acoustic radiation are

$$E_{AE} = -\frac{4\pi\rho_l}{a_l}\int_0^t F\ddot{F}\mathrm{d}t. \tag{3.28}$$

In the formulation of the KM equation, the third-order derivative of R in Eq. (3.23) is replaced by low-order derivatives while confining the error to order ϵ^2, and thus $\ddot{F}$ can be expressed as follows:

$$\ddot{F} = \frac{\dot{R}^3}{2} + R\dot{R}\ddot{R} + \dot{R}\left(\frac{p_l - p_\infty - p_f}{\rho_l}\right) + R\frac{\dot{p}_l - \dot{p}_f}{\rho_l}. \tag{3.29}$$

Thus, the acoustic radiation energy can be calculated by substituting $F = R^2\dot{R}$ and equation 3.29 into equation 3.28.

3.3 Results

3.3.1 Energy transport during bubble growth

The bubble response (i.e., $R(t)$) to the prescribed waveforms in figure 3.2 can be interpreted from an energy perspective, which we analyze in detail in this section. Figure 3.5 shows the time history of the different energy modes (described in section 3.2.2) normalized by the total energy at equilibrium and of the the rate of input energy via waves normalized by the total energy at equilibrium over acoustic period. The energy transfer during growth and collapse of a bubble can be described by dominant modes of energy transfer: (i) energy input via the ultrasound waves, (ii) liquid potential energy, (iii) liquid kinetic energy, (iv) bubble internal energy, and (v) acoustic radiation energy. As it experiences the tension, the bubble starts to grow rapidly at a high velocity (see figure 3.2(c)). The corresponding rapid increase in liquid kinetic energy implies that the energy input via the ultrasound waves, during the early stages of growth, is directly transferred to the kinetic energy. At the same time as working on the liquid, the bubble contributes to the increase in the kinetic energy although its contribution is negligible compared with the input energy. As the bubble volume

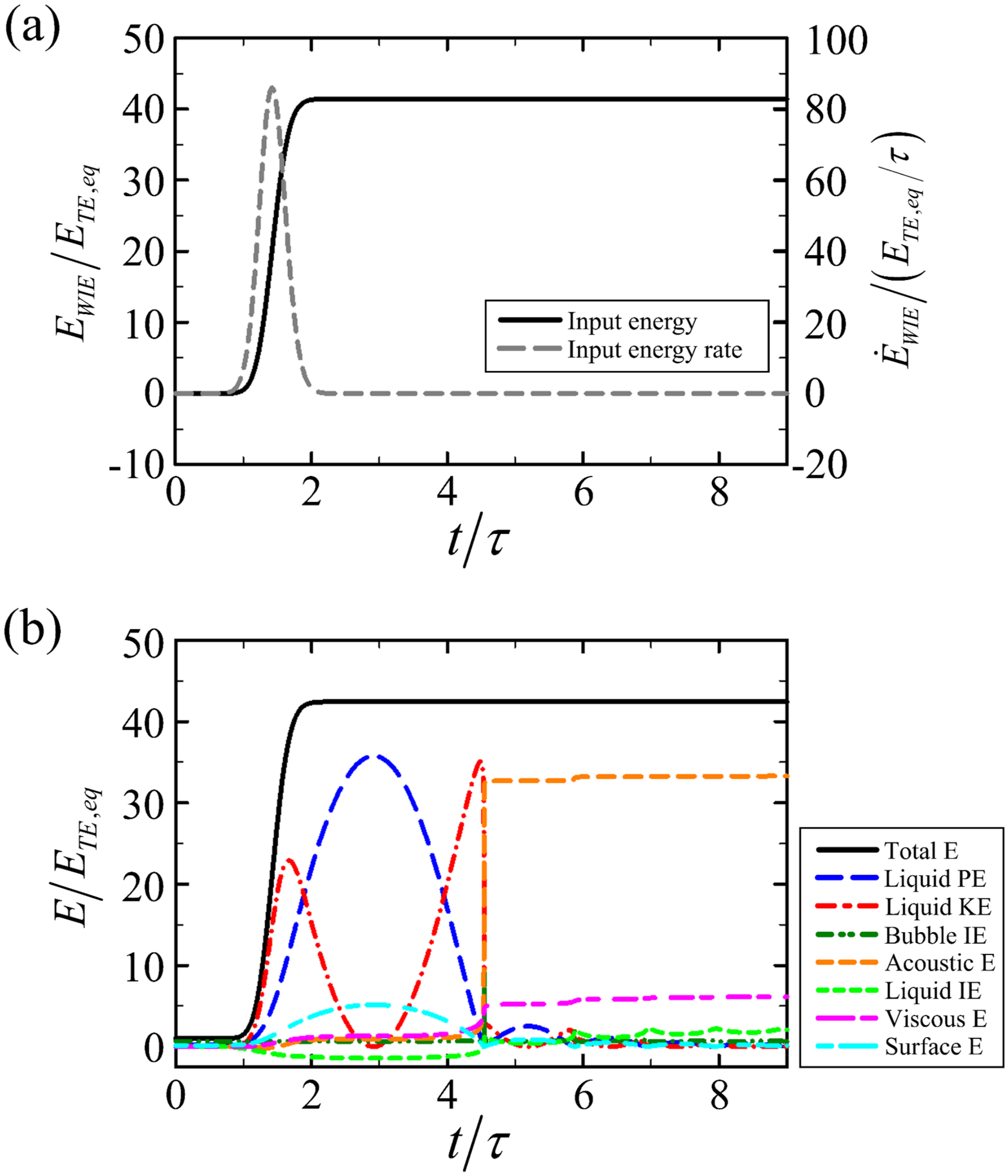

Figure 3.4: Time evolution of (a) the input energy via waves and the input energy rate, and (b) different energy modes normalized by the total energy at equilibrium and the total energy over the acoustic period for the baseline case.

increases, hydrostatic force in the far field works on the liquid, such that the potential energy of liquid rises. After the negative peak pressure of the waves passes, the rate of energy input reduces, causing the bubble–wall velocity to reduce, while the energy input continues. The bubble–wall velocity finally reaches zero as the bubble attains its largest size, at which point the liquid kinetic energy is zero and the liquid potential energy is largest. As the collapse progresses, the bubble volume decreases, also leading to a decrease in potential energy and a corresponding increase in liquid kinetic energy. In the final stages of collapse, the bubble–wall velocity rises rapidly (see figure 3.2(c)), causing large energy losses due to acoustic radiation. Simultaneously, the bubble pressure (and thus internal energy) builds up rapidly, eventually arresting the liquid and confining the gas inside the bubble. The bubble subsequently rebounds, driven by an explosion process, i.e., a localized high pressure and energy spot causing growth, which is different from the initial growth driven by a drop in local pressure near the bubble.

Interestingly, as illustrated in figure 3.5, there is an asymmetry in the kinetic energy change during growth and collapse due to two reasons. First, the initial state of growth and final state of collapse are different as growth is initiated by a drop in surrounding pressure fields rather than the high bubble pressure achieved at collapse; in laser-induced cavitation or underwater explosion, the kinetic energy change during growth and collapse would be more symmetric than the acoustic cavitation because the initial and final states are expected to be closer to each other. Secondly, the energy losses due to acoustic radiation are significant at collapse only; the Mach number corresponding to growth is much smaller than the Mach number corresponding to collapse.

Additional energy modes are present but are not significant. As the bubble grows, gas temperature inside the bubble drops, such that temperature gradient at the bubble wall drives the transfer of heat energy into the bubble, and thus the heat energy transferred to the liquid is negative and reduces during growth, as shown in figure 3.5. On the other hand, as the bubble obtains energy through heat conduction, change in the bubble internal energy is not visible during growth. Conversely, during most of the collapse, the internal energy of the bubble is transferred to the liquid through heat conduction, due to the continuously increasing gas temperature. Thus, the bubble internal energy is almost constant over time during most of the collapse. The energy losses due to viscosity are negligibly small during the growth. In the final stages of collapse, as the bubble is more compressed than its equilibrium radius, viscous effects on the energy transport cannot be ignored. The surface tension energy proportional to R^2 increases during the growth and subsequently decreases during the collapse. Even though these modes of energy transfer are not particularly sig-

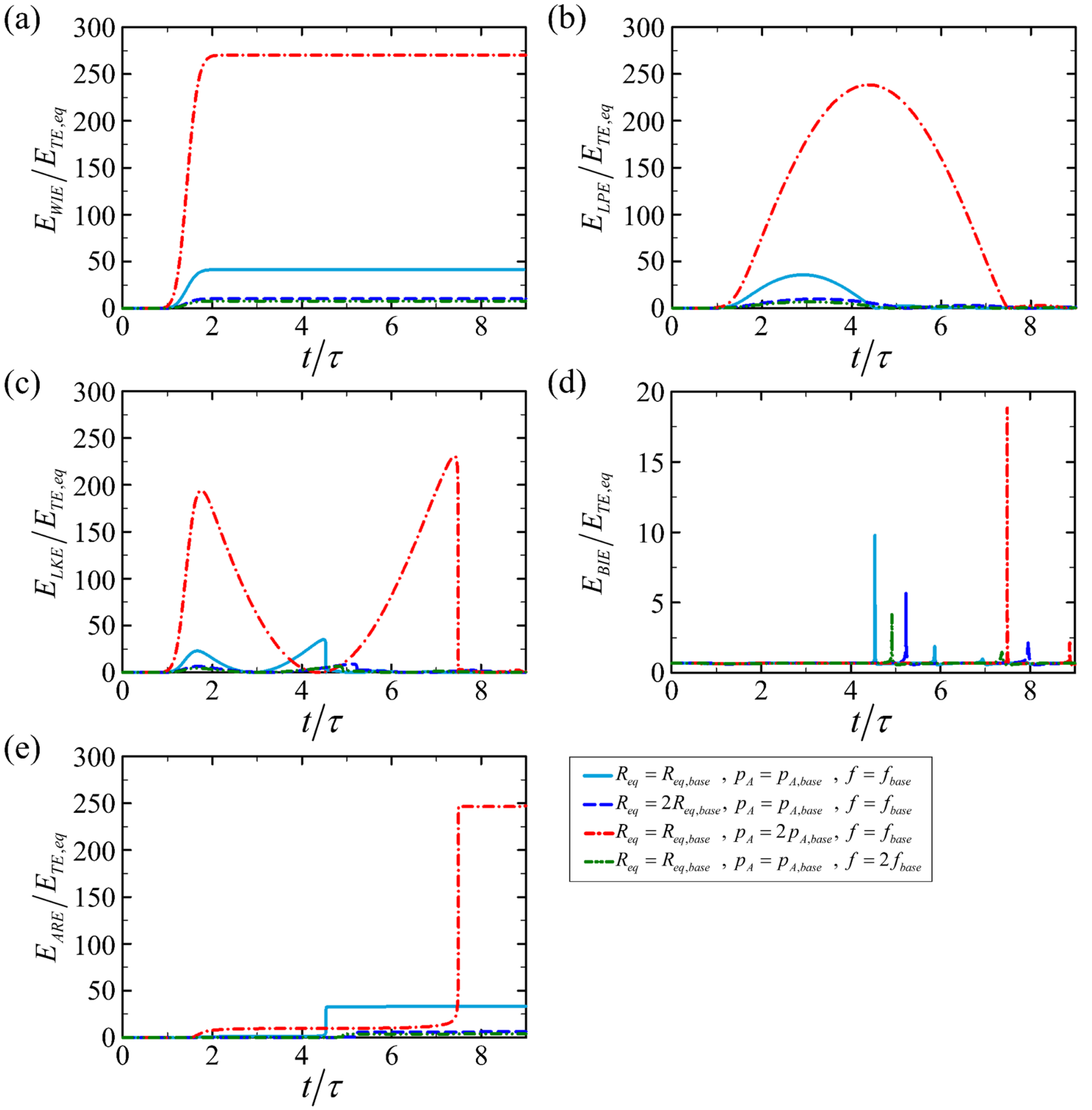

Figure 3.5: Time evolution of (a) the input energy via waves, (b) the liquid potential energy, (c) the liquid kinetic energy, (d) the bubble internal energy, and (e) acoustic radiation energy normalized by the total energy at equilibrium for the baseline case and relevant waveform cases.

nificant, they must be accurately calculated to determine the total energy that no longer changes once the wave has passed and the input energy rate has become zero.

Change in the problem parameters (i.e., R_{eq}, p_A, f) leads to large difference in energy transfer during bubble growth, compared to the baseline case. Figure 3.2 shows the time evolution of dominant modes of energy transfer for the baseline case and other relevant waveforms, as illustrated in figure 3.2. For all cases, a general trend in energy transfer is similar; the energy input introduced in the early stages of growth is transferred to the kinetic energy of liquid, which is ultimately transferred to the potential energy of liquid at maximum bubble size. During bubble collapse, the potential energy of liquid is concentrated into the bubble, while some of the potential energy is lost through acoustic radiation. However, the amount of energy transferred between energy modes depend upon the bubble response to different waveforms. As shown in figure 3.2(a), for waves with larger negative peak pressure, a greater amount of energy is introduced to the system via waves due to more explosive growth. Hence, the liquid attains larger kinetic and potential energy during the growth. Similar to the growth, the collapse is also more violent, such that more energy is concentrated into the bubble and more energy is lost through acoustic radiation, relative to the total energy at equilibrium. Conversely, for larger equilibrium radius, the growth is less explosive, such that a smaller amount of energy is introduced to the system, leading to weak energy transfer during the growth and collapse. Similarly, for higher frequency, the shorter exposure time of bubble to the negative pressure causes the limited energy input, which provides a smaller amount of energy into the energy modes. Thus, understanding of the dependence of the bubble response on the waveform is crucial to describe the relationship between the waveform and the energy transfer in the system.

3.3.2 Dependence of the bubble radius and energy at maximum size on the problem parameters

The state of the system (e.g., bubble size, energy) is important as it often serves as a starting point in experimental (Vogel *et al.*, 1989; Tinguely *et al.*, 2012; Supponen *et al.*, 2016, 2017), computational (Johnsen & Colonius, 2009; Beig *et al.*, 2018), and theoretical (Brennen, 1995; Kim *et al.*, n.d.) studies. In this section, we first determine the dependence of key properties (i.e., maximum bubble radius, and bubble pressure and energy modes at maximum size) on the problem parameters, namely the wave amplitude and frequency, as well as the equilibrium radius. Figure 3.6 shows the dependence of maximum bubble radius and bubble pressure at maximum size on

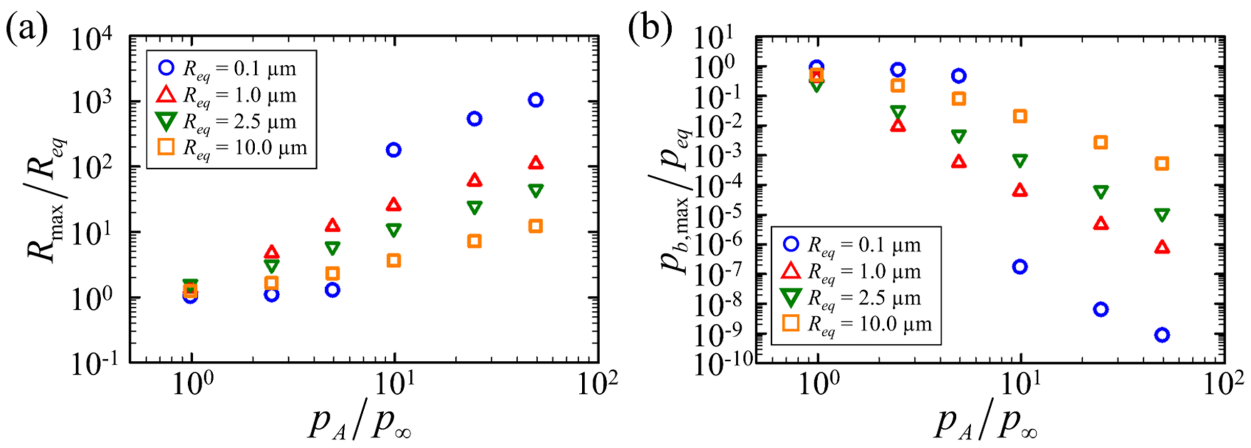

Figure 3.6: (a) Maximum bubble radius normalized by equilibrium radius and (b) bubble pressure at maximum size normalized by equilibrium pressure as a function of normalized peak negative pressure for R_{eq} = 0.1–10 μm; $f = f_{base}$.

the wave amplitude for different equilibrium radii, which are used to equations 3.31 and 3.32 to predict bubble radius and energy at collapse, as well as shock emission. As the wave amplitude is increased, larger amount of energy is introduced to the system, such that the normalized maximum radius rises, and thus the bubble pressure at maximum size reduces. In particular, at $p_A/p_\infty < 10$, the bubble growth for R_{eq} = 0.1 μm is negligibly small due to large surface tension that suppresses bubble growth, such that the bubble undergoes a small-amplitude oscillation. At $p_A/p_\infty > 10$, the bubble grows more explosively for smaller equilibrium radii because of larger driving pressures for growth. Accordingly, the bubble pressure at maximum size becomes smaller.

The energy modes at maximum size also exhibits a similar trend to the bubble expansion. Figure 3.7 shows the dependence of dominant modes of energy transfer at maximum size on the wave amplitude for different equilibrium radii. As the wave amplitude is increased, more energy is introduced to the system via waves as the bubble grows more explosively. Since the bubble–wall attains higher velocities, more input energy is transferred to the kinetic energy in the early stages of the collapse, which is ultimately stored as the potential energy in liquid. In addition, as the bubble–wall attained higher velocities, the bubble loses more energy through acoustic radiation. Interestingly, the internal energy of bubble does not depend on the wave amplitude due to isothermal process of gas during bubble growth. As it grows, the bubble works on the liquid, such that

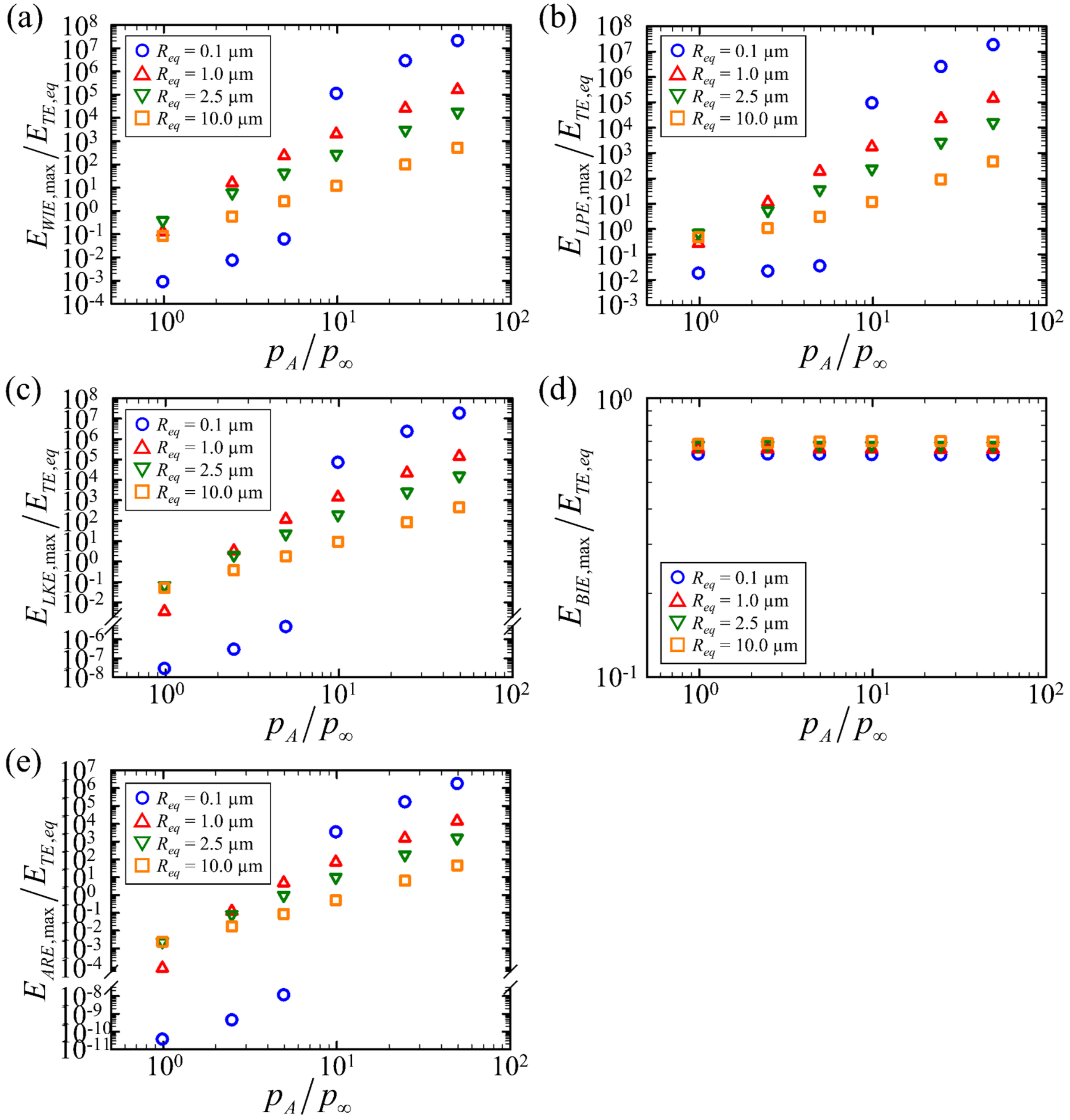

Figure 3.7: (a) Input wave energy and (b) liquid potential energy at maximum size, (c) maximum kinetic energy during growth, (d) bubble internal energy and (e) acoustic radiation energy at maximum size normalized by the total energy at equilibrium as a function of normalized peak negative pressure for R_{eq} = 0.1–10 μm; $f = f_{base}$.

gas temperature inside the bubble drops. Then, due to high thermal conductivity of liquid, heat energy instantaneously supplements the decrease in the internal energy of bubble. Thus, the overall change in bubble internal energy is negligibly small, and the bubble maintains most of its initial

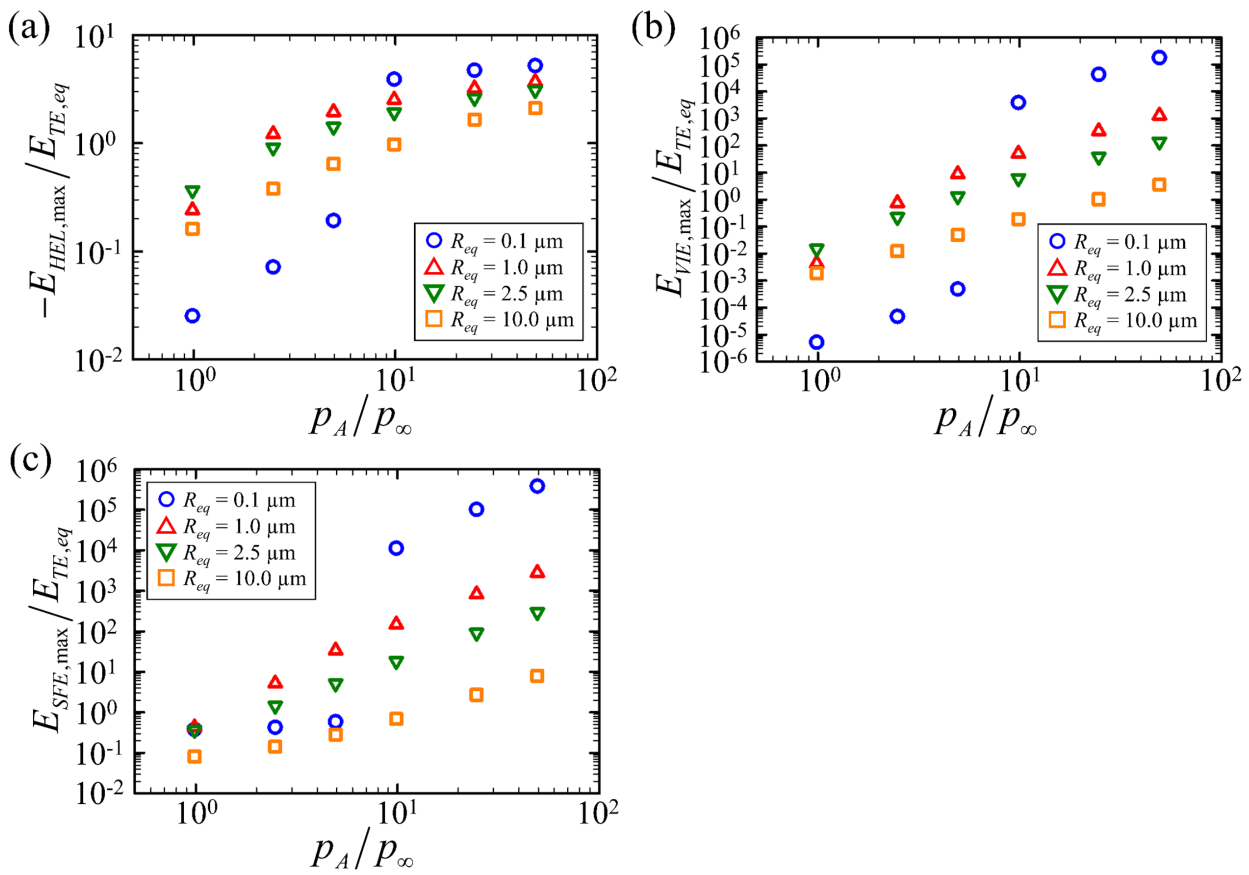

Figure 3.8: (a) Negative value of heat energy transferred to the liquid, (b) energy losses due to viscosity, and (c) surface tension energy at maximum size normalized by the total energy at equilibrium as a function of normalized peak negative pressure for R_{eq} = 0.1–10 μm; $f = f_{base}$.

internal energy during the growth. As also shown in figure 3.6, at $p_A/p_\infty < 10$, the change in each energy mode is negligible for R_{eq} = 0.1 μm, while at $p_A/p_\infty > 10$, more energy is provided and transferred to other energy modes for R_{eq} = 0.1 μm. The initial internal energy of bubble depends on the bubble size; larger equilibrium bubble contains more internal energy, such that for larger equilibrium radii, the bubble has more energy at maximum size.

Other energy modes also shows a similar trend although their effects on energy transport are not significant. Figure 3.8 shows the dependence of energy modes at maximum size, which are less significant in energy transport (i.e., heat energy transferred to the liquid, energy losses due to viscosity, and surface tension energy), on the wave amplitude for different equilibrium radii. Negative values of heat energy are shown to plot them in a logarithmic scale. Again, similar trends

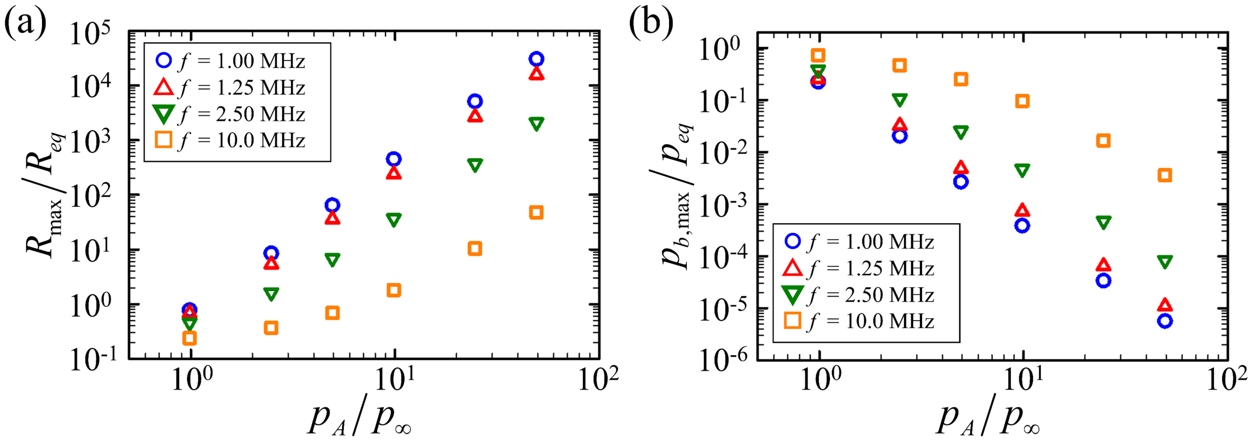

Figure 3.9: (a) Maximum bubble radius normalized by equilibrium radius and (b) bubble pressure at maximum size normalized by equilibrium pressure as a function of normalized peak negative pressure for $f = 1$–10 MHz; $R_{eq} = R_{eq,base}$.

are also observed in those energy modes, indicating that the larger wave amplitude and smaller equilibrium radius lead to a larger amount of energy transfer.

The bubble response and energy transfer during bubble growth are also depend on the wave frequency. Figure 3.9 shows the dependence of the maximum bubble radius and bubble pressure at maximum radius on the wave frequency and amplitude. For a given wave amplitude, the maximum bubble radius rises as the wave frequency decreases because the bubble is exposed to negative pressures for a longer time. Thus, the bubble pressure at maximum size decreases. As discussed in figure 3.6, for larger wave amplitudes, the bubble attains larger maximum radius, and accordingly, the bubble pressure decreases.

The dominant modes of energy transfer also depend on the wave frequency. Figure 3.10 shows the dependence of the dominant modes of energy transfer on the wave frequency and amplitude. For a given wave amplitude, the bubble grows more explosively at smaller frequencies, such that more input energy is introduced to the system, which is transferred to other dominant energy modes, such as the kinetic and potential energy of liquid. Furthermore, at smaller frequencies, the bubble–wall reaches higher velocities, such that more energy is lost through acoustic radiation. The wave frequency has negligible effects on the bubble internal energy at maximum size because this energy does not change during the growth due to large heat energy input to the bubble. For different frequencies, the initial internal energy of bubble is the same, such that the bubble internal energy at maximum size collapses to a single value for a given wave amplitude. As discussed in figure 3.7, for larger wave amplitudes, a greater amount of energy is achieved in each dominant mode, excepted for the bubble internal energy, which are almost the same for different wave amplitudes.

Other energy modes relevant to heat conduction, viscosity and surface tension depend on the wave frequency although their contributions to the overall energy transport are not significant. Figure 3.11 shows the dependence of those energy modes on the wave frequency and amplitude. For a given wave amplitude, larger input energy is introduced at smaller frequencies, such that a larger amount of energy is transferred through heat conduction and viscosity and is stored as the surface tension energy.

The dependence of the bubble response and energy transport on the problem parameters can be summarized as follows: for larger wave amplitudes, smaller equilibrium radius, and smaller wave frequencies, the bubble grows more explosively at higher bubble–wall velocities, such that larger normalized maximum bubble radius and energy modes at maximum size are achieved. Under some circumstances (e.g., small equilibrium radius and wave amplitude), the bubble undergoes a small amplitude oscillation. The bubble maintains its internal energy at equilibrium due to instantaneous heat energy input from the surrounding liquid.

3.3.3 Modeling for predicting maximum bubble radius and energy at maximum size

During bubble growth, the bubble response and energy transport shows a similar trend for different problem parameters, indicating the presence of possible scaling relations that can universally describe their dependency on the problem parameters. In the following, we investigate the dependence of the maximum bubble radius and each energy mode at maximum size on a single dimensionless parameter that can represent the waveform properties and equilibrium bubble. For theoretical analysis of the relation between the Gaussian pulse and corresponding bubble responses, we start our analysis with the top-hat waveform to derive the analytical relation. Then,

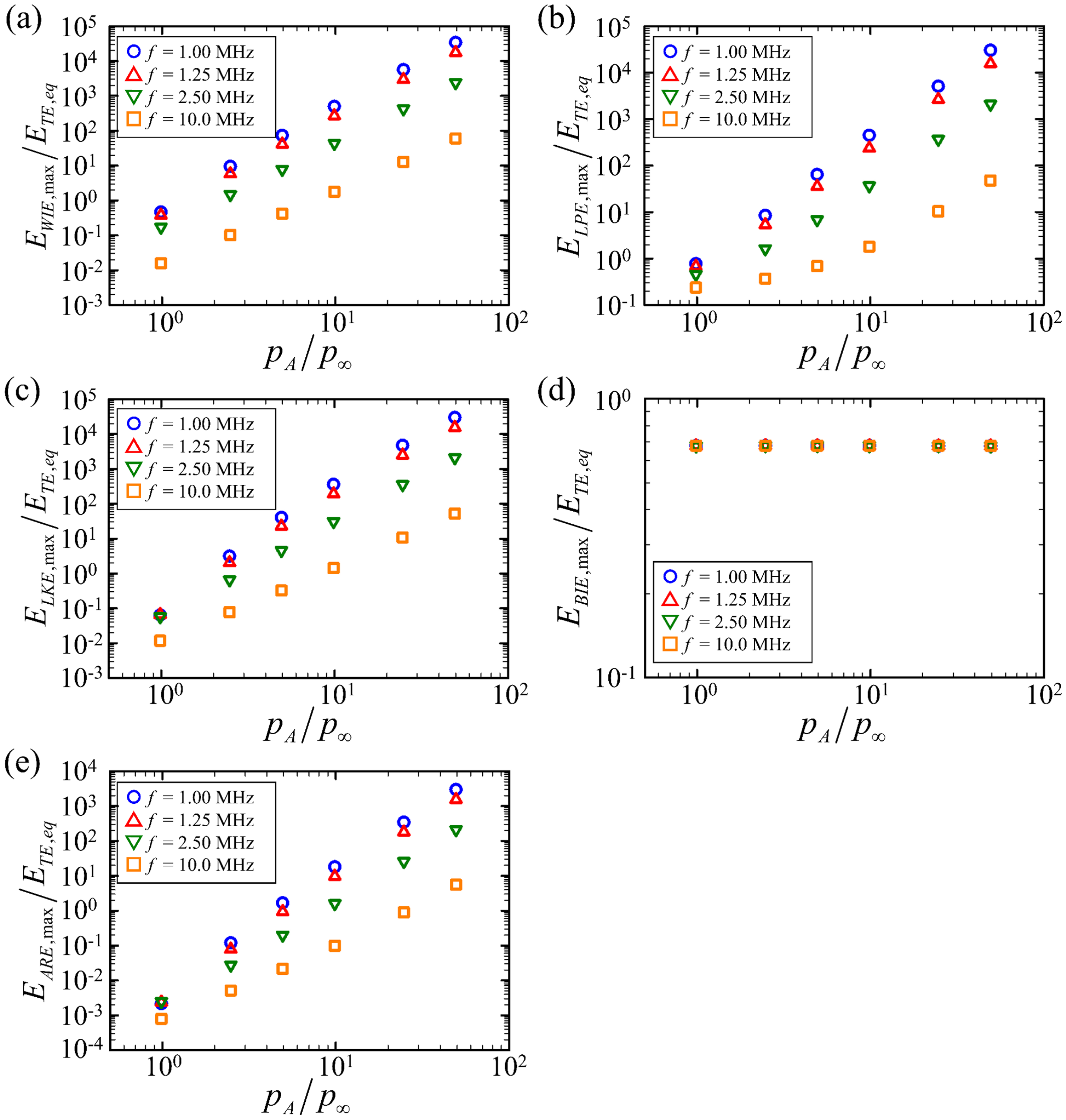

Figure 3.10: (a) Input wave energy and (b) liquid potential energy at maximum size, (c) maximum kinetic energy during growth, (d) bubble internal energy and (e) acoustic radiation energy at maximum size normalized by the total energy at equilibrium as a function of normalized peak negative pressure for f = 1–10 MHz; $R_{eq} = R_{eq,base}$.

we apply this relation to describe the maximum bubble radius and energy at maximum size for the Gaussian waveform case.

The partition of each energy mode of the total energy at maximum size is useful to assess the

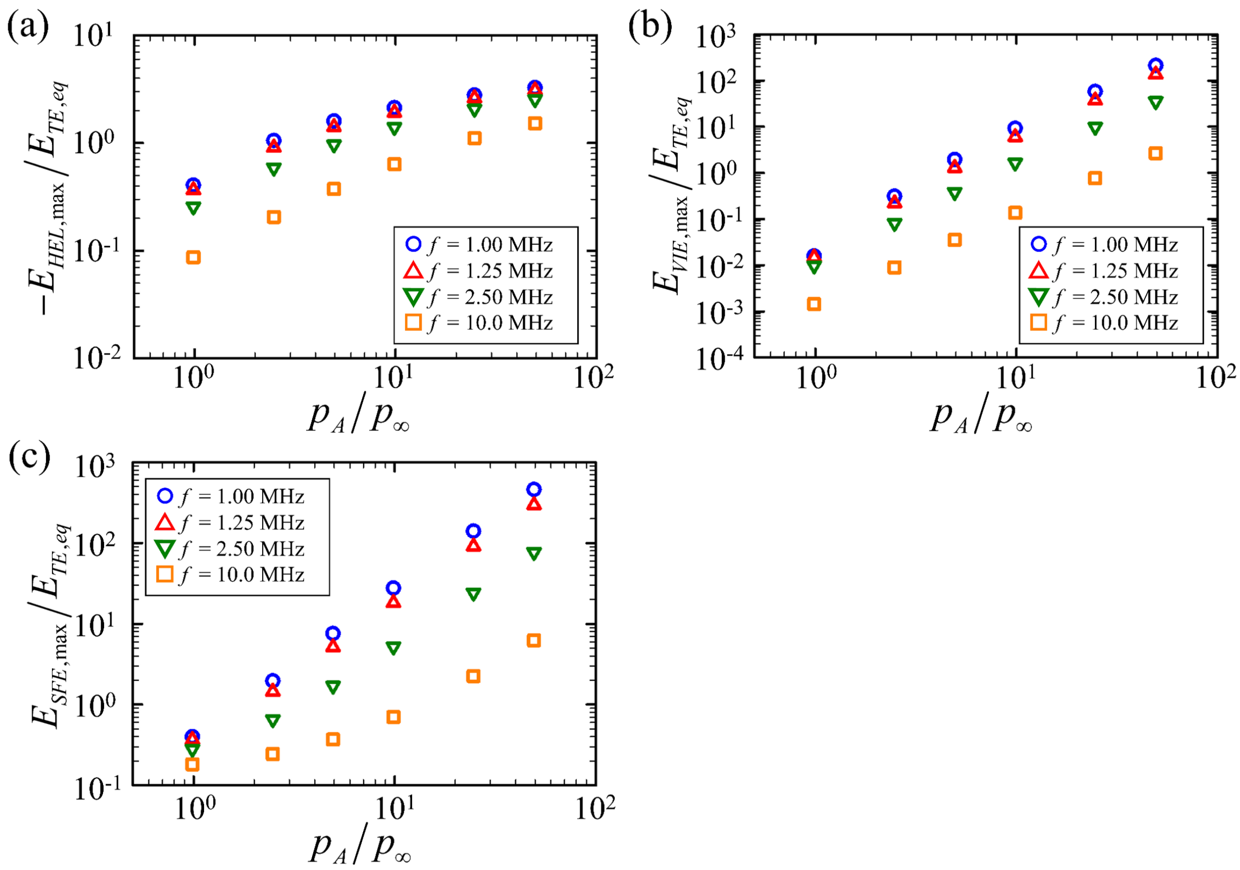

Figure 3.11: (a) Negative value of heat energy transferred to the liquid, (b) energy losses due to viscosity, and (c) surface tension energy at maximum size normalized by the total energy at equilibrium as a function of normalized peak negative pressure for f = 1–10 MHz; $R_{eq} = R_{eq,base}$.

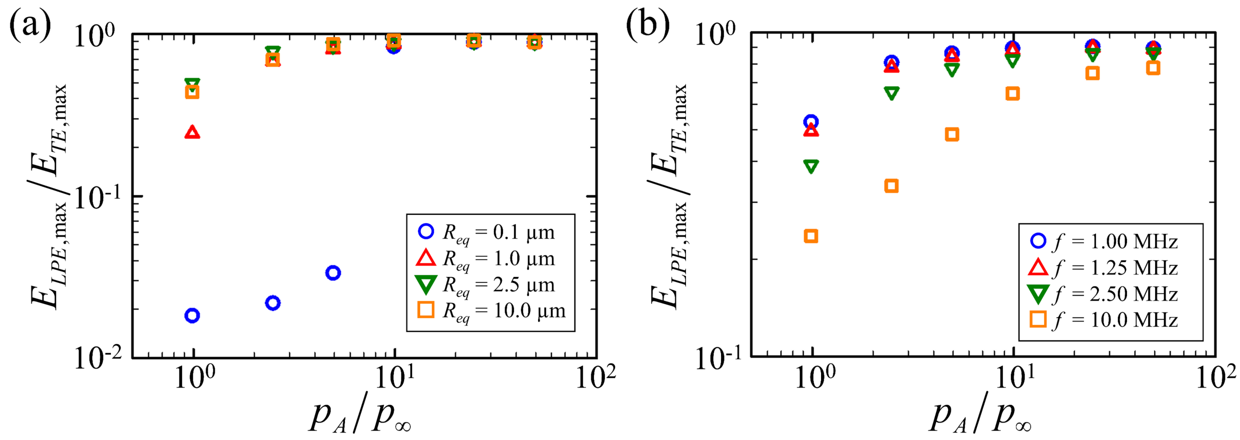

Figure 3.12: Liquid potential energy at maximum size normalized by total energy at maximum size for (a) R_{eq} = 0.1–10 μm and $f = f_{base}$, and for (b) f = 1–10 MHz and $R_{eq} = R_{eq,base}$ as a function of the wave amplitude.

dominant energy mode in the system at maximum size. Figure 3.12 shows the liquid potential energy at maximum size normalized by the total energy at maximum size. For larger wave amplitudes, more fraction of the total energy is stored as the potential energy of liquid for different bubble radii and frequencies. In addition, for smaller wave frequencies, more faction of the total energy is stored as the potential energy. Thus, the energy balance equation (3.15) can be simplified as

$$E_{WIE} \approx E_{LPE}, \tag{3.30}$$

which is expressed as

$$-\int_0^{t'} p_f \left(4\pi R^2 \dot{R}\right) \mathrm{d}t' = p_\infty V_{max}. \tag{3.31}$$

Then, for top-hat waveform, which has a rectangle shape and consists of constant flat pressures between zero pressures, Eq. (3.31) is given by

$$p_A \frac{4\pi}{3} \left[R(\tau)^3 - R_{eq}^3\right] = p_\infty \frac{4\pi}{3} R_{max}^3, \tag{3.32}$$

where τ is the acoustic period and $R(\tau)$ is the bubble radius at $p_f = 0$. In the early stages of the growth, the bubble–wall velocity rapidly increases to the inertial growth velocity $\sqrt{2p_A/3\rho_l}$ and is saturated during most of the growth (Apfel, 1981, 1982; Leighton, 2012). The time duration for achieving this saturated velocity (i.e., inertial velocity-rising time) is given by $t_I = R_{eq}\sqrt{3\rho_l/2p_A}$. For large wave amplitudes or frequencies, we can assume $t_I \ll \tau$, such that $R(\tau)$ is given by

$$R(\tau) = R_{eq} + \tau \sqrt{\frac{2p_A}{3\rho_l}}. \tag{3.33}$$

Since $R(\tau) \gg R_{eq}$ for large p_A or τ, substituting Eq. (3.33) into Eq. (3.32) gives

$$\frac{R_{max}}{R_{eq}} \approx \left(\frac{p_A}{p_\infty}\right)^{\frac{1}{3}} \left(\frac{t_I}{\tau}\right)^{-1} = \eta, \tag{3.34}$$

where the term in the right-hand side is defined as a single dimensionless parameter η, and $R_{max}/R_{eq} \approx$

η. This relation implies that the expansion ratio of the bubble is determined by two parameters; acoustic pressure ratios p_A/p_∞ and inertial-to-acoustic time ratios t_I/τ. For larger pressure amplitudes, the acoustic pressure ratio rises and the inertial velocity-rising time reduces, such that the bubble grows with larger expansion ratios. For longer acoustic periods, the expansion ratio becomes larger because the bubble is exposed to negative pressure for longer times. To understand both growth and collapse of the bubble using initial conditions, we also find the relation for the gas pressure inside the bubble at $R = R_{max}$. Since the bubble growth tends to be isothermal (Leighton, 2012) due to its thermal penetration length $\sqrt{\alpha_b(R_{eq}/U)}$ comparable to R_{eq}, the gas pressure becomes

$$\frac{p_{b,max}}{p_{eq}} = \left(\frac{R_{eq}}{R_{max}}\right)^3 \approx \left(\frac{p_A}{p_\infty}\right)^{-1}\left(\frac{t_I}{\tau}\right)^3 = \eta^{-3}. \tag{3.35}$$

Eqs. (3.34) and (3.35) are derived for the top-hat waveform. However, the Gaussian waveform can be approximated to the corresponding top-hat waveform as follows. As the waves act on the bubble, the bubble–wall velocity rises from zero to the saturated velocity, leading to the rapid bubble expansion in the early stages of the growth, $\dot{R} \approx \sqrt{(2/3)(p_A/\rho_l)}$, such that the bubble radius during the growth can be estimated by $R = \int_o^t \dot{R}(t')\mathrm{d}t'$. R and $\dot{R}$ are substituted into Eq. (3.25) to approximate the energy provided by the Gaussian waveform $E_{WIE,gauss}$. The amplitude of the top-hat waveform $p_{A,TH}$ is set to be same as p_A of the Gaussian waveform. To make the top-hat waveform producing the same energy, we evaluate the acoustic period of the top-hat waveform τ_{TH} as follows:

$$\tau_{TH} = E_{WIE,gauss} \Bigg/ \left[\frac{4\pi}{3}\left(\frac{2}{3}\right)^{3/2}\frac{p_{A,TH}^{5/2}}{\rho_l^{3/2}}\right]. \tag{3.36}$$

Using the input wave energy by the Gaussian waveform, we find the corresponding top-hat waveform (i.e., τ_{TH} and p_A). Figure 3.13 shows the Gaussian waveform and the corresponding top-hat waveform for the baseline case and the dependence of the input energy introduced by those waveforms on the wave amplitude. The estimated energy $E_{WIE,gauss}$ using the approximated top-hat waveform shows good agreement with the exact input energy by the Gaussian waveform at various acoustic pressure ratios.

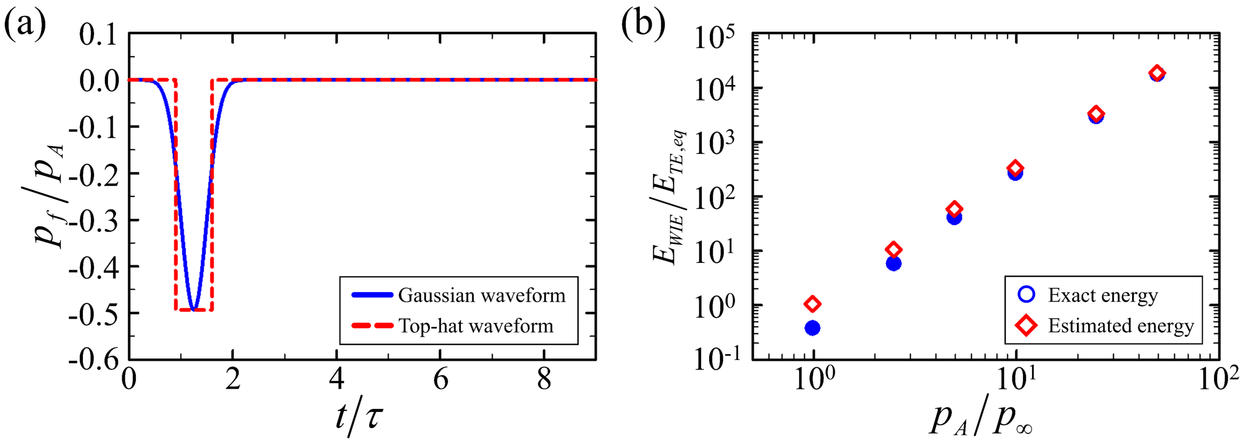

Figure 3.13: (a) Waveform of the Gaussian pulse and approximated top-hat wave for the baseline case and (b) their input energy for $R_{eq} = R_{eq,base}$ and $f = f_{base}$ as a function of the normalized wave amplitude.

Making use of Eqs. (3.34) and (3.35), we derive the relations between energy at maximum size and initial conditions as follows. The input energy provided by waves normalized by equilibrium energy is given by

$$\frac{E_{WIE,max}}{E_{TE,eq}} \approx \frac{(4\pi/3)p_A R(\tau)^3}{p_{eq}V_{eq}/(k-1)} = (k-1)\left(\frac{p_A}{p_\infty}\right)^{-1}\left(\frac{t_I}{\tau}\right)^3\left(\frac{p_\infty}{p_{eq}}\right) = (k-1)\eta^3\left(\frac{p_\infty}{p_{eq}}\right), \tag{3.37}$$

where p_∞/p_{eq} is the equilibrium pressure ratio. While the expansion ratio is solely described by η, the energy is described by two parameters: η and equilibrium pressure ratio. Since it is assumed that most of the input energy is transferred to the liquid kinetic energy during the growth and finally stored as the potential energy in liquid, Eq. (3.37) can also describe the maximum liquid kinetic energy during the growth and liquid potential energy at maximum size.

The normalized maximum bubble radius and bubble pressure at maximum size can be described by Eqs. (3.34) and (3.35). Figure 3.14 shows the dependence of the maximum bubble radius and bubble pressure at maximum size for different bubble radii, wave amplitudes, and wave frequencies on η. The relations (3.34) and (3.35) correctly describe the bubble growth ratio for larger η, indicating that the bubble growth ratio rises for larger acoustic pressure ratios and smaller inertial-to-acoustic time ratios. In particular, as the bubble growth begins with smaller equilibrium

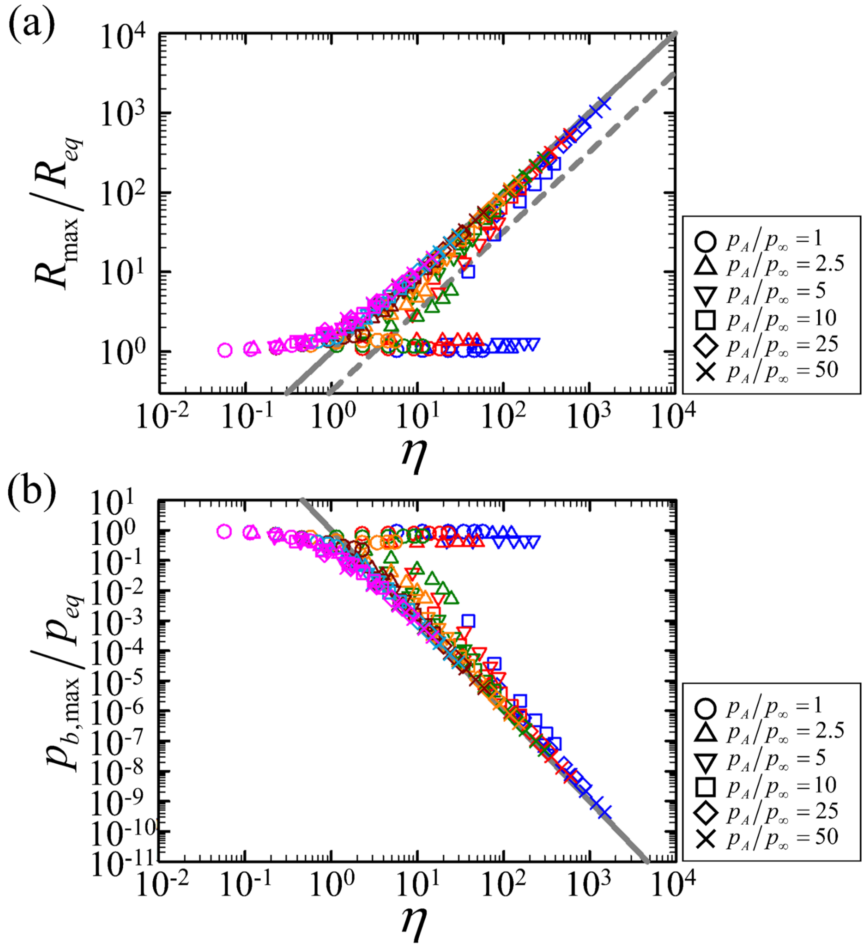

Figure 3.14: (a) Maximum bubble radius normalized by equilibrium bubble radius and (b) bubble pressure at maximum size normalized by equilibrium bubble pressure for $p_A/p_\infty = 1 - 50$ and $f = 1 - 10$ MHz as a function of a single dimensionless parameter η; R_{eq} = (blue) 0.1 μm, (red) 0.25 μm, (green) 0.5 μm, (orange) 1 μm, (brown) 2.5 μm, (cyan) 5 μm, and (pink) 10 μm; solid line: Eq. (3.34); dashed line: $R_{max}/R_{eq} = \eta(2^{4/3}/3^{5/6}\pi)$ (Apfel, 1981).

radii, the bubble–wall reaches the saturated (maximum) velocity more rapidly, such that the bubble reaches larger maximum size with smaller bubble pressure, compared to its equilibrium values. For smaller η, there are some differences between scaling relations and the simulation results because (i) inertial velocity-rising time is comparable to acoustic period and (ii) wave amplitude is comparable to the equilibrium gas pressure or far-field liquid pressure. The scaling relation proposed by Apfel (1981), $R_{max}/R_{eq} = \eta(2^{4/3}/3^{5/6}\pi)$, is introduced in figure 3.14(a) and shows some discrepancies with the calculated expansion ratios. Because only the continuous sine waveform is treated in their study to understand the forced bubble oscillation, their relations cannot be directly used for

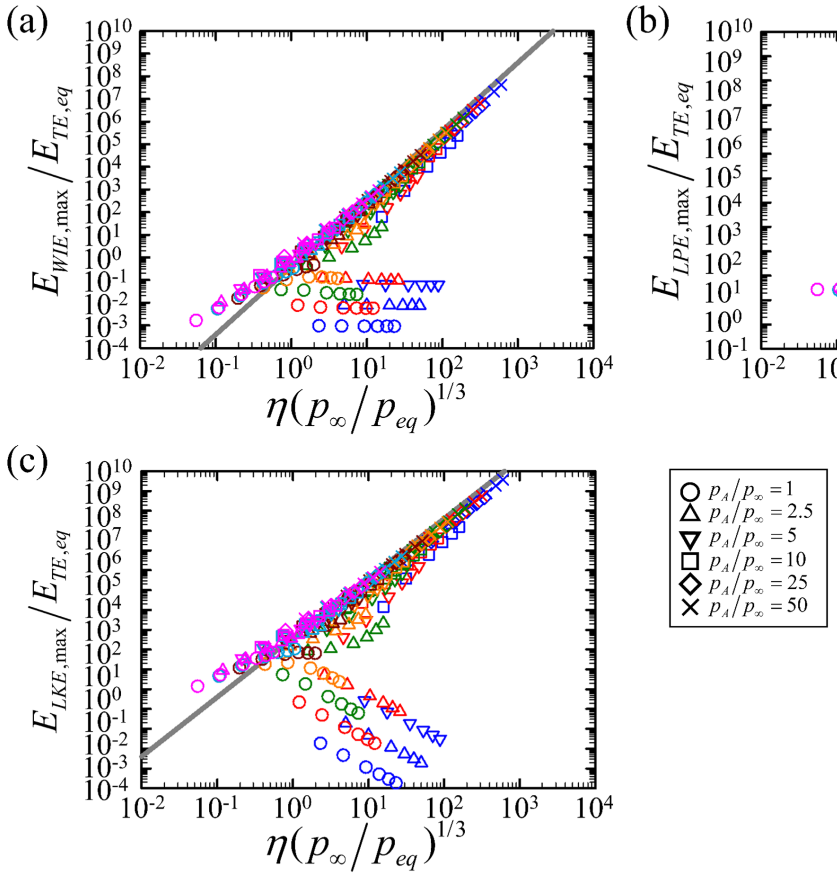

Figure 3.15: (a) Input wave energy, (b) liquid potential energy, and (c) liquid kinetic energy normalized by the total energy at equilibrium for $p_A/p_\infty = 1 - 50$ and $f = 1 - 10$ MHz as a function of $\eta(p_\infty/p_{eq})^{(}1/3)$; R_{eq} = (blue) 0.1 µm, (red) 0.25 µm, (green) 0.5 µm, (orange) 1 µm, (brown) 2.5 µm, (cyan) 5 µm, and (pink) 10 µm; solid line: Eq. (3.37).

the pulsed ultrasound waveform (i.e., Gaussian waveform), where the acoustic period need to be accurately evaluated in the scaling relations.

The normalized energy modes at maximum size can be described by Eq. (3.37). Figure 3.15 shows the dependence of the input energy, and potential and kinetic energy of liquid normalized by equilibrium total energy on acoustic pressure ratios and periods, and equilibrium bubble radius. Larger maximum bubble radius leads to larger energy input, and correspondingly, larger maximum kinetic energy and potential energy at maximum size. Hence, for larger amplitudes, longer acoustic periods, and smaller equilibrium radius, more energy is provided to the system and is finally stored to the potential energy at maximum size. Eq. (3.37) correctly describes the energy mode illustrated in figure 3.15, while there exists some deviations from the simulation results at smaller

$\eta(p_\infty/p_{eq})^{1/3}$ because the assumptions used for deriving the scaling relations are not valid at this regime. When the pressure amplitude or equilibrium bubble radius is smaller than some thresholds, the bubble maintains its equilibrium state or undergoes stable oscillations, such that the expansion ratios and gas pressures at maximum size are close to one, and energy ratios are much smaller than one. This will be discussed in section 3.4.

3.4 Discussion

3.4.1 Application of energy budget framework to histotripsy

Our energy budget framework and scaling relations can readily be applied to other various waveforms for therapeutic ultrasound. In the present study, we choose the ultrasound waveform to predict the maximum bubble radius using our scaling relations, which is closely relevant to tissue damage induced by bubble oscillations in histotripsy. The waveform for the intrinsic-threshold histotripsy is given by (Mancia *et al.*, 2020, 2021):

$$p_f = \begin{cases} p_A \left[\frac{1+\cos[\omega(t-\delta)]}{2}\right]^n, & |t-\delta| \leq \frac{\pi}{\omega}, \\ 0, & |t-\delta| > \frac{\pi}{\omega}, \end{cases} \tag{3.38}$$

where p_A is the peak amplitude, f is the frequency, and $\omega = 2\pi f$, $\delta = 5$ µs, $n = 3.7$, and the gas nuclei size is $O(1\text{–}10)$ nm. As described in section 3.3.3, the histotripsy waveform is projected to obtain the corresponding top-hat waveform and τ as preserving the total input energy by the histotripsy waveform. Similar to the Gaussian form cases in section 3.3.3, larger acoustic pressure ratios and inertial-to-acoustic rime ratios lead to larger bubble expansion ratios. The scaling relation (Eq. (3.34)) shows a good agreement with the histotripsy waveform case. This is because for explosive bubble growth, most of the input energy is finally stored as the potential energy of liquid, which is the fundamental assumption used to derive the scaling relation. Therefore, our framework and scaling relations introduced in section 3.3 provides a baseline case to predict damage potential

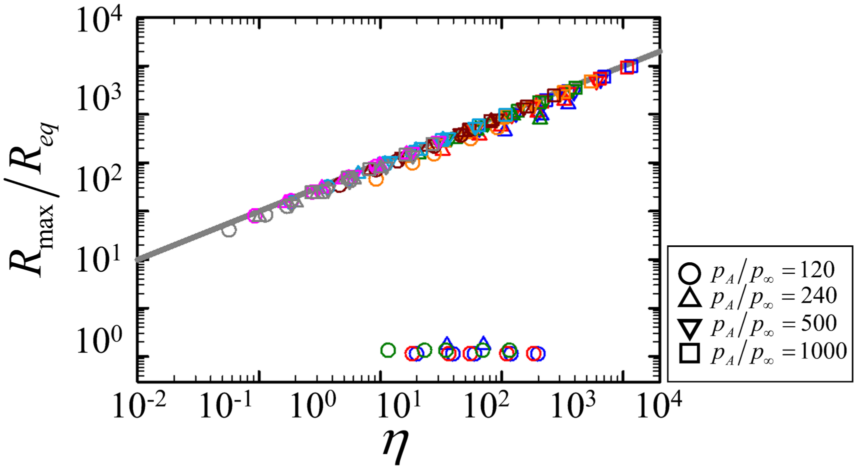

Figure 3.16: Maximum bubble radius normalized by equilibrium radius for $p_A/p_\infty = 120 - 1000$ and $f = 0.3 - 3$ MHz as a function of η; R_{eq} = (blue) 2.32 nm, (red) 2.5 nm, (green) 4 nm, (orange) 5 nm, (brown) 10 nm, (cyan) 25 nm, (pink) 50 nm, and (gray) 100 nm; solid line: Eq. (3.34)

in oscillating bubbles surrounded by medium.

3.4.2 Cavitation thresholds for bubble growth

As observed in figures 3.14, 3.15, and 3.16, there exist two distinct regimes that classifies the bubble behavior during the growth. At lower acoustic pressure ratios, the bubble oscillation is affected by the surface tension, leading to the stable oscillation. For smaller bubble radius where the surface tension becomes more significant, the bubble oscillation tends to be stable at larger acoustic pressure ratios. On the other hand, at higher acoustic pressure ratios, the bubble grows explosively and collapse violently, such that bubble oscillations have remarkable effects on surrounding medium. These two regimes can be theoretically classified using the perturbation theory (Blake, 1949; Brennen, 1995; Mancia *et al.*, 2020). With the small perturbation $\epsilon \ll 1$, $R = R_{eq}(1+\epsilon)$, the Rayleigh–Plesset equation is linearized, and the stability of the solutions is evaluated to get the critical pressure amplitude (i.e., the Blake threshold pressure):

$$\left(\frac{p_A}{p_\infty}\right)_{Blake} = 1 + \frac{8}{9}\left(\frac{S}{p_\infty R_{eq}}\right)\sqrt{\frac{3S/R_{eq}}{2k(p_\infty + 2S/R_{eq})}}, \tag{3.39}$$

and this equation can be rewritten as

$$R_{eq,Blake} = \left(\frac{1}{3k} - 1\right)\left(\frac{2S}{p_\infty - p_A}\right), \tag{3.40}$$

where the equilibrium is stable and the bubble undergoes stable oscillations at $p_A < P_{A,Blake}$ or $R_{eq} < R_{eq,Blake}$. The equilibrium becomes unstable at $p_A > P_{A,Blake}$ or $R_{eq} > R_{eq,Blake}$. It should be noted that only the peak pressure amplitude determines whether the oscillations are stable or unstable; the bubble would undergo stable oscillation for longer acoustic periods if the pressure amplitude is smaller than the Blake threshold pressure. However, once the oscillation becomes unstable, the bubble achieves larger maximum radius and longer acoustic periods, as observed in figures 3.14 and 3.16.

While the equilibrium state and bubble growth are focused on understanding the bubble oscillations, the bubble collapse is also essential to describing the effects of bubble oscillations on surrounding medium. As comparing the inertial term (i.e., $\dot{R}^2$) with the pressure term in the Rayleigh–Plesset equation, the criterion for the inertial bubble collapse is obtained as $(R_{max}/R_{eq})_I = \eta_I = 2.3$ (Flynn, 1975b). This implies that if $R_{max}/R_{eq} > 2.3$, the bubble collapses inertially, and the bubble undergoes non-inertial collapse if $R_{max}/R_{eq} < 2.3$ (Leighton, 2012). Substituting the critical expansion ratio η_I into Eq. (3.34) yields the critical acoustic pressure ratio:

$$\left(\frac{p_A}{p_\infty}\right)_I = \left(\frac{3\rho_l}{2p_\infty^{2/3}}\right)^{3/5}\left(\frac{\eta_I R_{eq}}{\tau}\right)^{6/5}, \tag{3.41}$$

which implies that the bubble collapses inertially if $p_A/p_\infty > (p_A/p_\infty)_I$.

Understanding more strict criteria among those thresholds is important to predict bubble growth. Figure 3.17 shows the dependence of the Blake and inertial cavitation thresholds on critical acoustic pressure ratios. Different from the Blake threshold, the acoustic period is also a key parameter; at longer acoustic periods, smaller pressure ratios are needed for the inertial collapse. For $f = 1$ MHz, the critical pressure ratio for the inertial cavitation is smaller than that for the Blake threshold at $R_{eq} < 1\,\mu\text{m}$, such that in this regime, the bubble undergoes unstable growth and inertial collapse

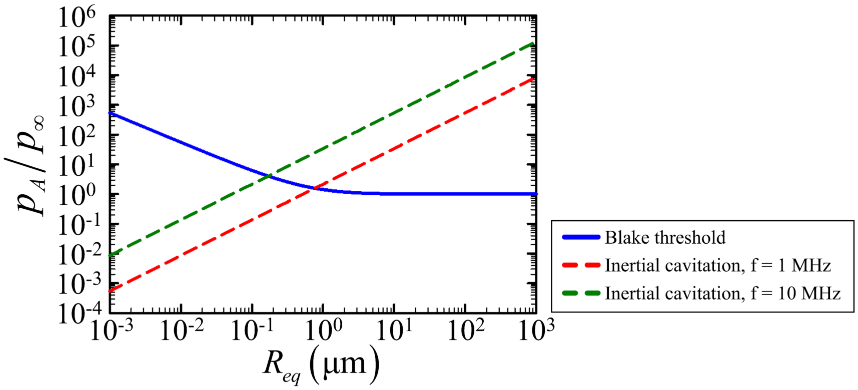

Figure 3.17: The acoustic pressure ratio for the Blake threshold and inertial cavitation threshold for f = 0.1–5 MHz as a function of equilibrium bubble radius.

at acoustic pressure ratios larger than $(p_A/p_\infty)_{Blake}$. At $R_{eq} > 1\,\mu\text{m}$, acoustic pressure ratios larger than $(p_A/p_\infty)_I$ are needed for unstable growth and inertial collapse. For f = 10 MHz, the transition for threshold criteria occurs at smaller equilibrium radius (~ 0.2 μm).

The simulations results that are deviated from the scaling relations in figures 3.14, 3.15, and 3.16 can be described by the Blake and inertial cavitation thresholds: Eqs. (3.39) and (3.41). This is because the scaling relations only well describe the explosive growth of the bubble where $p_A \gg p_\infty$ and $t_I \ll \tau$. The growth ratio of the bubble around one belongs to the regime of stable oscillation due to the low acoustic pressure ratios (~ 1) smaller than $(p_A/p_\infty)_{Blake}$, and the explosive bubble growth following the scaling relations can only be achieved under waves with higher pressure amplitudes. On the other hand, the bubble with $1 < R_{max}/R_{eq} < 2.3$ belongs to the regime of the non-inertial growth and collapse, such that the expansion ratio begins to follow the scaling relations for larger acoustic pressure ratios and longer acoustic periods.

3.5 Conclusions

In summary, we study the dependence of the bubble response and energy transport on the properties of ultrasound waveform. We propose a theoretical approach to accurately represent energy transport, considering the contributions of external forcing (e.g., ultrasound waves), thermal conduction, viscosity, and surface tension. This approach is used to build a framework to track the evolution of individual energy modes in the system. During the growth and collapse of the bubble exposed to an ultrasound wave, the energy is transferred as follows. Energy is input to the system via the ultrasound, which decreases the liquid pressure. As a result, the higher-pressure bubble expands rapidly with the surrounding liquid, which also moves outward and thus acquires kinetic energy. As the bubble expands, its pressure and velocity decrease, thereby causing liquid kinetic energy to decrease and potential energy to increase. At this point, the state of the system is the same as the initial condition of the problem described in chapter 2, in which case potential energy is converted to liquid kinetic energy, which confines the bubble, raising its pressure and thus its kinetic energy. In the final stages of the collapse, a significant fraction of the bubble internal energy is lost through acoustic radiation as bubble–wall velocities become comparable to the speed of sound. We showed that, for larger wave amplitudes, smaller frequencies, and smaller equilibrium radii, a greater amount of energy is introduced to the system via waves, such that the bubble reaches a larger maximum radius relative to the equilibrium radius; the different energy modes also increase at maximum radius, relative to the equilibrium total energy.

Assuming that most of the input energy is finally stored as liquid potential energy at maximum size, we find that the growth ratio of the bubble is determined by two dimensionless parameters; the acoustic pressure ratio and inertial-to-acoustic time ratio. We develop scaling relations for the maximum bubble radius, as well as the gas pressure and the dominant energy modes at that radius. The maximum bubble radius follows one of two scenarios; the bubble undergoes stable oscillation when the equilibrium radius is smaller than the Blake threshold radius, while inertial cavitation is observed when the equilibrium radius is smaller than the critical radius. Our scaling relations can be employed to predict the bubble radius, energy concentration, and shock emission at collapse. We also apply our framework and scaling relations to the nano-size bubble under the histotripsy waveform, which demonstrates wide applicability of our approach to diverse waveforms. The present results form the basis for better understanding of energy concentration and shock emission in non-spherical bubble collapse. The effects of vapor inside the bubble are expected to affect the energy transfer in other regimes. For future work, we plan to extend our framework to describe energy transfer for the gas/vapor mixture bubble. Furthermore, the present results for a bubble in water would provide guidelines to understand energy transfer during bubble oscillation in biological material.

CHAPTER 4

Effects of Compressibility on Bubble Dynamics during the Collapse of a Cavitation Bubble Near a Rigid Boundary

Cavitation-bubble collapse is known to cause structural damage in a variety of industrial applications such as naval hydrodynamics and turbomachinery. When cavitation bubbles are subjected to high-pressure regions, they undergo a rapid compression that concentrates energy into a small volume. As the bubble rebounds, a high-amplitude pressure (or shock) wave is generated, propagating radially outward and subsequently producing impact loads on the nearby objects. In addition, when a bubble collapses near a boundary, asymmetrical surroundings causes the bubble to collapse non-spherically. The concentration of energy and shock emission during non-spherical collapse is expected to depend on the liquid compressibility. Thus, a better understanding of role of compressibility is essential to predicting cavitation erosion. In this study, we compare direct simulations to potential flow calculations to assess the effects of compressibility on the collapse of a gas bubble near a rigid boundary. The 3D compressible Navier-Stokes are solved in the gas and liquid using a high-order shock- and interface-capturing scheme; potential calculations are conducted using a boundary integral method. We observe a delay between the two approaches, attributed to the differences in the pressure fields at early times due to compressibility effects. Nevertheless, bubble morphologies are similar for the most part of collapse, with discrepancies visible only in the final stages of collapse. We discuss the effects of compressibility on the dynamics of the bubble and jet at jet impact. This understanding will help better understand the importance of waves generating during the collapse and will inform efforts to develop a better relation to predict shock properties.

4.1 Introduction

Cavitation is the process whereby vapor bubbles are formed due to the reduction of local pressure in a liquid. When the bubbles are subjected to high pressure regions, they undergo a rapid compression, which concentrates energy into a small volume. Subsequently, at collapse, some of the energy inside the bubble is released through shock waves, propagating outward and impinging upon neighboring boundaries, thus producing an impact load. The destructive nature of inertial cavitation plays a critical role in determining the sustainability of a system in a variety of applications, including naval hydrodynamics (Knapp *et al.*, 1970; Plesset & Prosperetti, 1977), turbomachinery (Arndt, 1981), and the Spallation Neutron Source (SNS) (Riemer *et al.*, 2014; Winder *et al.*, 2020). However, inertial cavitation has recently been exploited for therapeutic and diagnostic ultrasound treatment, including histotripsy (Parsons *et al.*, 2006; Khokhlova *et al.*, 2015), lithotripsy (Zhong, 2013), contrast-enhanced ultrasound (Patterson *et al.*, 2012; Versluis *et al.*, 2020), and targeted drug delivery to the brain (McDannold *et al.*, 2006; Tung *et al.*, 2010).

In an infinite sea of liquid, which is perfectly symmetrical, the bubble collapses spherically. However, the presence of the nearby object breaks the symmetry and causes the bubble to collapse in non-spherical fashion, which is often observed in aforementioned applications (Plesset & Prosperetti, 1977; Arndt, 1981; Tomita & Shima, 1986). During the collapse, a high-speed re-entrant jet is formed in the direction of the boundary, piercing the bubble. When the re-entrant jet impacts the opposite side of the bubble wall, a water-hammer shock wave is produced (Tomita & Shima, 1986; Philipp & Lauterborn, 1998). Furthermore, as the bubble reaches its minimum volume and subsequently rebounds, an implosion shock wave is produced. These shock waves propagate outward, resulting in high pressures on neighboring boundaries (Lindau & Lauterborn, 2003; Johnsen & Colonius, 2009). Thus, it is essential to understand the dynamics of a bubble collapsing near a solid surface and of the re-entrant jet to build a predictive model for the impact loads induced by shock waves.

During the process of inertial collapse, liquid compressibility has significant effects on bubble dynamics and jet formation. In the early stages of collapse, due to the initial pressure difference, a rarefaction wave propagates outward. As the waves interact with a nearby boundary, they are reflected with negligible attenuation due to the large impedance mismatch between the boundary and liquid. The reflected waves interact with the collapsing bubble and change nearby pressure fields. On the other hand, in the incompressible limit, the bubble would instantaneously be made aware of the nearby boundary. It is clear that pressure fields would be significantly different in the compressible and incompressible cases. Thus, the overall bubble and jet dynamics are expected to depend significantly on liquid compressibility.

Liquid compressibility may explain discrepancies between different past studies (Naudé & Ellis, 1961; Tomita & Shima, 1986; Blake *et al.*, 1986; Vogel *et al.*, 1989; Philipp & Lauterborn, 1998; Supponen *et al.*, 2016). In past studies, different relationships have been proposed to describe jet velocity, which is one of the key quantities for estimating water-hammer shock pressure. For investigation of bubble collapse, Naudé & Ellis (1961) employed the potential flow theory, which neglected liquid compressibility and determined that the maximum jet velocity is 50–76 m/s and the corresponding maximum peak pressure along the boundary is 0.1–10 MPa. Tomita & Shima (1986) experimentally studied bubble collapse at high driving pressures, where liquid compressibility cannot be ignored. They showed that the maximum jet velocity ranges from 30 to 120 m/s and the corresponding maximum peak pressure ranges from 2 to 10 MPa. Blake & Gibson (1987) empirically found scaling relations to describe the jet velocity as a function of driving pressure. Supponen *et al.* (2016) conducted experiments and proposed scaling relations to universally explain the maximum jet velocity observed in the collapse of a bubble near a boundary and a free surface, and of a bubble under the action of gravity. However, their relations are based on potential flow theory, only valid at low driving pressures where liquid compressibility is negligible. As shown in these studies, liquid compressibility adds great complexity to building a more comprehensive, predictive model for the dynamics of bubble and jet. Thus, a better understanding of the effect of liquid compressibility is required to achieve this goal.

The objective of this work is to understand the effects of liquid compressibility on bubble and

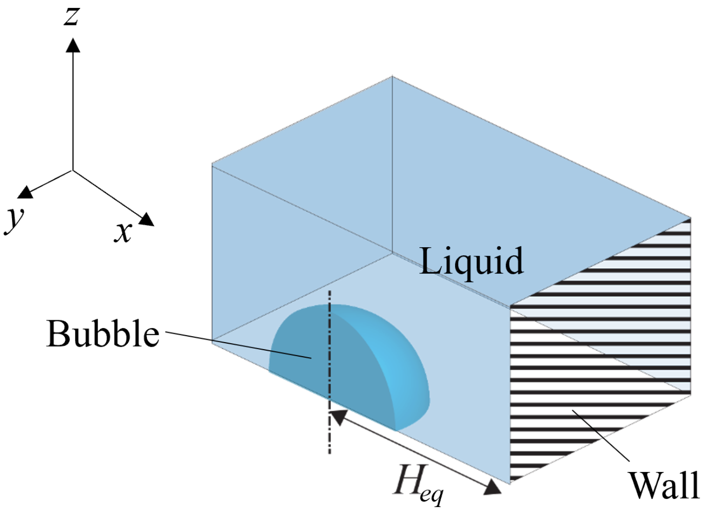

Figure 4.1: Schematics of the Rayleigh collapse of a bubble near a rigid boundary.

jet dynamics. For this purpose, we compare compressible flow simulations to potential flow results to assess the contributions of compressibility to bubble collapse. The article is organized as follows. First, numerical methods for compressible flow simulations and potential flow calculations are introduced in section 4.2. In section 4.3, both approaches are used to quantify the effects of compressibility on the bubble and jet dynamics (i) during the collapse and (ii) at jet impact. This article ends with concluding remarks in section 4.4.

4.2 Physical and numerical models

4.2.1 Problem description

We investigate the classical Rayleigh collapse (Rayleigh, 1917) of an isolated bubble in water near a rigid boundary. Initially, a spherical gas bubble of radius R_{eq} = 500 µm at pressure p_{eq} = 3.55 kPa and temperature T_{eq} = 300 K is in mechanical and thermal equilibrium with the surrounding water. The bubble centroid is located a distance H_{eq} from a rigid wall. In the direct simulation, the domain size is typically $10 \times 6 \times 6$ to make sure that the initial distance between the domain boundary and the bubble centroid is larger than 6. The problem symmetry is leveraged such that one fourth of the domain is considered by applying symmetry boundary conditions along the xz and xy planes. Non-reflecting conditions are applied along the remaining planes. A no-slip wall condition is applied along the yz plane. In the following sections, we investigate the dependence of the bubble and jet dynamics on the driving pressure ratio $\Delta p/p_{eq}$, the effective Mach number $M = \sqrt{\Delta p/\rho_l a_l^2}$ and the normalized initial stand-off distance δ_{eq}. The range of these parameters are $\Delta p/p_{eq} = 1.4-2.8\times10^3$, $M = 3.3-6.6\times10^{-2}$ and $\delta_{eq} = 1.25-5.00$. The driving pressure range is relevant to inertial collapse of acoustically generated bubble as well as underwater explosions (Cole, 1948; Hunter & Geers, 2004). Bubble collapse from maximum bubble volume to jet impact is our interest in the present study; the bubble dynamics after jet impact will be discussed in a subsequent study.

4.2.2 Numerical simulations for compressible multiphase flows

We numerically solve the three-dimensional compressible Navier-Stokes (NS) equations for a gas-liquid system consisting of mass conservation, momentum and energy balance equations:

$$\frac{\partial \rho}{\partial t} + \frac{\partial}{\partial x_j}(\rho u_j) = 0, \tag{4.1a}$$

$$\frac{\partial \rho u_i}{\partial t} + \frac{\partial}{\partial x_j}(\rho u_i u_j + p\delta_{ij}) = \frac{\partial \tau_{ij}}{\partial x_j}, \tag{4.1b}$$

$$\frac{\partial E}{\partial t} + \frac{\partial}{\partial x_j}[u_j(E + p)] = \frac{\partial}{\partial x_j}(u_i\tau_{ij} - Q_j), \tag{4.1c}$$

where ρ is the density, t is the time, u_i is the velocity vector, p is the pressure, δ_{ij} is the identity tensor, τ_{ij} is the viscous stress tensor, x_j is the spatial vector in the Cartesian coordinate, E is the total energy per unit volume, Q_j is the heat flux, and i, j = 1, 2, and 3. The total energy E per unit volume comprises the internal and kinetic energy:

$$E = \rho e + \frac{1}{2}\rho u_i^2, \tag{4.2}$$

where e is the internal energy per unit mass. The viscous stress tensor and heat flux are expressed as follows:

$$\tau_{ij} = \mu\left(\frac{\partial u_i}{\partial x_j} + \frac{\partial u_j}{\partial x_i} - \frac{2}{3}\frac{\partial u_k}{\partial x_k}\delta_{ij}\right) + \mu_B \frac{\partial u_k}{\partial x_k}\delta_{ij}, \tag{4.3a}$$

$$Q_j = -\kappa \frac{\partial T}{\partial x_j}, \tag{4.3b}$$

where μ is the dynamics shear viscosity, μ_B is the bulk viscosity, and κ is the heat conductivity. For a micro-to-millimeter size bubble, the Reynolds number $O(10^3 - 10^5)$ and Weber number $O(10^1 - 10^5)$ are sufficiently large, such that the inertial effects dominates the bubble collapse, and viscous and surface tension effects can be ignored. (Johnsen & Colonius, 2009; Tiwari *et al.*, 2015; Beig *et al.*, 2018; Trummler *et al.*, 2020).

To capture gas/liquid interfaces, additional transport equations for volume fraction are solved (Murrone & Guillard, 2005; Beig & Johnsen, 2015; Saurel & Pantano, 2018):

$$\frac{\partial}{\partial t}(\rho^{(k)}\alpha^{(k)}) + \frac{\partial}{\partial x_j}\left(\rho^{(k)}\alpha^{(k)}u_j\right) = 0, \tag{4.4a}$$

$$\frac{\partial \alpha^{(k)}}{\partial t} + u_j \frac{\partial \alpha^{(k)}}{\partial x_j} = \Gamma^{(k)}\frac{\partial u_j}{\partial x_j}, \tag{4.4b}$$

where

$$\Gamma^{(k)} = \frac{\alpha^{(k)}}{K_s^{(k)}}\left(\frac{1}{\sum_l \frac{\alpha^{(l)}}{K_s^{(l)}}} - K_s^{(k)}\right), \qquad K_s^{(k)} = \rho^{(k)}(a^{(k)})^2, \tag{4.5}$$

where k represents phases, and $k = 1$ and 2. In this multifluid modeling, the volume fraction approach prevents generation of spurious oscillations in pressure and temperature across the material discontinuities Beig & Johnsen (2015).

To close the system and relate the internal energy to pressure and temperature, the Noble-Abel

Stiffened-Gas (NASG) equation of state (EOS) (Métayer & Saurel, 2017) is used:

$$\rho e = \frac{p}{n-1}(1-\rho b) + \frac{nB}{n-1}(1-\rho b) + \rho q, \tag{4.6a}$$

$$= \rho c T + B(1-\rho b) + \rho q, \tag{4.6b}$$

where b, B, n, q, and c are parameters, depending on the materials. For water vapor and liquid water, the coefficients introduced in Table 4.1 produces a good fit to experimental data (Métayer & Saurel, 2017). Using this EOS, the pressure and temperature can be obtained:

$$p = \left[\rho e - \sum_k \alpha^{(k)} \left(\frac{nB}{n-1}\right)^{(k)} + \sum_k (\rho\alpha)^{(k)} \left(\frac{nBb}{n-1}\right)^{(k)} - \sum_k (\rho\alpha)^{(k)} q^{(k)}\right] \Bigg/ \left[\alpha^{(k)} \left(\frac{1}{n-1}\right)^{(k)} - \sum_k (\rho\alpha)^{(k)} \left(\frac{b}{n-1}\right)^{(k)}\right] \tag{4.7}$$

$$T = \left[\rho e - \sum_k \alpha^{(k)} B^{(k)} + \sum_k (\rho\alpha)^{(k)} (bB)^{(k)} - \sum_k (\rho\alpha)^{(k)} q^{(k)}\right] \Bigg/ \sum_k (\rho\alpha)^{(k)} c^{(k)}, \tag{4.8}$$

where $(\rho\alpha)^{(k)}$ is calculated from the conservative from of the volume fraction transport equation (4.4a) and $\alpha^{(k)}$ is calculated from the non-conservative form of the volume fraction transport equation (4.4b). The speed of sound in gas/liquid mixture follows the Wood's formula (Wood, 1930)

$$\frac{1}{\rho a^2} = \sum_k \frac{\alpha^{(k)}}{\rho^{(k)} (a^{(k)})^2}, \tag{4.9}$$

where $a^{(k)}$ is the speed of sound for k component. The NASG–EOS is used to express this equation

Table 4.1: Coefficients in the NASG–EOS for water vapor and liquid water.

Coefficients	Water vapor	Liquid water
n	1.47	1.19
b (m^3/kg)	0	6.61×10^{-4}
B (MPa)	0	702.8
c (J/kg-K)	955	3610
q (J/kg)	2.077×10^6	-1.177×10^6

as the mixture form:

$$a^2 = \frac{n(p+B)}{\rho(1-\rho b)}. \tag{4.10}$$

The physical models described in this section is numerically implemented to an in-house code to simulate cavitation bubble collapse. For spatial discretization of Eqs. (4.1) and (4.4), a solution-adaptive high-order accurate finite difference scheme is used to approximate advection fluxes while appropriately capturing discontinuities (Movahed & Johnsen, 2013; Beig & Johnsen, 2015). A sensor is used to detect the discontinuities (i.e., interface, contacts, shocks) (Henry de Frahan *et al.*, 2015). For smooth regions, a fourth-order central difference scheme is used, while for discontinuous regions, a fifth-order weighted essentially non-oscillatory (WENO) reconstruction (Jiang & Shu, 1996) and the Harten-Lax-van Leer (HLL) (Harten *et al.*, 1983) Riemann solver is used. For the diffusive terms, a fourth-order explicit central difference scheme is used. For time marching, a third-order accurate explicit strong-stability-preserving Runge-Kutta scheme (Gottlieb & Shu, 1996) is used, and the time step size is controlled adaptively by the advection and diffusion constraints. The high-order solution-adaptive techniques may prevent interfaces being overly smeared (Beig, 2018). The code leverages Message Passing Interface (MPI) to accelerate the computation, and parallel Hierarchical Data Format (HDF5) is used to efficiently manage extremely large data sets (Beig, 2018).

The convergence of our in-house code for spherical bubble collapse is demonstrated in Beig (2018). Comparing the minimum bubble volume at collapse in the simulations to the solution of the Keller–Miksis equation (Keller & Miksis, 1980), Beig (2018) showed that the resolution with 192 cells per initial bubble radius represents the dynamics with sufficient accuracy to inform physics, so this is also used in the present study. This result also means that the interface smeared over a number of cells has negligible effects on the bubble dynamics.

4.2.3 Potential flow theory for collapse of a bubble in a liquid

To examine the role of compressibility in the context of collapse of a cavitation bubble, we consider a framework for potential flow calculations using the Boundary Integral Method (BIM) (Blake *et al.*, 1986). For incompressible, inviscid, and irrotational flows, there exists a velocity potential ϕ satisfying Laplace's equation:

$$\nabla^2 \phi = 0, \tag{4.11}$$

obtained from the continuity equation for the liquid domain Ω. By Green's theorem, a solution of equation (4.11) also satisfies the following integral equation:

$$c(\mathbf{p})\phi(\mathbf{p}) = \int_{\partial\Omega} \left(\frac{\partial \phi(\mathbf{q})}{\partial n} G(\mathbf{p},\mathbf{q}) - \phi(\mathbf{q}) \frac{\partial G(\mathbf{p},\mathbf{q})}{\partial n} \right) dS, \tag{4.12}$$

where the point $\mathbf{p} \in \Omega + \partial\Omega$, the point $\mathbf{q} \in \partial\Omega$, ∂n is the normal derivative, and S is the surface integral. The coefficient $c(\mathbf{p})$ is 4π if $\mathbf{p} \in \Omega$ and 2π if $\mathbf{p} \in \partial\Omega$. The three-dimensional Green's function G($\mathbf{p}$,$\mathbf{q}$) is

$$G(\mathbf{p},\mathbf{q}) = \frac{1}{|\mathbf{p}-\mathbf{q}|} + \frac{1}{|\mathbf{p}-\mathbf{q}'|}, \tag{4.13}$$

where the point $\mathbf{q}'$ is the image of $\mathbf{q}$ reflected with respect to the rigid wall. The momentum balance equation can be simplified as the unsteady Bernoulli equation:

$$\frac{D\phi}{Dt} = \frac{|\mathbf{u}|^2}{2} + \frac{(p_{eq} + \Delta p) - p_b}{\rho_l}, \tag{4.14}$$

where p_{eq} is the equilibrium gas pressure, Δp is the driving pressure, and p_b is the gas pressure, ρ_l and $\mathbf{u}$ are the liquid density and velocity. The bubble wall is advected, following the liquid velocity at the wall:

$$\frac{d\mathbf{x}}{dt} = \nabla\phi, \tag{4.15}$$

where the point $\mathbf{x} \in \partial\Omega$. In figure 4.2, the bubble wall is discretized into $n + 1$ Lagrangian nodes and n segments in axisymmetric coordinates, and each segment and variable along the bubble wall

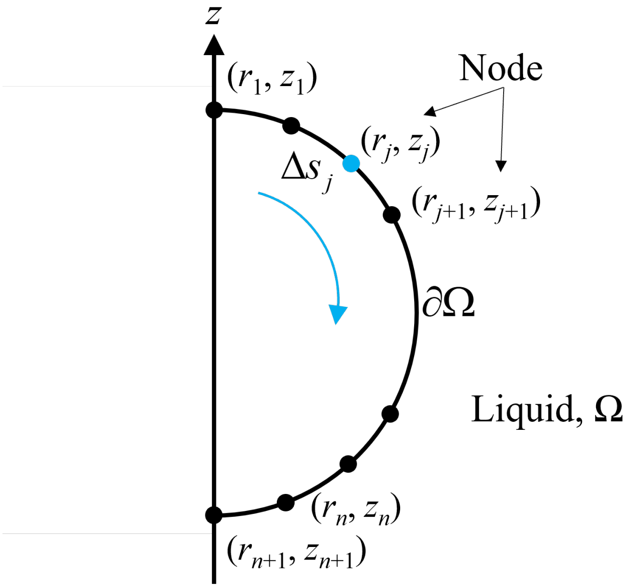

Figure 4.2: Schematic and discretization of the bubble wall for implementation of the Boundary Integral Method.

is represented by cubic splines. Since the gradient in the radial direction at $r = 0$ should be zero for $\phi(s)$ and $z(s)$, a clamped spline is used to enforce zero gradient boundary conditions at the first and $(n+1)^{th}$ node. In addition, the second derivative of $r(s)$ should be zero at $r = 0$, and the natural spline is used to enforce this boundary condition.

Following this discretization, equation (4.12) can be expressed as

$$\begin{aligned} 2\pi\phi(p_i) = \sum_{j=1}^{n} \int_{s_j}^{s_{j+1}} \frac{\partial\phi(q_j)}{\partial n} \left(\int_0^{2\pi} G\left(p_i, q_j\right) d\theta \right) r(s) ds \\ - \sum_{j=1}^{n} \int_{s_j}^{s_{j+1}} \phi(q_j) \left(\int_0^{2\pi} \frac{\partial G\left(p_i, q_j\right)}{\partial n} d\theta \right) r(s) ds, \end{aligned} \tag{4.16}$$

where p_i and q_j are the j^{th} node at $\partial\Omega$, s_j is the arc length from the reference point (r_1,z_1) to j^{th} node (r_j,z_j), r is the paramter in the radial direction, θ is the parameter in the azimuthal direction, and s is the parameter for the surface integral. This integral equation can be rewritten:

$$2\pi\phi(p_i) + \sum_{j=1}^{n} A_{ij} = \sum_{j=1}^{n} \left(B_{ij}\psi_j + C_{ij}\psi_{j+1} \right), \tag{4.17}$$

where ψ_j is the normal velocity at node j, and $\psi_j = (\partial\phi/\partial n)_j$. The matrices for segment j with respect to node i, A_{ij}, B_{ij}, and C_{ij} are given by

$$A_{ij} = \int_{s_j}^{s_{j+1}} \phi(q_j)\beta_{ij}(s)ds, \tag{4.18a}$$

$$B_{ij} = \int_{s_j}^{s_{j+1}} \left(\frac{s_{j+1} - s}{s_{j+1} - s_j}\right)\alpha_{ij}(s)ds, \tag{4.18b}$$

$$C_{ij} = \int_{s_j}^{s_{j+1}} \left(\frac{s - s_j}{s_{j+1} - s_j}\right)\alpha_{ij}(s)ds, \tag{4.18c}$$

where $\beta_{ij}(s)$ and $\alpha_{ij}(s)$ are the integration term in the azimuthal direction, multiplied by $r(s)$. A 10-points Gauss quadrature is used to compute the integration terms with complete elliptic integrals of the first and second kind (Blake *et al.*, 1986; Best, 1993). To treat the singularities at the leftmost and rightmost points of the segment, logarithmic terms in the integration (4.18) are decomposed into singular and non-singular terms:

$$\log(1 - k_j^2) = \log\left[\frac{1 - k_j^2}{((s_{j+1} - s)/\Delta s_j)^2}\right] + 2\log\left(\frac{s_{j+1} - s}{\Delta s_j}\right), \tag{4.19}$$

where the left term is the non-singular term, the right term is the singular term, and k_j is given by

$$k_j^2 = \frac{4r_j r_i}{(r_j + r_i)^2 + (z_j - z_i)^2}. \tag{4.20}$$

For the singular term, the 10-points Stroud quadrature is used (Stroud, 1966).

The velocity in the normal direction, $\partial\phi/\partial n$ is computed using Eq. (4.16). Then, for given velocity potential, the tangential velocity is obtained using a fourth-order central difference scheme on non-uniform grids. After the total velocity is computed, ϕ at each node i is marched forward in time by a time step with adaptive size (Blake *et al.*, 1986):

$$\Delta t = \frac{\Delta t_{max}}{\max\left[|1 - p_b| + (1/2)|\mathbf{u}|^2\right]}, \tag{4.21}$$

which is in accordance with the Courant−Friedrichs−Lewy (CFL) condition to limit the rapid increment in the velocity potential and to capture a violent change in bubble dynamics with $\Delta t_{max} = 0.001$ (Best, 1993; Pearson *et al.*, 2004). At each time step, the nodes on the bubble surface are redistributed with the same arc length to prevent numerical instabilities (Best, 1993; Pearson *et al.*, 2004). The five-point smoothing formula of Longuet-Higgins & Cokelet (1976) is also implemented to suppress these instabilities at every 200 time steps (Best, 1993; Lind, 2014).

4.3 Results

4.3.1 Effects of compressibility on bubble dynamics during the collapse

To qualitatively describe the effects of compressibility on the bubble dynamics, we first observe the bubble morphology and pressure fields. Figures 4.3 and 4.4 show (i) contours for the pressure and density gradient (i.e., bubble shape) fields during the collapse in the direct simulations at the left column and (ii) bubble shapes and surrounding pressure fields during bubble collapse at different times for the compressible and potential flow cases. As the bubble begins to collapse, overall the pressure in the liquid decreases over time. As the bubble collapses more, due to asymmetrical surroundings, a re-entrant jet is formed in the direction of the wall, piercing the bubble, and a water-hammer shock wave is produced when the jet impacts the opposite side of the bubble surface.

At the beginning of the collapse, both cases show the same bubble shape, even though the pressure fields are significantly different. At this stage, in the compressible case, the initially generated rarefaction waves propagating radially outward have not hit the neighboring wall yet, such that the liquid pressure remains unaffected by the presence of the wall. On the other hand, in the potential flow case, the bubble instantaneously knows about the presence of the nearby wall, and thus the pressure fields adjust accordingly, as shown in figure 4.3(a). In the compressible case, after the passage of initially generated rarefaction waves, which are reflected off the rigid wall, the pressure fields in both cases become similar, as shown in figure 4.3(b).

This difference between the compressible and potential flow cases in the early stages of collapse causes large discrepancies in the later stages of collapse. Figure 4.4 shows the bubble shapes and

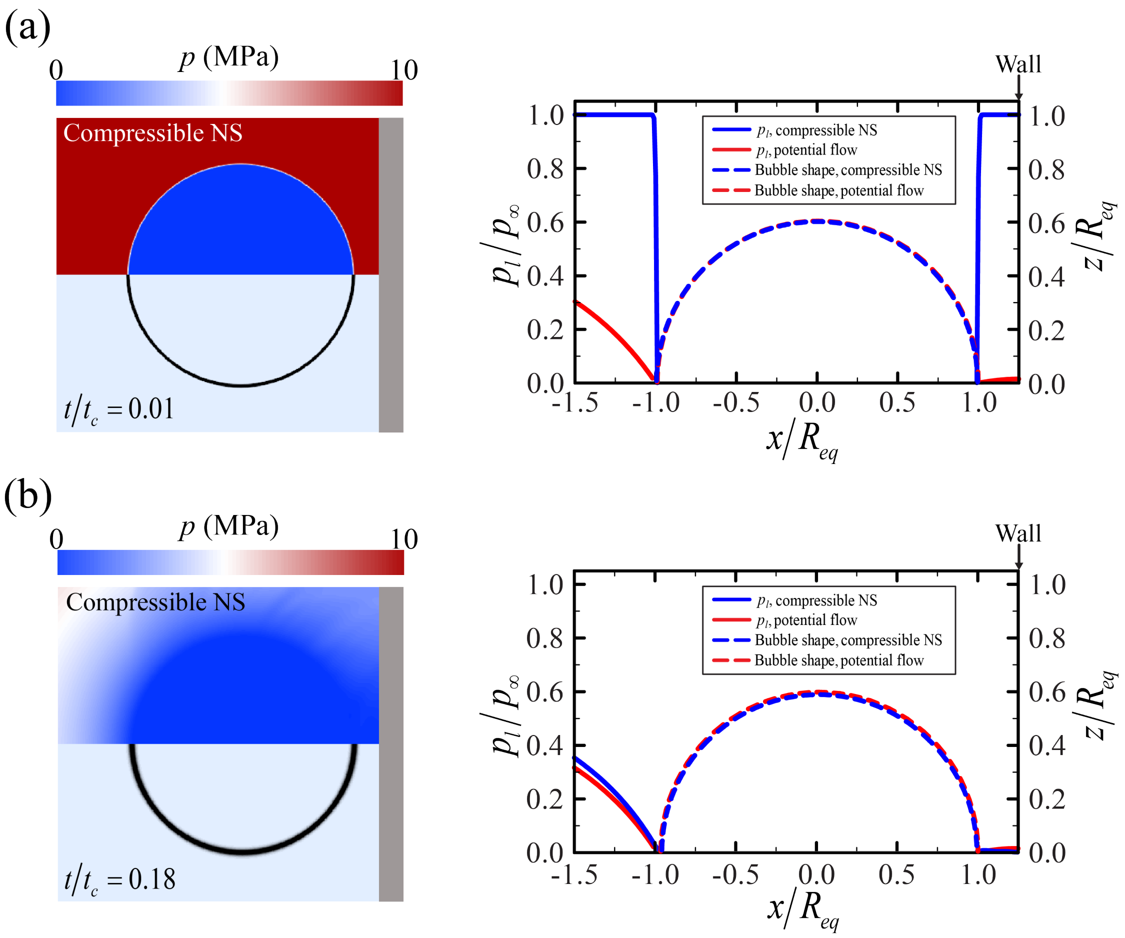

Figure 4.3: Bubble shapes and surrounding pressure fields for the compressible and potential flow simulations at t/t_c = (a) 0.01 and (b) 0.18 for $\delta_{eq} = 1.25$. Left column: central cross section of pressure and density gradient contours for the direct simulations. Right column: pressure field along the axis across the bubble centroid and bubble shape along the central cross section. Time is normalized by the Rayleigh collapse time $t_c = 0.915R_{eq}\sqrt{\rho_l/\Delta p}$

surrounding pressure fields at late and in the final stages of the collapse. In the compressible case, the bubble is exposed to a higher pressure over a longer period of time, compared to the potential flow case. As a result, the bubble compresses to a greater extent and collapses more rapidly in the compressible case. At $t/t_c = 0.86$, the bubble in the compressible case is smaller than that in the potential flow case, as shown in figure 4.4(a). As the bubble collapses further, the discrepancies in bubble shape and near-field pressure field become more significant, such that the formation of a re-entrant jet is observed in the compressible case, which is not yet observed in the potential flow case (see figure 4.4(b)). Thus, jet impact occurs in the compressible case at $t/t_c = 1.10$, while a jet

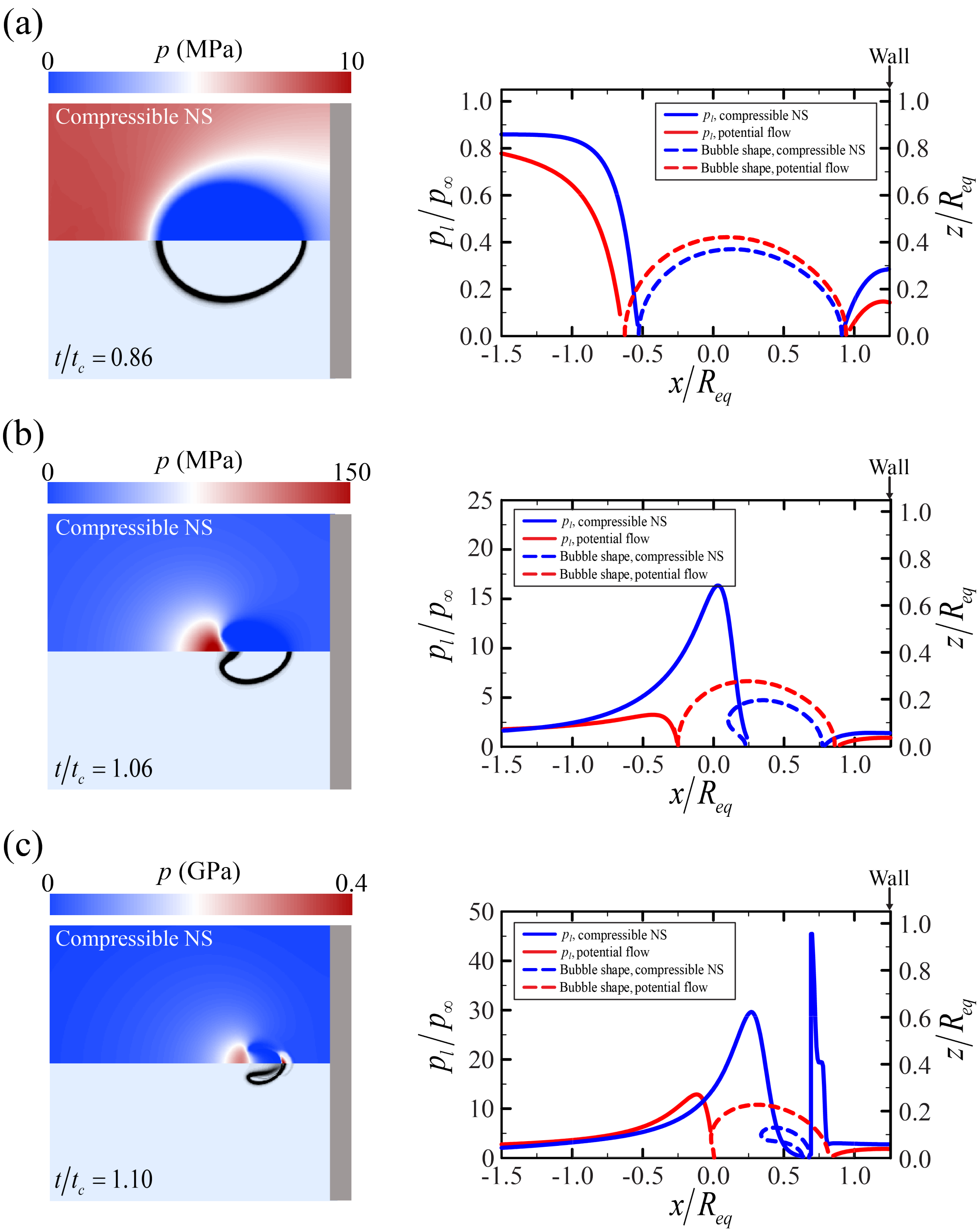

Figure 4.4: Bubble shapes and surrounding pressure fields for the compressible and potential flow cases at t/t_c = (a) 0.86, (b) 1.06, and (c) 1.10 for $\delta_{eq} = 1.25$. Left column: central cross section of pressure and density gradient contours for the compressible case. Right column: pressure field along the axis across the bubble centroid and bubble shape along the central cross section. Time is normalized by the Rayleigh collapse time $t_c = 0.915 R_{eq} \sqrt{\rho_l/\Delta p}$.

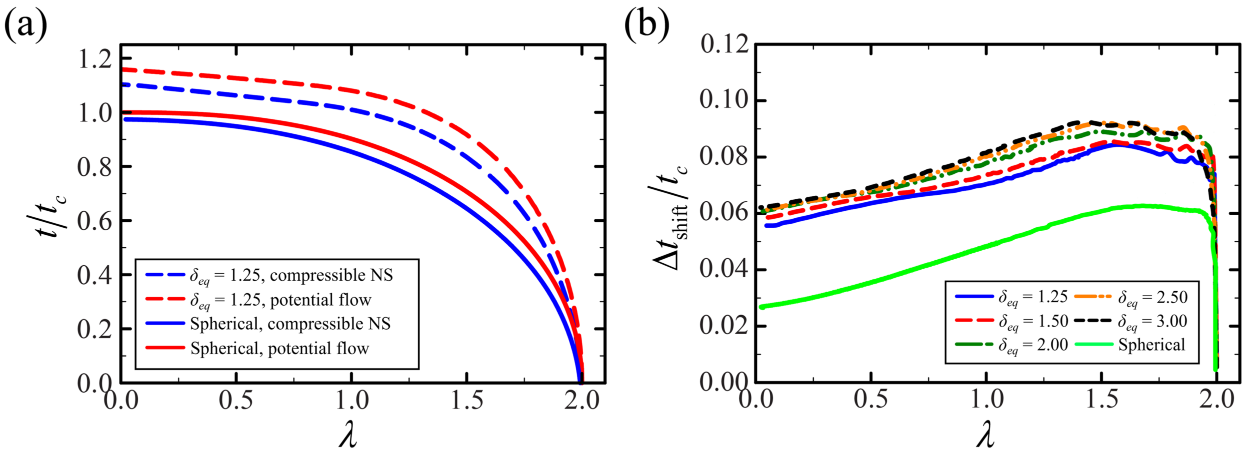

Figure 4.5: (a) Time as a function of jet thickness normalized by the initial radius for non-spherical ($\delta_{eq} = 1.25$) and spherical ($\delta_{eq} = \infty$) collapse for the compressible and potential flow case. (b) Time shift as a function of jet thickness for different distances $\delta_{eq} = 1.25 - 3.00, \infty$.

only begins to appear in the potential flow case at the same time, as shown in figure 4.4(c).

To appropriately compare time differences during the collapse for the compressible and potential flow cases, figure 4.5 shows the normalized time and the time shift as a function of normalized jet thickness for non-spherical collapse; as a comparison, spherical collapse is also considered. Here, jet thickness λ is the distance along the x axis between the points at the bubble surface, normalized by the equilibrium radius, such that it changes from 2 to 0. For spherical and non-spherical collapse, the bubble in the compressible case collapses faster than the bubble in the potential flow case. We also compute the time difference Δt_{shift} between the instants when both compressible and potential flow simulations yield the same jet thickness. As shown in figure 4.5, the time shift is more pronounced in the early stages of collapse due to the greater difference in the liquid pressure fields, and it decreases as the collapse proceeds. As the initial stand-off distance is increased, the initially emitted rarefaction wave takes a longer time to propagate to the wall and reflect back to the bubble, such that the time shift increases. However, when the bubble collapses infinitely far from the wall, the near-field pressure fields in the compressible case are qualitatively similar to those obtained in the potential flow case at earlier time because the near-field pressure fields are not affected by the reflected waves.

To make meaningful comparisons, figure 4.6 compares the bubble morphologies during the

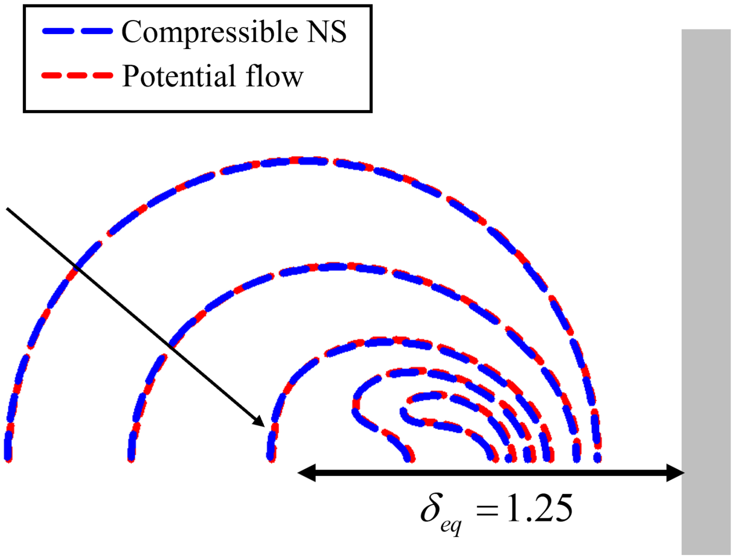

Figure 4.6: Bubble morphologies during bubble collapse for the compressible and potential flow simulations; δ_{eq} =1.25 and p_∞/p_{eq} = 2800.

collapse for both compressible and potential flow cases for a given jet thickness, such that each case has the same jet thickness at different times. Interestingly, when both cases have the same jet thickness, the bubble morphologies are similar during most of the collapse. Apart from the time shift, the bubble shows similar kinematics throughout the collapse for both compressible and potential flow cases. Figure 4.7 shows the normalized bubble displacement d/R_{eq} and collapse non-sphericity η for different initial stand-off distances for compressible and potential flow simulations. Here the collapse non-sphericity is calculated as $\eta = 1 - \pi\lambda/P$, where P is the perimeter of the toroidal bubble in the centerplane (Beig *et al.*, 2018). For most of the collapse, the bubble displacement and the collapse non-sphericity are almost identical in the compressible and potential flow cases. However, slight discrepancies are observed between the two cases in the final stages of collapse (small jet thicknesses), where the liquid compressibility effects are no longer negligible.

4.3.2 Bubble dynamics at jet impact

As described earlier, in non-spherical collapse, a water-hammer shock wave is produced at jet impact, propagating outward and leading to impact loads on a nearby wall. Emission of the water-hammer shock wave relies on the bubble dynamics at jet impact, which are significantly affected by

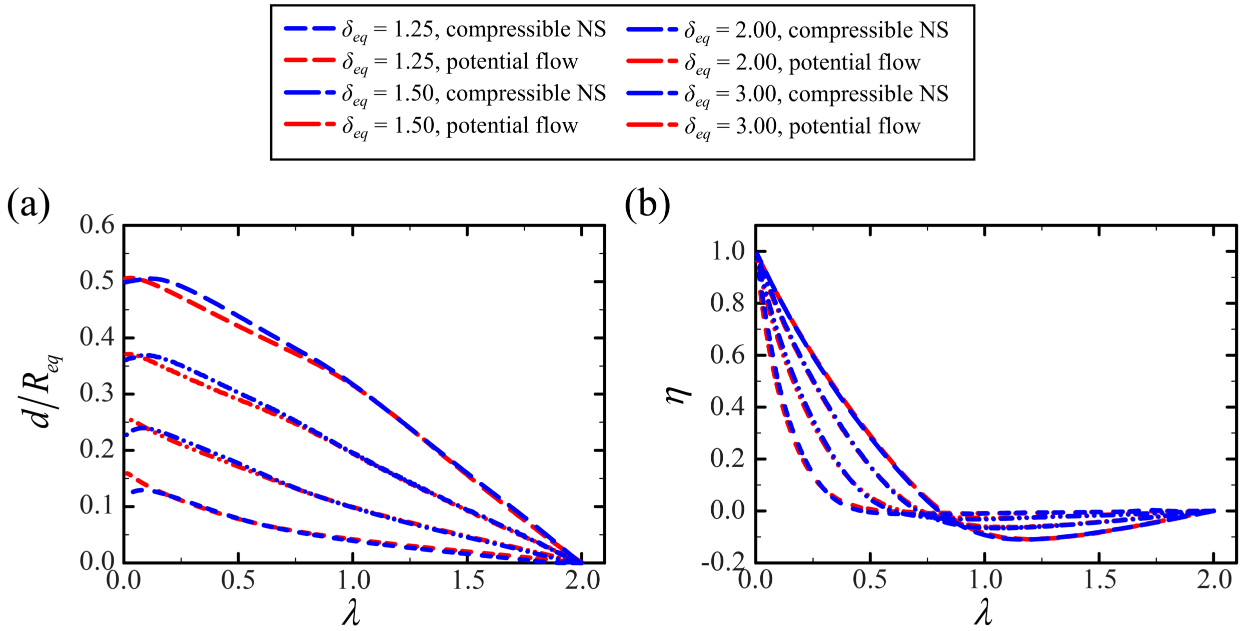

Figure 4.7: (a) Bubble displacement and (b) non-sphericity as a function of jet thickness for the compressible and potential flow simulations for different distances δ_{eq} = 1.25–3.00, and p_∞/p_{eq} = 2800.

liquid compressibility. Thus, to develop a model to predict the dynamics of a water-hammer shock wave, a better understanding of the dependence of the bubble dynamics at jet impact on liquid compressibility is required. Figure 4.8 shows the normalized time t_{imp}, bubble volume V_{imp}, bubble displacement d_{imp} and jet velocity V_{jet} at jet impact as a function of initial stand-off distance for both compressible and potential flow simulations. The jet impact time demonstrates the duration of jet formation during the collapse. For all cases, the normalized jet impact time decreases as the initial stand-off distance increases. For smaller initial stand-off distances, bubble collapse becomes more non-spherical, leading to longer jet impact times. Furthermore, in the potential flow simulations, the normalized jet impact time is very similar for different driving pressure ratios. In the potential flow cases, the driving pressure ratios are already high enough, such that the bubble collapse tends to be collapse of an empty bubble (i.e., no gas inside the bubble); normalized jet impact time can be scaled analytically as a function of δ_{eq} (Plesset & Chapman, 1971). However, in the compressible cases, the jet impact time is delayed at low driving pressure ratios, where the compressibility is less important. In addition, as explained in section , in the compressible cases,

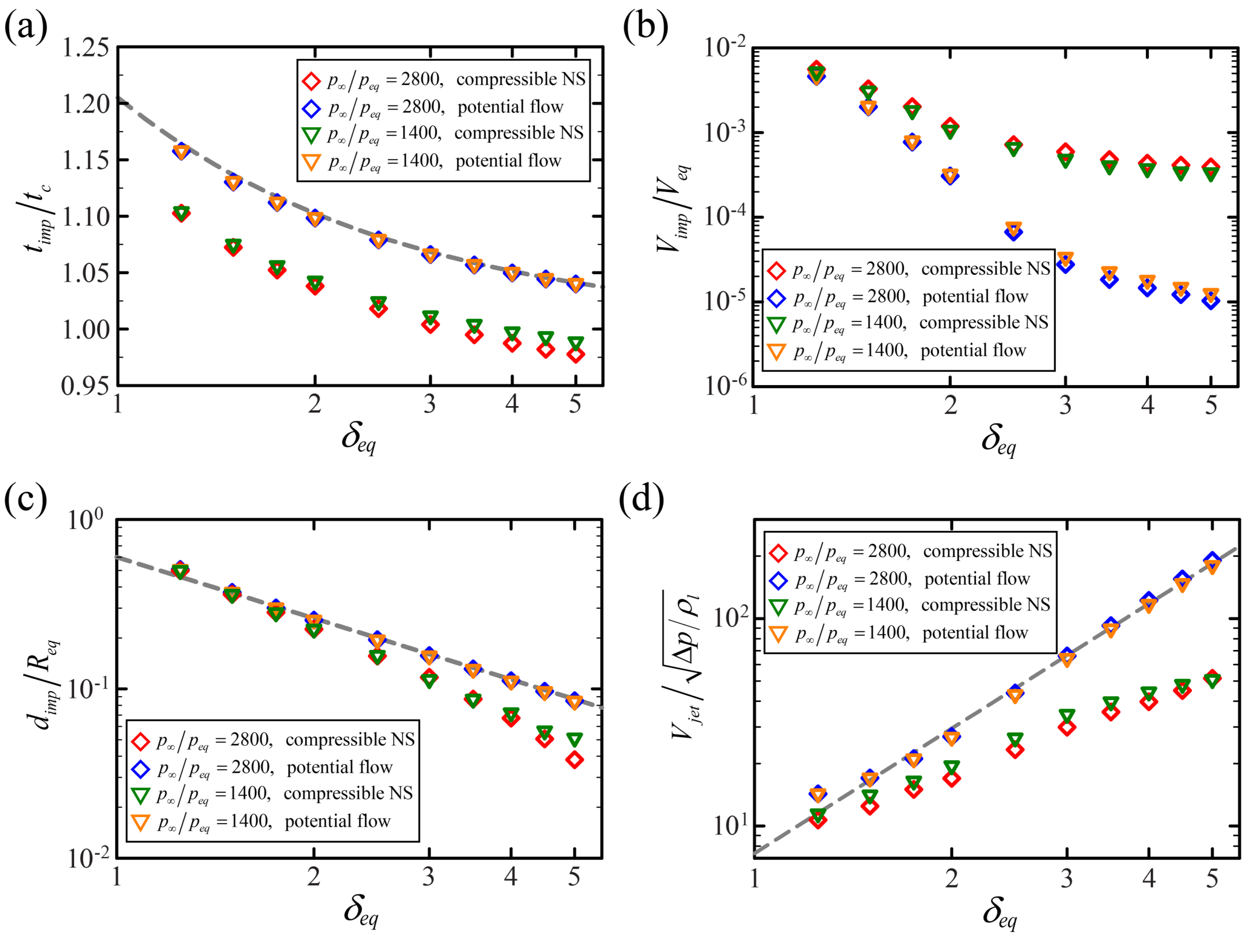

Figure 4.8: (a) Time, (b) bubble volume, (c) bubble displacement, and (d) jet velocity at jet impact for different distances δ_{eq} = 1.25–5 and p_∞/p_{eq} = 1400, 2800; gray dashed line: (a) $1+0.205/\delta_{eq}$ (Plesset & Prosperetti, 1977), (c) slope: -1.2, and (d) slope: +2 (Supponen *et al.*, 2016).

the bubble is exposed to a high pressure over a longer period of time, leading to short jet impact time, compared to the potential flow cases.

The bubble volume at jet impact is one of the important parameters to estimate the implosion shock produced at collapse. For all cases, the normalized bubble volume at jet impact reduces as the initial stand-off distance increases. If the bubble is initially located closer to the wall, the collapse becomes more non-spherical, and thus at jet impact, the bubble has larger volume. As the bubble collapses farther from the wall, the interactions between a bubble and wall are no longer strong, and thus bubble collapses more spherically and the jet impacts the opposite bubble wall at the smaller volume. Additionally, the bubble is less compressed at jet impact in the compressible cases, compared to the potential flow cases, because lower bubble–wall velocity is achieved in the compressible case.

The bubble displacement characterizes the dynamics of a bubble during the collapse and demonstrates the effects of a nearby wall on bubble motion during the collapse. For all simulations, the normalized bubble displacement at jet impact reduces as the initial stand-off distance increases. As illustrated in figure 4.1(b), the effect of a nearby wall can be roughly replaced by an image sink located at the wall side with the same distance to the wall. The image sink draws the bubble toward itself; its effects are inversely proportional to the distance between the bubble and the sink. Thus, as the bubble begins to collapse farther from the wall, the bubble translates a smaller distance. Furthermore, for small driving pressures, the bubble translates large distance in the compressible case due to large impact time. In the potential flow case, driving pressure has negligible effects on the bubble displacement. In addition, in the compressible case, the bubble translates smaller distance than the potential flow case because of smaller jet impact time.

The jet velocity characterizes the dynamics of a re-entrant jet and can be used to estimate the strength of a shock produced at jet impact. For all simulations, the normalized jet velocity at jet impact rises as the initial stand-off distance increases. At larger driving pressures, in the potential flow simulations, the bubble is more compressed, such that the higher jet velocities are achieved. However, in the compresssible simulations, the increase in the jet velocity is limited by liquid compressibility, such that the normalized jet velocity is smaller at larger driving pressures. In addition, the jet velocity in the compressible case is smaller than the incompressible case.

Thus, as the initial stand-off distance is decreased, the presence of the wall leads to larger minimum bubble volume, bubble migration, and lower jet velocities. In addition, for a given driving pressure ratio and initial stand-off distance, in the compressible case, the bubble volume is larger and the jet velocity is smaller, compared to the potential flow case. In addition, the jet impact occurs at a location farther from the wall. As a result, the peak pressure along the boundary produced by a water-hammer shock is expected to be lower than the peak pressure in the potential flow case.

4.4 Conclusions

In summary, we assess the effects of compressibility on the dynamics of the bubble and the re-entrant jet by comparing direction simulations with potential flow simulations. At the beginning of the collapse, both cases show similar bubble morphologies even though the pressure fields are significantly different; in the compressible case, the bubble is exposed to a higher pressure over a longer period of time compared to the potential flow case. As a result, the bubble compresses further and the collapse becomes more rapid.

We choose the jet thickness to compare bubble morphologies and collapsing time in the compressible and potential flow cases. We also calculate the time shift, which is the time difference between the instants where both cases yield the same jet thickness. This time shift is more pronounced in the early stages of collapse due to the difference in the surrounding pressure fields and decreases as the collapse progresses. For the most part of the collapse, similar overall bubble kinematics are observed for both cases after implementing a time shift. In the final stages of collapse, there are discrepancies in the dynamics of the bubble and jet between the compressible and potential flow cases.

We finally investigate the effects of compressibility on the bubble dynamics (i.e., time, bubble volume, bubble displacement, and jet velocity) at jet impact. For all cases, as the initial stand-off distance increases, the normalized time, bubble volume, and bubble displacement at jet impact reduce, while the normalized jet velocity rises because the bubble remains spherical for a longer time during its collapse. Furthermore, the driving pressure ratio changes the bubble dynamics significantly in the compressible cases. For a given driving pressure ratio and initial stand-off distance, in the compressible case, the bubble volume is larger and the jet velocity is smaller, compared to the potential flow case. In addition, the jet impact occurs at a location farther from the wall. As a result, the peak pressure along the boundary produced by a water-hammer shock is expected to be lower than the peak pressure in the potential flow case.

Even after jet impact, liquid compressibility is expected to affect the bubble collapse and shock wave emission. In the future, we plan to investigate the bubble collapses and rebounds after jet impact. This understanding will help better understand the importance of liquid compressibility to develop a model for impact loads produced by bubble collapse.

CHAPTER 5

Conclusions

This chapter summarized the research, discusses the results, and proposes directions for future studies.

5.1 Summary and conclusions

The main objective of this study was to better understand the dynamics and energy transport of individual oscillating bubbles and their relation to the macroscopic phenomena. Towards that purpose, this thesis primarily investigated the growth and collapse of a gas bubble in an infinite medium and near a rigid surface. Specifically, the present study aimed to (i) develop a theoretical framework to better describe energy transport in the liquid–bubble system, (ii) explore the role of compressibility in the overall bubble dynamics, energy transport, and shock emission, and (iii) develop a predictive model for energy transport, concentration and release during bubble growth and collapse. The following subsections summarize chapters 2 through 4 in the present study.

5.1.1 Spherical bubble dynamics

The study of spherical bubble dynamics is the first step toward understanding and predicting bubble dynamics in practically relevant geometries, in which case the bubble dynamics are typically non-spherical. In particular, it is critical to understand the energy concentration and shock emission in spherical bubble collapse in order to build a predictive model for damage induced by cavitation bubbles in applications.

In chapter 2, we considered the classical Rayleigh collapse problem of spherical bubble collapse driven by an instantaneous increase in liquid pressure. We proposed a theoretical approach to accurately represent energy transport, including direct calculations of energy losses due to liquid compressibility. This approach was used to build an energy framework for identifying energy modes in the liquid–bubble system and for understanding energy transport between these modes. The overall energy transport can be described as follows: as the bubble collapses, the potential energy in the liquid is primarily transferred to kinetic energy of the liquid, which is ultimately concentrated into the internal energy of the bubble; in the final stages of collapse, energy losses due to acoustic radiation become significant. In the early stages of the collapse, the liquid primarily loses its kinetic energy due to acoustic radiation, while in the final stages of the collapse, the bubble primarily loses its internal energy due to acoustic radiation.

Using our energy budget framework, we quantitatively showed that the energy concentration during the collapse follows one of two scenarios: up to the driving pressure ratio of 112, most of the initial potential energy is concentrated into the bubble at collapse, whereas beyond that pressure ratio a significant fraction of the initial energy is lost via acoustic radiation as the bubble-wall velocity becomes comparable to the speed of sound, thus reducing the efficiency of the energy concentration process. Overall, as the driving pressure ratio is increased, the liquid has a larger initial potential energy, such that a larger energy is concentrated into a smaller bubble confinement as internal energy although larger fraction of initial potential energy is lost through acoustic radiation. Hence, the bubble energy density increases and a stronger shock is released at collapse. Finally, we derived, for the first time, scaling relations for the bubble volume, energy concentration, bubble energy density, and shock emission at collapse accounting for liquid compressibility and depending on the parameters governing the problem, i.e., the driving pressure ratio and effective Mach number.

Our framework and scaling relations could be used in conjunction with single-phase simulations as a means to estimate the cavitation activity. For instance, the expected cavitation activity of a nucleus/bubble following a Lagrangian trajectory could be determined for the corresponding pressure. Further, the resulting shock produced by the collapsing bubble could be determined. Such information could help devise strategies to mitigate cavitation, for instance by modifying the geometry accordingly.

In chapter 3, we studied the dependence of the bubble response and energy transport on the properties of ultrasound waveform. We proposed a theoretical approach to accurately represent energy transport, considering the contributions of external forcing (e.g., ultrasound waves), thermal conduction, viscosity, and surface tension. This approach was used to build a framework to track the evolution of individual energy modes in the system. During the growth and collapse of the bubble exposed to an ultrasound wave, the energy is transferred as follows. Energy is input to the system via the ultrasound, which decreases the liquid pressure. As a result, the higher-pressure bubble expands rapidly with the surrounding liquid, which also moves outward and thus acquires kinetic energy. As the bubble expands, its pressure and velocity decrease, thereby causing liquid kinetic energy to decrease and potential energy to increase. At this point, the state of the system is the same as the initial condition of the problem described in chapter 2, in which case potential energy is converted to liquid kinetic energy, which confines the bubble, raising its pressure and thus its kinetic energy. In the final stages of the collapse, a significant fraction of the bubble internal energy is lost through acoustic radiation as bubble–wall velocities become comparable to the speed of sound. We showed that, for larger wave amplitudes, smaller frequencies, and smaller equilibrium radii, a greater amount of energy is introduced to the system via waves, such that the bubble reaches a larger maximum radius relative to the equilibrium radius; the different energy modes also increase at maximum radius, relative to the equilibrium total energy.

Assuming that most of the input energy is finally stored as liquid potential energy at maximum size, we found that the growth ratio of the bubble is determined by two dimensionless parameters; the acoustic pressure ratio and inertial-to-acoustic time ratio. We developed scaling relations for the maximum bubble radius, as well as the gas pressure and the dominant energy modes at that radius. The maximum bubble radius follows one of two scenarios; the bubble undergoes stable oscillation when the equilibrium radius is smaller than the Blake threshold radius, while inertial cavitation is observed when the equilibrium radius is smaller than the critical radius. Our scaling relations can be employed to predict the bubble radius, energy concentration, and shock emission at collapse. We also applied our framework and scaling relations to the nano-size bubble under the histotripsy waveform, which demonstrates wide applicability of our approach to diverse waveforms. The present results form the basis for better understanding of energy concentration and shock emission in non-spherical bubble collapse.

5.1.2 Non-spherical bubble dynamics

We showed in chapter 2 that spherical bubble collapse is fully characterized by two parameters, the driving pressure ratio and the effective Mach number. In practice, impact loads with the greatest potential for damage are produced by bubbles collapsing sufficiently close to the surface under consideration, in which case the collapse is no longer spherical as a re-entrant jet develops and penetrates the bubble. In chapter 4, we investigated the role of compressibility on the collapse of a gas bubble near a rigid surface. In particular, we examined the bubble dynamics using direct simulations and potential flow calculations. In addition to the driving pressure ratio and the effective Mach number, key collapse quantities are governed by a third parameter, the initial stand-off distance of the bubble from the wall.

By comparing direct simulations with potential flow calculations, we assessed the effects of compressibility on the dynamics of the bubble and the re-entrant jet. At the beginning of the collapse, both cases show similar bubble morphologies even though the pressure fields are significantly different: in the compressible case, the bubble is exposed to a higher pressure over a longer period of time compared to the incompressible case. As a result, the bubble compresses further and delays its collapse in the compressible case. We observed that, for a given jet thickness, which is the thickness of the bubble along the centerline, there exists a time difference between the compressible and incompressible; this difference is more pronounced in the early stages of collapse and reduces as the collapse progresses. For the most part of the collapse, similar overall bubble kinematics were observed for both cases after implementing a time shift. In the final stages of the collapse, there are observable discrepancies in bubble dynamics at jet impact between the compressible and incompressible results. We finally investigated the effects of compressibility on the bubble dynamics at jet impact. In the compressible case, the bubble volume is larger and the jet velocity is smaller compared to the incompressible case. In addition, the jet impact occurs at a location farther from the boundary. As a result, the peak pressure along the boundary produced by a water-hammer shock is expected to be lower than the peak pressure in the incompressible case.

5.2 Suggestions for future research directions

This study provided insight into further investigation of cavitation bubble dynamics, especially in terms of energy. The following subsections propose future studies that can be examined as a next step of the present study: (i) energy budget framework for cavitation bubbles and (ii) spherical and (iii) non-spherical bubble dynamics.

5.2.1 Energy budget framework for cavitation bubbles

We presented a framework that identifies energy modes in the liquid–bubble system and describes energy transport between these modes, based on models considering different levels of compressibility. Figure 5.1 outlines numerical methods and physical models for simulations of spherical and non-spherical bubble dynamics, considering different levels of compressibility. The compressible Navier–Stokes equation, which is a fundamental equation for compressible flows, can be approximated to the equations for compressible BIM and the Keller–Miksis equation with the assumption of weakly compressible flows. It can be further simplified to the equations for BIM and the Rayleigh–Plesset equation with the assumption of incompressible flows. In our study about energy transport in the system, we used models (i.e., the Keller–Miksis and Rayleigh–Plesset equation, and compressible and incompressible BIM) assuming weakly compressible and incompressible flows, which correspond to a flow velocity smaller than the speed of sound. Although our framework is limited when it comes to describing energy transport corresponding to bubbles driven by

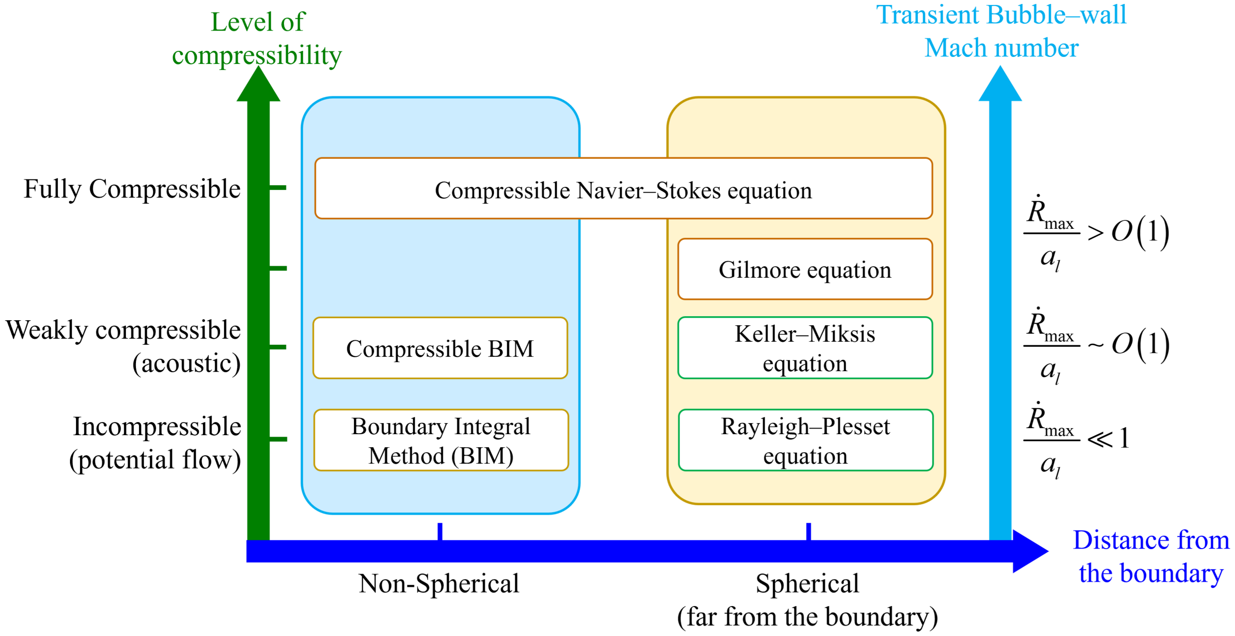

Figure 5.1: Numerical methods and physical models for simulations of spherical and non-spherical bubble dynamics, categorized by the level of compressibility and transient Mach number.

high-amplitude (shock) waves, it is relevant to describe the damage induced by bubbles in environments where the dynamics of shock waves are critical (e.g., underwater explosion, shock-induced bubble collapse). In past studies, Vogel *et al.* (1996) and Tomita *et al.* (2003) proposed an approach for evaluating the energy of the shock wave produced at collapse. However, their approach is derived from the acoustic limit and does not strictly satisfy the energy balance. We recommend that future research efforts consider developing an energy budget framework based on models for cases where the flow Mach number is larger than 1, such as the Gilmore equation and the compressible Navier–Stokes equation. Such future research would help quantify energy losses due to shock waves at collapse and the delivery of energy via shock waves to a nearby object and provide a better estimation of damage induced by cavitation bubbles.

In practical applications (e.g., lithotripsy and naval hydrodynamics), cavitation bubbles are often generated in the form of a cloud. Although our energy framework is only applied to individual bubbles in the present study, it could also be used to describe energy transport in bubble clouds (Ando *et al.*, 2011; Fuster & Colonius, 2011). Continuum bubbly flow models assume that bubbles are spherical. To close the model, the Rayleigh–Plesset–type equations are employed, such that the individual microscopic bubbles and macroscopic bubbly flows communicate through the energy transport process. Thus, the pressure in macroscopic flows becomes an input for introducing potential energy into each bubble, affecting the oscillations of the bubble, energy transport, and energy losses in the liquid–bubble system. Our energy budget framework could be used to describe the flow of energy, which starts with the energy input of macroscopic flows to energy release by microscopic bubbles.

Furthermore, nearby vapor structures of cavitation bubbles, which reduce the speed of sound in flows, may change the dynamics of bubbles. In high-speed flows, local pressure reduction near the surface of structures (e.g., hydrofoil, wedge) leads to the generation of large vapor structures broken up into small micro-size bubbles. Compared to single-phase liquid flows, high volume fractions in flows cause the speed of sound to be reduced (Bhatt *et al.*, 2021), such that effects of liquid compressibility may become significant due to larger Mach number in the flows. In the present work, we consider only an isolated bubble in an infinite sea of liquid. However, our framework can consider a transient change in the speed of sound due to motion of nearby vapor structures, which may enhance the energy losses due to acoustic radiation.

5.2.2 Spherical bubble dynamics

We proposed an approach identifying energy modes that cannot be neglected in the growth and collapse of a gas (single component) bubble. In the present study, we investigated the growth and collapse of a gas bubble by incorporating bubble dynamics equations with equations accounting for additional effects (e.g., thermal conduction, viscous dissipation, surface tension) (Nigmatulin *et al.*, 1981; Barajas & Johnsen, 2017; Hao *et al.*, 2017). However, in a variety of cavitation phenomena, such as hydrodynamic and laser-induced cavitation, the bubble consists of both gas and vapor, such that a more comprehensive framework is needed to accurately describe energy transport in the system of liquid and gas-vapor bubble. For example, a phase transition is one of the key characteristics of vapor bubbles, such that the phenomenon should be considered pertaining to energy conservation in the system. In addition, multiple phenomena, including gas diffusion, heat conduction, and phase transition, occur at the bubble wall, so the boundary conditions at the bubble wall would need careful treatment.

We investigated dynamics of a bubble in water, which may show different behaviors in soft materials. Although our work focused on liquid with low viscosity and zero elasticity, we can extrapolate possible results when the bubble collapses in soft medium, summarized below. Due to higher viscoelasticity in soft materials, the bubble would be less compressed, compared to the bubble in water. In addition, a smaller fraction of the total energy would be concentrated into the bubble due to the energy losses due to viscosity and elastic energy. Thus, a shock with a smaller peak pressure would be produced at collapse. To better understand the dependence of shock pressures on the properties of soft materials, a model for describing energy transport in a system of a bubble and a soft material is required.

5.2.3 Non-spherical bubble dynamics

In our non-spherical bubble dynamics study, we observed that during collapse, a re-entrant jet is formed toward the boundary, piercing the bubble, which produces a water-hammer shock wave. However, the complex geometries or nearby surfaces often cause the bubble to collapse differently, and thus our study has limitations on describing impact loads due to bubble collapse near practical geometries. Han *et al.* (2015) and Supponen *et al.* (2016) showed that nearby interfaces (e.g., bubble, free surface) change the dynamics of a bubble and a jet, which then cause the jet to be formed in different directions. These studies demonstrated that nearby surfaces or interfaces can enhance or suppress the formation of a re-entrant jet, and they can even cause the formation of multiple jets, such that impact loads produced by bubbles are significantly affected by the neighboring geometries. In our simulations, different boundary conditions could be considered to investigate the effects of complex geometries (e.g., corner, channel, cube) on the bubble dynamics. Future work considering even more complex geometries (e.g., textured surface) could improve our understanding of the impact loads due to bubble collapse in practical applications.

Appendices

Appendix A

Scaling Relations Using the Modified Herring Equation

The Modified Herring equation, which is a simplified version of the general Keller–Herring equation Prosperetti & Lezzi (1986) with $\lambda = 1$, is given by

$$R\ddot{R} + \frac{3}{2}\dot{R}^2 = \frac{p_{eq}}{\rho_l}\left(\frac{R_o}{R}\right)^{3k}\left(1 - 3k\frac{\dot{R}}{a_l}\right) - \frac{p_\infty}{\rho_l}. \tag{A.1}$$

When the interface velocity is maximum with zero acceleration (i.e., $R = R_I$), Eq. (A.1) reduces to

$$\frac{3}{2}\dot{R}_I^2 \approx \frac{p_{eq}}{\rho_l}\left(\frac{R_o}{R}\right)^{3k}\left(-3k\frac{\dot{R}}{a_l}\right). \tag{A.2}$$

For most of the collapse, the interface velocity tends to the limit Brennen (1995); Lauterborn & Kurz (2010): $\dot{R} \to (2p_\infty/3\rho_l)^{1/2}(R_o/R)^{3/2}$. Combining this relation with Eq. (A.2) yields

$$\frac{V_I}{V_o} \approx \left(\frac{p_\infty}{p_{eq}}\right)^{-2/(2k-1)} M^{2/(2k-1)}\left(6k^2\right)^{1/(2k-1)}. \tag{A.3}$$

After manipulating the RP equation, a relation between V_I and V_{col} can be obtained: $V_{col}/V_o = (V_I/V_o)k^{1/(k-1)}$. Thus, the bubble volume at collapse at high p_∞/p_{eq} is given by

$$\frac{V_{col}}{V_o} \approx \eta_V\left(\frac{p_\infty}{p_{eq}}\right)^{-2/(2k-1)} M^{2/(2k-1)}, \tag{A.4}$$

where $\eta_V = k^{-1/(k-1)}(6k^2)^{1/(2k-1)}$.

Appendix B

Verification of Cold Liquid Assumption for Thermal Energy Equation of Liquid

The thermal energy equation of liquid can be modified as the temperature equation:

$$\frac{\partial T_l}{\partial t} + u_l \frac{\partial T_l}{\partial r_{out}} = \frac{\alpha_l}{r_{out}^2} \frac{\partial}{\partial r_{out}} \left(r_{out}^2 \frac{\partial T_l}{\partial r_{out}} \right) + \frac{12\mu_l}{\rho_l c_{p,l}} \left(\frac{R^4 \dot{R}^2}{r_{out}^6} \right), \tag{B.1}$$

where T_l is the liquid temperature, r_{out} is the radial coordinate in liquid, u_l is the liquid velocity, $\alpha_l = K_l/\rho_l c_{p,l}$ is the thermal diffusivity of liquid, K_l is the thermal conductivity in liquid, ρ_l is the liquid density, $c_{p,l}$ is the liquid heat capacity at constant pressure, and μ_l is the liquid viscosity. Since changes in liquid temperature mostly occur near the bubble interface due to large liquid heat capacity, the acoustic component of liquid velocity is neglected, and $u_l = R^2\dot{R}/r_{out}^2$ (Barajas & Johnsen, 2017; Hao *et al.*, 2017). The liquid domain is discretized with the following transformation, $x = 2/[1 + (y-1)/L] - 1$ and $y = r_{out}/R$, to consider infinitely large and spherically symmetric domain.

The balance of thermal energy at the bubble wall can be written as Barajas & Johnsen (2017); Hao *et al.* (2017)

$$\left. \frac{\partial \theta_b}{\partial r_{in}} \right|_w = K_l \left. \frac{\partial T_l}{\partial r_{out}} \right|_w, \tag{B.2}$$

where the gas diffusion and phase change are neglected. This equation implies at the bubble wall, the heat flux from the bubble side should be equal to the heat flux into the liquid side.

Using the dimensional variables R_{eq}, U, and T_∞, the temperature equation for liquid (B.1) is nondimensionalized as follows:

$$\frac{\partial T_l^*}{\partial t^*} = \frac{(1+x)^2}{LR^*}\left[\frac{\mathrm{Fo}_l}{R^*}\left(\frac{1+x}{2L}-\frac{1}{y}\right)+\frac{\dot{R}^*}{2}\left(\frac{1-y^3}{y^2}\right)\right]\frac{\partial T_l^*}{\partial x}+\frac{\mathrm{Fo}_l}{4}\frac{(1+x)^4}{L^2R^{*2}}\frac{\partial^2 T_l^*}{\partial x^2}+12\frac{\mathrm{Ec}_l}{\mathrm{Re}_l}\frac{\dot{R}^{*2}}{R^2y^6}, \tag{B.3}$$

where Fo_l is the liquid Fourier number and $\mathrm{Fo}_l = \alpha_l(R_o/U)/R_o^2$, α_l is the liquid thermal diffusivity, Re_l is the liquid Reynolds number and $\mathrm{Re}_l = \rho_l U R_o/\mu_l$, and Ec_l is the liquid Eckert number and $\mathrm{Ec}_l = U^2/c_{p,l}T_\infty$. Eq. (B.2) also becomes

$$K_{eq}\left.\frac{\partial \theta_b^*}{\partial y}\right|_w = -\frac{2K_l}{L}\left.\frac{\partial T_l^*}{\partial x}\right|_w. \tag{B.4}$$

For verification of cold liquid assumption, we choose the combination of the gaussian pulse and the equilibrium bubble radius (p_A =1 MPa, $\sigma = 1$ μs, R_{eq} =1 μm), in which the bubble oscillations is most explosive. For $N_{in} = 1000$ and $N_{out} = 1000$, R_{max}/R_{eq} =127.904 and R_{col}/R_{eq} =0.04361 for the cold liquid case, and R_{max}/R_{eq} =127.903 and and R_{col}/R_{eq} =0.04369 for the liquid with thermal conduction. Differences are below 0.001 %. Thus, the cold liquid assumption is reasonable for the parameter space in this study.

BIBLIOGRAPHY

Aganin, A. A., & Mustafin, I. N. 2021. Outgoing shock waves at collapse of a cavitation bubble in water. *Int. J. Multiph. Flow*, **144**, 103792.

Ando, K., Colonius, T., & Brennen, C. E. 2011. Numerical simulation of shock propagation in a polydisperse bubbly liquid. *International Journal of Multiphase Flow*, **37**(6), 596–608.

Apfel, R. E. 1981. Acoustic cavitation prediction. *J. Acoust. Soc. Am.*, **69**(6), 1624.

Apfel, R. E. 1982. Acoustic cavitation: a possible consequence of biomedical uses of ultrasound. *Br. J. Cancer*, **45**, 140–146.

Arndt, Roger E.A. 1981. Cavitation in fluid machinery and hydraulic structures. *Ann. Rev. Fluid Mech.*, **13**, 273–328.

Arons, A. B. 1954. Underwater explosion shock wave parameters at large distances from the charge. *J. Acoust. Soc. Am*, **26**(3), 343–346.

Arons, A. B., & Yennie, D. R. 1948. Energy partition in underwater explosion phenomena. *Rev. Mod. Phys.*, **20**(3), 519–536.

Bader, K. B., & Holland, C. K. 2016. Predicting the growth of nanoscale nuclei by histotripsy pulses Predicting the growth of nanoscale nuclei by histotripsy pulses. *Phys. Med. Biol.*, **61**, 2947–2966.

Bader, K. B., Vlaisavljevich, E., & Maxwell, A. D. 2019. For whom the bubble grows: physical principles of bubble nucleation and dynamics in histotripsy ultrasound therapy. *Ultrasound Med. Biol.*, **45**(5), 1056–1080.

Barajas, C., & Johnsen, E. 2017. The effects of heat and mass diffusion on freely oscillating bubbles in a viscoelastic, tissue-like medium. *J. Acoust. Soc. Am.*, **141**(2), 908–918.

Bark, G., & Bensow, R. E. 2014. Hydrodynamic processes controlling cavitation erosion. *In: Advanced Experimental and Numerical Techniques for Cavitation Erosion Prediction*. Springer.

Beig, S. A. 2018. *A computational study of the inertial collapse of gas bubbles near a rigid surface*. Ph.D. thesis, University of Michigan.

Beig, S. A., & Johnsen, E. 2015. Maintaining interface equilibrium conditions in compressible multiphase flows using interface capturing. *J. Comput. Phys.*, **302**, 548–566.

Beig, S. A., Aboulhasanzadeh, B., & Johnsen, E. 2018. Temperatures produced by inertially collapsing bubbles near rigid surfaces. *J. Fluid Mech.*, **852**, 105–125.

Besant, W. H. 1948. *Hydrostatics and hydrodynamics*. London: Cambridge University Press.

Best, J. P. 1993. The formation of toroidal bubbles upon the collapse of transient cavities. *J. Fluid Mech.*, **251**, 79–107.

Bhatt, A., Ganesh, H., & Ceccio, S. L. 2021. Cavitating flow behind a backward facing step. *Int. J. Multiph. Flow*, **139**, 103584.

Blake, F. G. 1949. The tensile strength of liquids; a review of the literature. *Harvard Acou. Res. Lab. Rep.*, **170**, TM9.

Blake, J. R., Doherty, G., & Taib, B. B. 1986. Transient cavities near boundaries. Part 1. Rigid boundary. *J. Fluid Mech.*, **170**, 479–497.

Blake, J.R., & Gibson, D.C. 1987. Cavitation bubbles near boundaries. *Ann. Rev. Fluid Mech.*, **19**, 99–123.

Brennen, C. E. 1995. *Cavitation and bubble dynamics*. Oxford University Press.

Brinton, T. J., Ali, Z. A., Hill, J. M., Meredith, I. T., Maehara, A., Illindala, U., Lansky, A., Götberg, M., van Mieghem, N. M., Whitbourn, R., Fajadet, J., & Di Mario, C. 2019. Feasibility of shockwave coronary intravascular lithotripsy for the treatment of calcified coronary stenoses first description. *Circulation*, **139**(6), 834–836.

Brujan, E. A. 2004. The role of cavitation microjets in the therapeutic applications of ultrasound. *Ultrasound Med. Biol.*, **30**(3), 381–387.

Brujan, E. A., Keen, G. S., Vogel, A., & Blake, J. R. 2002. The final stage of the collapse of a cavitation bubble close to a rigid boundary. *Phys. Fluids*, **14**(1), 85–92.

Burke, W. L. 1970. Runaway solutions: Remarks on the asymptotic theory of radiation damping. *Phys. Rev. A*, **2**(4), 1501–1505.

Cammalleri, A., Croce, P., Lee, W., Yoon, K., & Yoo, S. S. 2020. Therapeutic Potentials of Localized Blood-Brain Barrier Disruption by Noninvasive Transcranial Focused Ultrasound: A Technical Review. *J. Clin. Neurophysiol.*, **37**(2), 104–117.

Ceccio, S. L., & Brennen, C. E. 1991. Observations of the dynamics and acoustics of travelling bubble cavitation. *J. Fluid Mech.*, **233**(633), 633–660.

Chahine, G. L., Franc, J. P., & Karimi, A. 2014. Mass loss and advanced periods of erosion. *In: Advanced Experimental and Numerical Techniques for Cavitation Erosion Prediction*. Springer.

Cole, R. H. 1948. *Underwater explosions*. Princeton University Press.

Dular, M., Coutier, O., & Petkovšek, M. 2013. Observations of cavitation erosion pit formation. *Ultrason. Sonochem.*, **20**, 1113–1120.

Estrada, J. B., Barajas, C., Henann, D. L., Johnsen, E., & Franck, C. 2018. High strain-rate soft material characterization via inertial cavitation. *J. Mech. Phys. Solids*, **112**, 291–317.

Flynn, H. G. 1975a. Cavitation dynamics. I. A mathematical formulation. *J. Acoust. Soc. Am.*, **57**(6), 1379–1396.

Flynn, H. G. 1975b. Cavitation dynamics. II. Free pulsations and models for bubbles. *J. Acoust. Soc. Am.*, **58**(6), 1160–1170.

Fortes-Patella, R., Challier, G., Reboud, J. L., & Archer, A. 2013. Energy balance in cavitation erosion: From bubble collapse to indentation of material surface. *J. Fluids Eng.*, **135**(1), 1–11.

Franc, J.-P., & Michel, J.-M. 2006. *Fundamentals of cavitation*. Vol. 76. Springer science Business media.

Fuster, D., & Colonius, T. 2011. Modelling bubble clusters in compressible liquids. *J. Fluid Mech.*, **688**, 352–389.

Gaudron, R., Warnez, M. T., & Johnsen, E. 2015. Bubble dynamics in a viscoelastic medium with nonlinear elasticity. *J. Fluid Mech.*, **766**, 54–75.

Geers, T. L., & Hunter, K. S. 2002. An integrated wave-effects model for an underwater explosion bubble. *J. Acoust. Soc. Am.*, **111**(4), 1584–1601.

Ghahramani, E., Ström, H., & Bensow, R. E. 2021. Numerical simulation and analysis of multiscale cavitating flows. *J. Fluid Mech.*, **922**, 1–54.

Gilmore, F. R. 1952. *The growth or collapse of a spherical bubble in a viscous compressible liquid*. Tech. rept. 26–4.

Gottlieb, S., & Shu, C.-W. 1996. Total variation diminishing Runge-Kutta schemes. *Math. Comput.*, **67**, 73–85.

Guennoun, M. F. 2006. *Étude physique de l'apparition et du development de la cavitation sur une aube isolee*. Ph.D. thesis, EPFL.

Han, B., Köhler, K., Jungnickel, K., Mettin, R., Lauterborn, W., & Vogel, A. 2015. Dynamics of laser-induced bubble pairs. *J. Fluid Mech.*, **771**, 706–742.

Hao, Y., Zhang, Y., & Prosperetti, A. 2017. Mechanics of gas-vapor bubbles. *Phys. Rev. Fluids*, **2**(3), 1–16.

Harten, A., Lax, P. D., & van Leer, B. 1983. On Upstream Differencing and Godunov-Type Schemes for Hyperbolic Conservation Laws. *SIAM Review*, **25**(1), 35–61.

Henry de Frahan, M. T., Varadan, S., & Johnsen, E. 2015. A new limiting procedure for discontinuous Galerkin methods applied to compressible multiphase flows with shocks and interfaces. *J. Comput. Phys.*, **280**, 489–509.

Herring, C. 1941. *Theory of the pulsations of the gas bubble produced by an underwater explosion*. Tech. rept. 236. Columbia Univ. Office Sci. Res. Dev.

Hickling, R. 1994. Transient, high-pressure solidification associated with cavitation in water. *Phys. Rev. Lett.*, **73**, 2853.

Hickling, R., & S., Plesset M. 1964. Collapse and rebound of a spherical bubble in water. *Phys. Fluids*, **7**, 7–14.

Holzfuss, J. 2010. Acoustic energy radiated by nonlinear spherical oscillations of strongly driven bubbles. *Proc. R. Soc. A*, **466**, 1829–1847.

Hunt, J. D., & Jackson, K. A. 1966. Nucleation of the ice phase in supercooled water. *J. Appl. Phys.*, **37**, 254.

Hunter, Kendall S., & Geers, Thomas L. 2004. Pressure and velocity fields produced by an underwater explosion. *J. Acoust. Soc. Am.*, **115**(4), 1483–1496.

Ignee, A., Atkinson, N. S. S., Schuessler, G., & Dietrich, C. F. 2016. Ultrasound contrast agents. *Endoscopic Ultrasound*, **5**(6), 355–362.

Isselin, Jean Christophe, Alloncle, Anne Patricia, & Autric, Michel. 1998. On laser induced single bubble near a solid boundary: Contribution to the understanding of erosion phenomena. *J. Appl. Phys.*, **84**(10), 5766–5771.

Jiang, G.-S., & Shu, C.-W. 1996. Efficient Implementation of Weighted ENO Schemes. **228**(126), 202–228.

Johnsen, E., & Colonius, T. 2009. Numerical simulations of non-spherical bubble collapse. *J. Fluid Mech.*, **629**, 231–262.

Karimi Galougahi, Keyvan, Patel, Sanjay, Shlofmitz, Richard A., Maehara, Akiko, Kereiakes, Dean J., Hill, Jonathan M., Stone, Gregg W., & Ali, Ziad A. 2020. Calcific Plaque Modification by Acoustic Shockwaves: Intravascular Lithotripsy in Coronary Interventions. *Circ. Cardiovasc. Interv.*

Keller, J. B., & Kolodner, I. I. 1956. Damping of underwater explosion bubble oscillations. *J. Appl. Phys.*, **27**, 1152–1161.

Keller, J. B., & Miksis, M. 1980. Bubble oscillations of large amplitude. *J. Acoust. Soc. Am.*, **68**, 628–633.

Khokhlova, Vera A., Fowlkes, J. Brian, Roberts, William W., Schade, George R., Xu, Zhen, Khokhlova, Tatiana D., Hall, Timothy L., Maxwell, Adam D., Wang, Yak Nam, & Cain, Charles A. 2015. Histotripsy methods in mechanical disintegration of tissue: Towards clinical applications. *Int. J. Hyperther.*, **31**(2), 145–162.

Kim, K-H., Franc, J-P., & Karimi, A. 2014. *Advanced Experimental and Numerical Techniques for Cavitation Erosion Prediction, Series Fluid Mechanics and Its Applications*. Vol. 106. Springer.

Kim, M., Beig, S.B., & Johnsen, E. Energy concentration and release during the inertial collapse of a spherical gas cavity in a liquid. *In preparation for Phys. Rev. Fluids*.

Kim, T.-H., & Kim, H.-Y. 2014. Disruptive bubble behaviour leading to microstructure damage in an ultrasonic field. *J. Fluid Mech.*, **750**, 355–371.

Kirkwood, J. G., & Bethe, H. A. 1942. *The pressure wave produced by an underwater explosion*. Tech. rept. 588. Office Sci. Res. Dev.

Knapp, R. T., Dailey, J. W., & Hammitt, F. G. 1970. *Cavitation*. McGraw-Hill Book Company.

Lamb, H. 1932. *Hydrodynamics*. Cambridge University Press.

Lauterborn, Werner, & Kurz, Thomas. 2010. Physics of bubble oscillations. *Rep. Prog. Phys.*, **73**(106501).

Leighton, T. 2012. *The acoustic bubble*. Academic Press.

Lind, S. J. 2014. On the dynamics of non-spherical magnetic microbubbles. *Phys. Fluids*, **26**, 061901.

Lindau, O., & Lauterborn, W. 2003. 'Cinematographic observation of the collapse and rebound of a laser-produced cavitation bubble near a wall. *J. Fluid Mech.*

Longuet-Higgins, M. S., & Cokelet, E. D. 1976. The deformation of steep surface waves on water. *Proc. R. Soc. Lond.*, **350**, 1–26.

Mancia, L., Rodriguez, M., Sukovich, J., Xu, Z., & Johnsen, E. 2020. Single–bubble dynamics in histotripsy and high–amplitude ultrasound: Modeling and validation. *Phys. Med. Biol.*

Mancia, L., Rodriguez, M., Sukovich, J. R., Haskel, S., Xu, Z., & Johnsen, E. 2021. Acoustic Measurements of Nucleus Size Distribution at the Cavitation Threshold. *Ultrasound Med. Biol.*, **47**(4), 1024–1031.

Maxwell, A. D., Cain, C. A., Duryea, A. P., Yuan, L., Gurm, H. S., & Xu, Z. 2009. Noninvasive thrombolysis using pulsed ultrasound cavitation therapy – histotripsy. *Ultrasound Med. Biol.*, **35**(12), 1982–1994.

McDannold, N., Vykhodtseva, N., & Hynynen, K. 2006. Targeted disruption of the blood-brain barrier with focused ultrasound: Association with cavitation activity. *Phys. Med. Biol.*, **51**(4), 793–807.

Métayer, O. L., & Saurel, R. 2017. The Noble-Abel Stiffened-Gas equation of state The Noble-Abel Stiffened-Gas equation of state. **046102**(2016).

Movahed, P., & Johnsen, E. 2013. A solution-adaptive method for efficient compressible multifluid simulations, with application to the Richtmyer-Meshkov instability. *J. Comput. Phys.*, **239**, 166–186.

Murrone, A., & Guillard, H. 2005. A five equation reduced model for compressible two phase flow problems. *J. Comput. Phys.*, **202**(2), 664–698.

Naudé, C. F., & Ellis, A. T. 1961. On the mechanism of cavitation damage by nonhemispherical cavities collapsing in contact with a solid boundary. *J. Fluids Eng., Trans. ASME*, **83**(4), 648–656.

Nazari-Mahroo, H., Pasandideh, K., Navid, H. A., & Sadighi-Bonabi, R. 2018. How important is the liquid bulk viscosity effect on the dynamics of a single cavitation bubble? *Ultrason. Sonochem.*, **49**, 47–52.

Nigmatulin, R. I., Khabeev, N. S., & Nagiev, F. B. 1981. Dynamics, heat and mass transfer of vapour-gas bubbles in a liquid. *Int. J. Heat Mass Transf.*, **24**(6), 1033–1044.

Noltingk, B. E., & Neppiras, E. A. 1950. Cavitation produced by ultrasonics. *Proc. Phys. Soc. B*, **63**, 674–685.

Obreschkow, D., Kobel, P., Dorsaz, N., De Bosset, A., Nicollier, C., & Farhat, M. 2006. Cavitation bubble dynamics inside liquid drops in microgravity. *Phys. Rev. Lett.*, **97**, 094502.

Obreschkow, D., Tinguely, M., Dorsaz, N., Kobel, P., De Bosset, A., & Farhat, M. 2011. Universal scaling law for jets of collapsing bubbles. *Phys. Rev. Lett.*, **107**(204501), 1–5.

Obreschkow, D., Tinguely, M., Dorsaz, N., Kobel, P., De Bosset, A., & Farhat, M. 2013. The quest for the most spherical bubble: Experimental setup and data overview. *Exp. Fluids*, **54**(1503), 1–18.

Ohl, C. D., & Ikink, R. 2003. Shock-Wave-Induced Jetting of Micron-Size Bubbles. *Phys. Rev. Lett.*, **90**(21), 4.

Parsons, J. E., Cain, C. A., Abrams, G. D., & Fowlkes, J. B. 2006. Pulsed cavitational ultrasound therapy for controlled tissue homogenization. *Ultrasound Med. Biol.*, **32**(1), 115–129.

Patterson, B., Miller, D. L., & Johnsen, E. 2012. Theoretical microbubble dynamics in a viscoelastic medium at capillary breaching thresholds. *J. Acoust. Soc. Am.*, **132**(6), 3770–3777.

Pearson, A., Blake, J. R., & Otto, S. R. 2004. Jets in bubbles. *J. Eng. Math.*, **48**, 391–412.

Pecha, R., & Gompf, B. 2000. Microimplosions: Cavitation collapse and shock wave emission on a nanosecond time scale. *Phys. Rev. Lett.*, **84**(6), 1328–1330.

Philipp, A, & Lauterborn, W. 1998. Cavitation erosion by single laser- produced bubbles. *J. Fluid Mech.*, **361**, 75–116.

Pishchalnikov, Y. A., Sapozhnikov, O. A., Bailey, M. R., Williams, J. C., Cleveland, R. O., Colonius, T., Crum, L. A., Evan, A. P., & Ateer, J. 2003. Cavitation Bubble Cluster Activity in the Breakage of Kidney Stones by Lithotripter Shockwaves. **17**(7).

Plesset, M. S. 1949. The dynamics of cavitation bubbles. *ASME J. Appl. Mech.*, **16**, 228–231.

Plesset, M. S., & Chapman, Richard B. 1971. Collapse of an initially spherical vapour cavity in the neighbourhood of a solid boundary. *J . Fluid Mech.*, **47**(2), 283–290.

Plesset, M. S., & Prosperetti, A. 1977. Bubble dynamics and cavitation. *Ann. Rev. Fluid Mech.*, **9**, 145–185.

Pouliopoulos, A. N., Jimenez, Daniella A., Frank, Alexander, Robertson, Alexander, Zhang, Lin, Kline-Schoder, Alina R., Bhaskar, Vividha, Harpale, Mitra, Caso, Elizabeth, Papapanou, Nicholas, Anderson, Rachel, Li, Rachel, & Konofagou, Elisa E. 2020. Temporal stability of lipid-shelled microbubbles during acoustically-mediated blood-brain barrier opening. *Front. Phys.*, **8**, 1–16.

Prosperetti, A. 1977. Thermal effects and damping mechanisms in the forced radial oscillations of gas bubbles in liquids. *J. Acoust. Soc. Am.*, **61**(1), 17–27.

Prosperetti, A. 1979. Boundary conditions at a liquid–vapour interface. *Meccanica*, **46**, 34–46.

Prosperetti, A. 1987. The equation of bubble dynamics in a compressible liquid. *Phys. Fluids*, **30**(11), 3626–3628.

Prosperetti, A. 1991. The thermal behaviour of oscillating gas bubbles. *J. Fluid Mech.*, **222**, 587–616.

Prosperetti, A., & Lezzi, A. 1986. Bubble dynamics in a compressible liquid. part 1. first-order theory. *J. Fluid Mech.*, **168**, 457–478.

Prosperetti, A., Crum, L. A., & Commander, K. W. 1988. Nonlinear bubble dynamics. *J. Acoust. Soc. Am.*, **83**(2), 502–514.

Prosperetti, Andrea. 2017. Vapor Bubbles. *Ann. Rev. Fluid Mech.*, **49**, 221–248.

Ramsey, M. C., & P., Robert W. 2013. Energetic Cavitation Collapse Generates 3.2 Mbar Plasma with a 1.4 J Driver. *Phys. Rev. Lett.*, **110**, 154301.

Rayleigh, L. 1917. On the pressure developed in a liquid during the collapse of a spherical cavity. *Philos. Mag.*, **4**, 94–98.

Riemer, B. W., McClintock, D. A., Kaminskas, S., & Abdou, A. A. 2014. Correlation between simulations and cavitation-induced erosion damage in Spallation Neutron Source target modules after operation. *J. Nucl. Mater*, **450**(1-3), 183–191.

Saurel, R., & Pantano, C. 2018. Diffuse-Interface Capturing Methods for Compressible Two-Phase Flows. *Ann. Rev. Fluid Mech.*, **50**, 105–130.

Shaw, S. J., & Spelt, P. D.M. 2010. Shock emission from collapsing gas bubbles. *J. Fluid Mech.*, **646**, 363–373.

Shen, Y., Yasui, K., Zhu, T., & Ashokkumar, M. 2017. A model for the effect of bulk liquid viscosity on cavitation bubble dynamics. *Phys. Chem. Chem. Phys.*, **19**, 20635–20640.

Sirsi, S., & Borden, M. 2009. Microbubble Compositions, Properties and Biomedical Applications. *Bubble Sci. Eng. Technol.*, **1**(1–2), 3–17.

Stroud, A. H. 1966. *Gaussian quadrature formulas*. Prentice-Hall series.

Supponen, O., Obreschkow, D., Tinguely, M., Kobel, P., Dorsaz, N., & Farhat, M. 2016. Scaling laws for jets of single cavitation bubbles. *J. Fluid Mech.*, **802**, 263–293.

Supponen, O., Obreschkow, D., Kobel, P., Tinguely, M., Dorsaz, N., & Farhat, M. 2017. Shock waves from nonspherical cavitation bubbles. *Phys. Rev. Fluids*, **2**(9), 093601.

Templin, J. D. 1999. Radiation reaction and runaway solutions in acoustics. *Am. J. Phys.*, **67**(5), 407–413.

Tinguely, M. 2013. *The effect of pressure gradient on the collapse of cavitation bubbles in normal and reduced gravity*. Ph.D. thesis, EPFL.

Tinguely, M., Obreschkow, D., Kobel, P., Dorsaz, N., De Bosset, A., & Farhat, M. 2012. Energy partition at the collapse of spherical cavitation bubbles. *Phys. Rev. E*, **86**, 046315.

Tiwari, A., Pantano, C., & Freund, J. B. 2015. Growth-and-collapse dynamics of small bubble clusters near a wall. *J. Fluid Mech.*, **775**, 1–23.

Todd, N., Angolano, C., Ferran, C., Devor, A., Borsook, D., & McDannold, N. 2020. Secondary effects on brain physiology caused by focused ultrasound-mediated disruption of the blood–brain barrier. *J. Control. Release*, **324**, 450–459.

Tomita, Y., & Shima, A. 1986. Mechanisms of impulsive pressure generation and damage pit formation by bubble collapse. *J. Fluid Mech.*, **169**, 535–564.

Tomita, Y., Tsubota, M., & An-Naka, N. 2003. Energy evaluation of cavitation bubble generation and shock wave emission by laser focusing in liquid nitrogen. *J. Appl. Phys.*, **93**(5), 3039–3048.

Trilling, L. 1952. The Collapse and Rebound of a Gas Bubble. *J. Appl. Phys.*, **23**(1), 14–17.

Trummler, T., Bryngelson, S. H., Schmidmayer, K., Schmidt, S. J., Colonius, T., & Adams, N. A. 2020. Near-surface dynamics of a gas bubble collapsing above a crevice. *J. Fluid Mech.*, **899, A16**, 1–22.

Tung, Y. S., Vlachos, F., Choi, J. J., Deffieux, T., Selert, K., & Konofagou, E. E. 2010. In vivo transcranial cavitation threshold detection during ultrasound-induced blood-brain barrier opening in mice. *Phys. Med. Biol.*, **55**(20), 6141–6155.

Versluis, M., Stride, E., Lajoinie, G., Dollet, B., & Segers, T. 2020. Ultrasound Contrast Agent Modeling: A Review. *Ultrasound Med. Biol.*, **46**(9), 2117–2144.

Vogel, A., Lauterborn, W., & Timm, R. 1989. Optical and acoustic investigations of the dynamics of laser-produced cavitation bubbles near a solid boundary. *J. Fluid Mech.*, **206**, 299–338.

Vogel, A., Busch, S., & Parlitz, U. 1996. Shock wave emission and cavitation bubble generation by picosecond and nanosecond optical breakdown in water. *J. Acoust. Soc. Am.*, **100**(1), 148–165.

Vokurka, K. 1986. Comparison of Rayleigh's, Herring's, and Gilmore's models of gas bubbles. *Acta Acust. united Acust.*, **59**, 214–219.

Wang, Q. 2016. Local energy of a bubble system and its loss due to acoustic radiation. *J. Fluid Mech.*, **797**, 201–230.

Weinberg, K., & Ortiz, M. 2009. Kidney damage in extracorporeal shock wave lithotripsy: A numerical approach for different shock profiles. *Biomech. Model. Mechanobiol.*, **8**(4), 285–299.

Winder, D., McClintock, D., & Bruce, D. 2020. Cavitation-induced erosion in liquid metal spallation targets – A comparison between a predictive method and measured erosion damage to stainless steel target modules at the Spallation Neutron Source. *Wear*, **450–451**, 203257.

Wood, A.B. 1930. *A textbook of sound*. New York: Macmillan.

Xu, Z., Ludomirsky, A., Eun, L. Y., Hall, T. L., Tran, B. C., Fowlkes, J. B., & Cain, C. A. 2004. Controlled ultrasound tissue erosion. *IEEE Trans. Ultrason. Ferroelectr. Freq. Control*, **51**(6), 726–736.

Yang, X., & Church, C. C. 2005. A model for the dynamics of gas bubbles in soft tissue. *J. Acoust. Soc. Am.*, **118**(6), 3595–3606.

Yasui, K., Towata, A., Tuziuti, T., Kozuka, T., & Kato, K. 2011. Effect of static pressure on acoustic energy radiated by cavitation bubbles in viscous liquids under ultrasound. *J. Acoust. Soc. Am.*, **130**(5), 3233–3242.

Zel'dovich, Y.B., Raizer Y.P. 2002. *Physics of shock waves and high-temperature hydrodynamic phenomena*. Courier Corporation.

Zhong, P. 2013. *Shock wave lithotripsy*. Springer. Pages 291–338.

Zhong, P., Chuonq, C. J., & Preminger, G. M. 1993. Propagation of shock waves in elastic solids caused by cavitation microjet impact. II: Application in extracorporeal shock wave lithotripsy. *J. Acoust. Soc. Am.*, **94**(1), 29–36.

Zhou, G., & Prosperetti, A. 2020. Modelling the thermal behaviour of gas bubbles. *J. Fluid Mech.*, **901**, 1–15.